SLAC-R-841

Measurement of the Branching Fraction for the Decay B^{\pm} to K^{*\pm} gamma, K^{*\pm} to K^{\pm} \pi^{0} with the BaBar Detector

Karsten Koeneke

SLAC-R-841

Prepared for the Department of Energy
under contract number DE-AC02-76SF00515

Measurement of the branching fraction for the decay $B^{\pm} \to K^{*\pm}\gamma,\ K^{*\pm} \to K^{\pm}\pi^{0}$ with the BaBar detector [1]

Karsten Köneke

Stanford Linear Accelerator Center
2575 Sand Hill Road
Menlo Park, CA 94025

SLAC-R-841
September 2003

Prepared for the Department of Energy
under contract number DE-AC02-76SF0015

[1] M. S. thesis, University of Massachusetts Amherst

MEASUREMENT OF THE BRANCHING FRACTION FOR THE DECAY $B^{\pm} \to K^{*\pm}\gamma$, $K^{*\pm} \to K^{\pm}\pi^{0}$ WITH THE BABAR DETECTOR

A Thesis Presented

by

KARSTEN KÖNEKE

Submitted to the Graduate School of the
University of Massachusetts Amherst in partial fulfillment
of the requirements for the degree of

MASTER OF SCIENCE

September 2003

Physics

ACKNOWLEDGMENTS

First, I want to thank my advisor Professor Stéphane Willocq for his support during the last year. I could learn a lot from him and he always answered patiently all my questions. His vast knowledge about this project and far beyond was always helpful and he did a great job introducing me into this research project. It was a pleasure to work and interact with him during this project.

I am also very thankful towards Professor Guy Blaylock who introduced me to the working group and who kindly joined my thesis committee.

Also thank you to Ping Tan and Patrick Spradlin, the other two students working on this project as well as to Sridara Dasu and to our coordinator Mark Convery for a very fruitful working atmosphere and a good time.

All the students, post–docs and professors in my research group and beyond made my time at Amherst a fun and interesting learning experience.

For outstanding teaching, I want to thank Professor Eugene Golowich, Professor Guy Blaylock, Professor Stéphane Willocq, Professor Jennie Traschen and Professor Barry Holstein.

Last but not least, I want to thank all my friends and family who supported me whenever they could.

ABSTRACT

MEASUREMENT OF THE BRANCHING FRACTION FOR THE DECAY $B^{\pm} \rightarrow K^{*\pm}\gamma$, $K^{*\pm} \rightarrow K^{\pm}\pi^{0}$ WITH THE BABAR DETECTOR

SEPTEMBER 2003

KARSTEN KÖNEKE

M.S., UNIVERSITY OF MASSACHUSETTS AMHERST

Directed by: Professor Stéphane Willocq

The branching fraction of the radiative penguin B meson decay $B^{\pm} \rightarrow K^{*\pm}\gamma$ is measured at the PEP-II asymmetric energy $e^{+}e^{-}$ collider, operating at a center of momentum energy of 10.58 GeV, the $\Upsilon(4S)$ resonance. This document concentrates on the case $K^{*\pm} \rightarrow K^{\pm}\pi^{0}$; $\pi^{0} \rightarrow \gamma\gamma$. This analysis is based on a dataset of 88.2-million $\Upsilon(4S) \rightarrow B\bar{B}$ events corresponding to 81.3 fb^{-1} collected with the BABAR detector.

TABLE OF CONTENTS

LIST OF TABLES

LIST OF FIGURES

CHAPTER 1

INTRODUCTION

Currently, two high precision experiments designed to study the B-meson sector are running: *BaBar* and *Belle*. Both experiments are very similar, they are both asymmetric energy electron-positron colliders running at a center of momentum (CM) energy of 10.58 GeV. This is the energy of the $\Upsilon(4S)$ resonance, a meson which is a bound state of a b quark and an anti-b quark in the 4S configuration. Both *BaBar* and *Belle* are high luminosity experiments with a current peak luminosity of $6.6 \cdot 10^{33} cm^{-2} s^{-1}$ and $1.1 \cdot 10^{34} cm^{-2} s^{-1}$ respectively.

Also, there is data available from the CLEO collaboration, the previous-generation experiment studying B mesons at an e^+e^- collider. This experiment is a symmetric machine also running at the $\Upsilon(4S)$ resonance. This experiment is acquiring data at a much lower rate, the peak luminosity is about $8.5 \cdot 10^{32} cm^{-2} s^{-1}$.

Furthermore, the two detectors at the Tevatron, CDF and DØ, are also examining the physics in the b-quark system. These two experiments are not as clean as the other three mentioned above since the Tevatron is a hadron collider and thus the initial state is not known like it is in the e^+e^- machines. Also, there are a lot more final state particles in a hadron collider than in a e^+e^- collider. Thus it is much harder to isolate a photon from the rest of the event which will be needed for this analysis.

1.1 Theoretical Motivation

1.1.1 The Standard Model

Nowadays, there is a good model of the physics of elementary particles available, the Standard Model of Elementary Particle Physics (SM). This model is dealing with two types of spin-$\frac{1}{2}$ particles (quarks and leptons) and three types of forces (strong, electromagnetic and weak force) mediated by three different types of force carriers (8 gluons, the photon and the $W^{\pm}$ and Z^0 vector (=spin-1) bosons, respectively). The SM is a gauge theory, the invariance of the SM lagrangian under local transformation belonging to the $U(1)_Y \otimes SU(2)_L$ group yields the electroweak part of the SM and the local transformation belonging to the $SU(3)_C$ group leads to the part of the SM dealing with strong interactions, as described by Quantum Chromo Dynamics (QCD). To be more precise, the required invariance of the lagrangian under these local gauge transformations leads to the three types of force carriers, the vector bosons. Therefore, these force carriers are also known under the name "gauge bosons".

Up to now, the theoretical predictions of the SM agree to a high precision with experimental measurements that it is sometimes frustrating not to see any deviation.

1.1.2 CP Violation in the Standard Model

In the SM, the quark mass (or flavor) matrices are in general not diagonal. In order to transform the quark flavor states into the weak eigenstates needed in the lagrangian, one performs a rotation in the quark flavor space. This rotation of the flavor eigenstates leads to the diagonal weak eigenstates which are used in the lagrangian. This leads to a non-vanishing rotation matrix in the weak charged current term of the lagrangian, the Cabibbo-Kobayashi-Maskawa (CKM) matrix. This unitary matrix is usually interpreted as a redefinition of the down-type eigenstates of the weak interaction (primed) as a linear combination of the down-type flavor eigenstates (unprimed).

$$\begin{pmatrix} d' \\ s' \\ b' \end{pmatrix} = V_{CKM} \cdot \begin{pmatrix} d \\ s \\ b \end{pmatrix} = \begin{pmatrix} V_{ud} & V_{us} & V_{ub} \\ V_{cd} & V_{cs} & V_{cb} \\ V_{td} & V_{ts} & V_{tb} \end{pmatrix} \cdot \begin{pmatrix} d \\ s \\ b \end{pmatrix} \tag{1.1}$$

This CKM matrix is a unitary complex matrix and it has for the case of three quark generations 18 parameters. But since the matrix is unitary, only nine of these 18 parameters are independent. Furthermore, one can always redefine the individual phases of the six quark fields and thus remove five more independent parameters. This leaves us with four independent parameters, three real parameters (angles) and one irreducible phase factor. This phase factor is the source of CP violation in the SM.

With this remaining four independent parameters, one can expand the CKM matrix in a widely known way, the Wolfenstein parameterization of the CKM matrix [1][2]:

$$\begin{pmatrix} V_{ud} & V_{us} & V_{ub} \\ V_{cd} & V_{cs} & V_{cb} \\ V_{td} & V_{ts} & V_{tb} \end{pmatrix} = \begin{pmatrix} 1-\frac{1}{2}\lambda^2 & \lambda & A\lambda^3(\rho - i\eta) \\ -\lambda & 1-\frac{1}{2}\lambda^2 & A\lambda^2 \\ A\lambda^3(1-\rho-i\eta) & -A\lambda^2 & 1 \end{pmatrix} + \mathcal{O}(\lambda^4) \tag{1.2}$$

The unitarity conditions of the CKM matrix are

$$\sum_{i=1}^{3} V_{ji}V_{ki}^* = 0 = \sum_{i=1}^{3} V_{ij}V_{ik}^* \quad for j \neq k. \tag{1.3}$$

These can be visualized with six triangles. But for only two of those the length of all three sides are of the same order of λ ($\lambda \approx |V_{us}| \approx |V_{cd}| \approx 0.22$). One of these two triangles is usually referred to as “The Unitary Triangle” .

There are three types of CP violation known in the Standard Model of elementary particle physics:

- Direct CP violation (also known as CP violation in decay),
- Indirect CP violation (also known as CP violation in mixing), and
- CP violation due to interference between decays with mixing and without mixing.

The last manifestation of CP violation is the experimentally best measured case. This has been measured for instance in the decay $B^0(\bar{B}^0) \to J/\Psi K_s^0$ [3][4].

1.1.3 The $B \to K^*\gamma$ Radiative Penguin Decay

A penguin decay is a flavor changing neutral current (FCNC) process which takes place in the SM only with a loop in the Feynman diagram. The name "penguin decay" was first used as a result of a bet in [5]. In the case of $B \to K^*\gamma$, a W boson and an up-type quark are in the loop (see Figure 1.1).

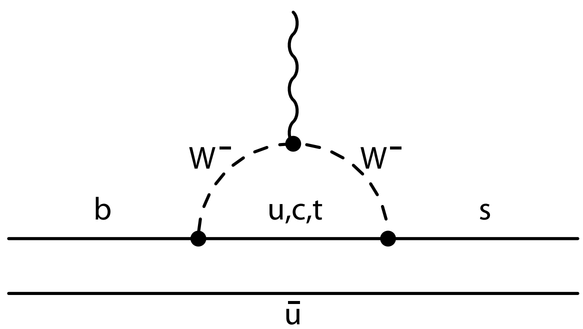

Figure 1.1. Feynman diagram for the $B^\pm \to K^{*\pm}\gamma$ transition. This is the leading order "penguin" diagram for this transition.

There are several interesting motivations to look at this $B \to K^*\gamma$ decay which in leading order proceeds via this electroweak penguin loop. Since the top- and charm-quark penguin diagrams are the largest contributions to this process, this analysis is a probe of the top- and charm-quark couplings. A reasonably clean determination of the ratio of the CKM matrix elements V_{td}/V_{ts} can be calculated from the ratio of branching fractions of the two exclusive radiative penguin decays $B \to \rho\gamma$ and $B \to K^*\gamma$ [6]:

$$\frac{\mathcal{B}(B \to \rho\gamma)}{\mathcal{B}(B \to K^*\gamma)} = S_\rho \left|\frac{V_{td}}{V_{ts}}\right|^2 \frac{\left(1 - m_\rho^2/M^2\right)^3}{\left(1 - m_{K^*}^2/M^2\right)^3} \zeta^2 \left[1 + \Delta R(\rho/K^*)\right] \tag{1.4}$$

where $\zeta = \xi_\perp^\rho(0)/\xi_\perp^{K^*}(0)$ is the ratio of form factors computed in Heavy Quark Effective Theory (HQET), $S_\rho = 1(1/2)$ are isospin weights for the charged (neutral) ρ-meson and $\Delta R(\rho/K^*)$ is a dynamical function calculated in [6] which accounts for vertex, hard-spectator and annihilation contributions. The $B \to \rho\gamma$ decay has not yet been observed, but it is expected to be observed in the near future.

One can easily imagine a new (e.g. supersymmetric) particle in the penguin loop. This non-SM physics contribution could change the branching fraction of this decay measurably. The hopes of discovering non-SM physics in this way were diminished by early measurements (see Chapter 1.2). In fact these measurements agree within errors with the SM predictions (see Table 1.1). The large uncertainties of these theoretical calculations are due to difficulties in calculating the hadronization of the final state mesons. Also QCD corrections to the penguin loop itself are hard to compute.

$\mathcal{B}(B \to K^*\gamma)$ (NLO)	Reference
$(6.8 \pm 2.6) \times 10^{-5}$	Ali and Parkhomenko [6]
$(7.9^{+1.8}_{-1.6}) \times 10^{-5}$	Beneke, Feldmann and Seidel [7]
$(7.09^{+2.47}_{-2.27}) \times 10^{-5}$	Bosch and Buchalla [8]

Table 1.1. Theoretical predictions for the $B \to K^*\gamma$ branching fraction. The calculations are done at next to leading order (NLO) precision).

In order to actually compute the branching fraction, an effective theory is used. In this particular case, the heavy quark effective theory is used. This effective theory integrates out the heavy fields from the full theory. The effective interaction Hamiltonian is [9]

$$\mathcal{H}_{eff} = -\frac{4G_F}{\sqrt{2}} V_{ts}^* V_{tb} \sum_{i=1}^{8} C_i(\mu) Q_i \ , \tag{1.5}$$

where G_F is the Fermi constant, V_{tj} are CKM matrix elements, $C_i(\mu)$ are Wilson coefficient (dependent on the renormalization scale μ) and Q_i are the operators. Unitarity of the CKM matrix has been assumed and everything bejond leading order in α_{em}, m_b/m_W, m_s/m_b and V_{ub}/V_{cb} has been neglected. The short distance QCD effects due to hard gluon exchanges between the quark lines of the leading order one loop Feynman diagram is contained in the Wilson coefficients which can be calculated perturbativly. The Hamiltonian has to be sandwiched between the final $K^{*\pm}$ meson state and the initial $B^{\pm}$ meson state.

The measurement of the branching fraction for the $B \to K^*\gamma$ decay will determine the form factor involved with the calculation of the electroweak penguin transition. A comparison between the pure calculation of this form factor and the calculation with input from the experimentally measured branching fraction will give useful input to the QCD calculations.

Also, the $B \to K^*\gamma$ decay process is a good candidate for the search for direct CP violation. This is due to cancellations of most hadronic uncertainties in the calculation of this CP violating charge asymmetry:

$$A_{CP}(B^+ \to K^{*+}\gamma) = \frac{\Gamma(B^- \to K^{*-}\gamma) - \Gamma(B^+ \to K^{*+}\gamma)}{\Gamma(B^- \to K^{*-}\gamma) + \Gamma(B^+ \to K^{*+}\gamma)}. \tag{1.6}$$

The SM-based theoretical calculations indicate that this asymmetry can be no larger than 1%. Nonetheless, Feynman diagrams with non-SM processes can interfere with the usual SM processes and thus lead to CP violating asymmetries of up to 20%.

1.2 $B \to K^*\gamma$ Branching Fraction Measurements

As of today (August 2003), the current Particle Data Group (PDG) [10] values for the branching fractions for the charged and neutral $B \to K^*\gamma$ decays are averages of two measurements. The first measurement has been done by the CLEOII collaboration in 1999 [11] and the second one is a previous BABAR measurement [12]. There is a new measurement provided by the *Belle* collaboration [13] which is not yet included into the PDG value (see Table 1.2).

Integrated luminosity	CLEOII [11] $9.2 fb^{-1}$	BABAR [12] $20.7 fb^{-1}$	*Belle*[13] $78.0 fb^{-1}$
$\mathcal{B}(B^0 \to K^{*0}\gamma)$ $(\times 10^{-5})$	$4.55^{+0.72}_{-0.68} \pm 0.34$	$4.23 \pm 0.40 \pm 0.22$	$4.09 \pm 0.21 \pm 0.19$
$\mathcal{B}(B^+ \to K^{*+}\gamma)$ $(\times 10^{-5})$	$3.76^{+0.89}_{-0.83} \pm 0.28$	$3.83 \pm 0.62 \pm 0.22$	$4.40 \pm 0.33 \pm 0.24$

Table 1.2. Previous measurements of the branching fractions. The first error is the statistical and the second is the systematical error (absolute values).

Taking the new *Belle* measurement into account, the average value for the branching fraction becomes approximately $(4.0 \pm 0.4) \times 10^{-5}$ (see Table 1.3).

Mode	Assumed branching fractions
$B \to K^*\gamma$	$(4.0 \pm 0.4) \cdot 10^{-5}$
$B \to X_s\gamma$	$(3.6 \pm 0.3) \cdot 10^{-4}$

Table 1.3. Assumed branching fractions for this analysis.

The decay $B \to X_{s(d/u)}\gamma$ is a potential background for this analysis and needs to be understood. The value listed in Table 1.3 is a rounded number from an inclusive BABAR measurement of this branching fraction [14]. The error on this is approximately 10% and the branching fraction will be varied accordingly in order to study systematic effects due to this uncertainty on the analysis.

CHAPTER 2

THE *BaBar* EXPERIMENT

The *BaBar* experiment is based on an asymmetric energy e^+e^- collider at the Stanford Linear Accelerator Center (SLAC) operating at a center of momentum (CM) energy of 10.58 GeV, coinciding with the $\Upsilon(4S)$ resonance. *BaBar* started taking data in 1999 and will continue running most probably beyond 2007.

2.1 The Stanford Linear Accelerator Center

The Stanford Linear Accelerator Center (SLAC) was established in 1962 and is located in Menlo Park, California. In 1966, the main machine went into operation, the main linear accelerator (Linac). This is a three kilometer long electron and positron accelerator now used to inject the electron and positron beams into the PEP-II storage rings. The linac is still the worlds largest and most powerful linear accelerator and it can provide beam energies of up to about 50 GeV. A schematic overview of the experimental site at SLAC can be seen in Figure 2.1.

2.2 The PEP-II Collider

The PEP-II collider is a two storage ring machine. One ring is an upgrade of the previously existing PEP collider which now stores a 9.0 GeV electron beam. The second storage ring is a new ring storing a 3.1 GeV positron beam. The PEP-II collider was completed in July 1998.

The different energies of the electron- and positron beams result into a CM frame which is moving in the laboratory frame with a $\beta\gamma$ Lorentz boost of 0.56. This boost

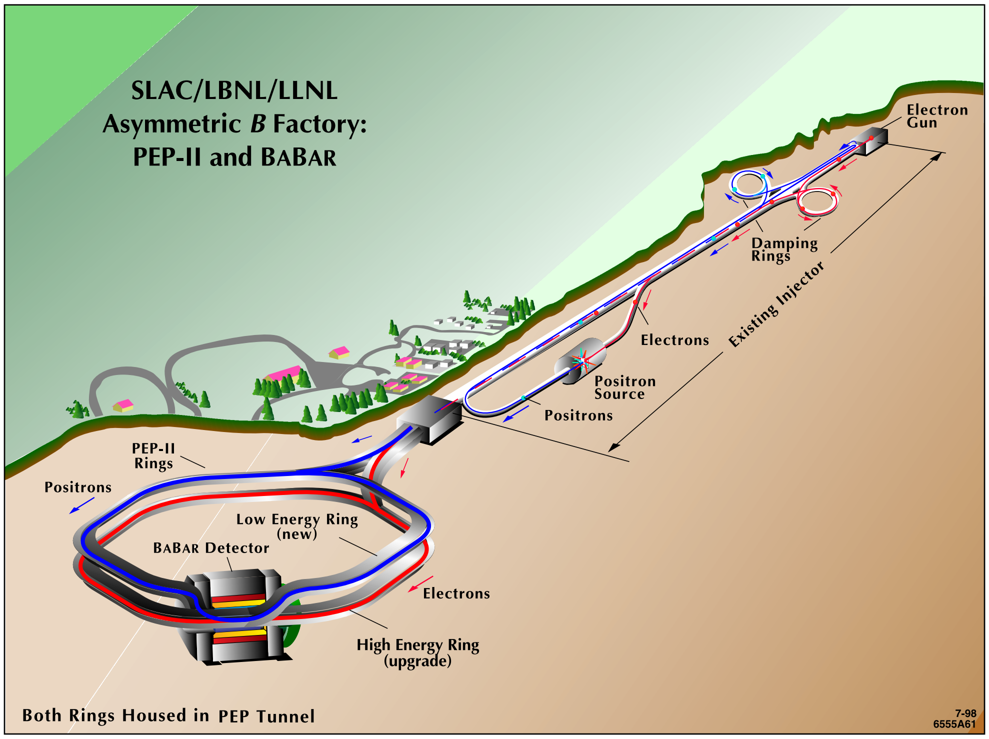

Figure 2.1. A schematic overview of the experimental site at SLAC. (Courtesy of Stanford Linear Accelerator Center)

is crucial to study the B-meson system. Since the $\Upsilon(4S)$ is only about 22 MeV heavier than the two resulting B-mesons, the B-mesons are produced almost at rest in the $\Upsilon(4S)$ rest frame. But with the above mentioned Lorentz boost of the CM frame (which is the $\Upsilon(4S)$ rest frame), it is possible to measure the difference in the decay length of the two B-mesons which is due to a difference in their decay times.

The design peak luminosity of the PEP-II collider is $3 \times 10^{33}\,cm^{-2}s^{-1}$. As of today, the current PEP-II record is $6.106 \times 10^{33}\,cm^{-2}s^{-1}$ (achieved May 2, 2003), which already exceeds this goal by a factor of two. With this high luminosity, there could be about 30–100 million $\Upsilon(4S)$ produced by PEP-II each year with increasing rate.

Figure 2.2. The PEP-II storage ring. The upper ring is the low energy positron ring and the lower ring is the high energy electron ring. (Courtesy of Stanford Linear Accelerator Center)

The two beams in the PEP-II machine collide head on, i.e. there is no crossing angle at the interaction point (IP). And the time between two bunch crossings is 4.2 ns. A picture of the PEP-II storage ring is shown in Figure 2.2.

2.3 The *BaBar* Detector

The *BaBar* detector is a modern high energy particle detector designed specifically for an asymmetric electron positron collider running at the $\Upsilon(4S)$ resonance. Because of the boost along the e^- direction, the detector is asymmetric with respect to the collision point. The forward–backward asymmetry of the detector is designed in such a way that it covers approximately the same solid angle in the forward and backward direction in the CM frame.

I am going to describe the different subsystems of the BaBar detector following a particle produced at the interaction point in the center of the detector to the outermost part of the detector. A schematic overview of the BaBar detector with its subsystems can be seen in Figure 2.3. The information in these sections is coming mostly from "The BaBar Physics Book" [15] and "The BaBar Detector" [16].

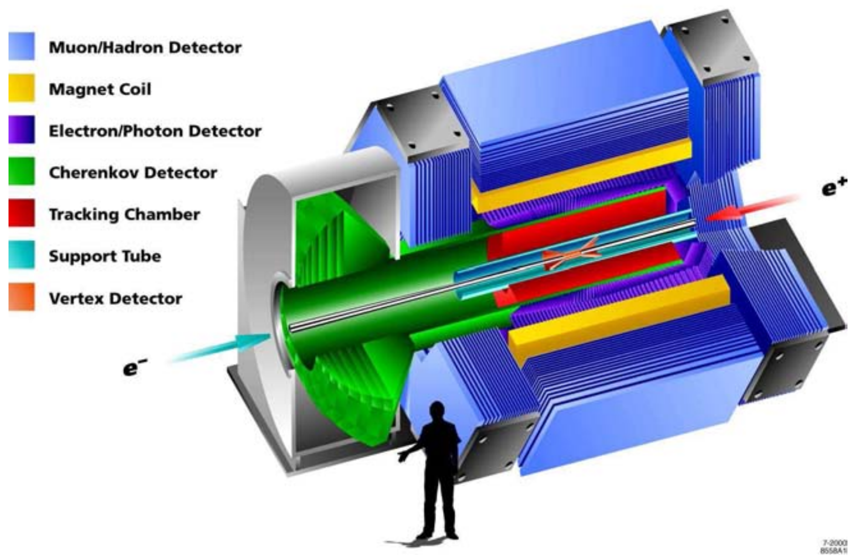

Figure 2.3. The BaBar detector. (Courtesy of Stanford Linear Accelerator Center)

2.3.1 The Silicon Vertex Tracker

The silicon vertex tracker (SVT) is the innermost part of the BaBar detector. It consists of five layers of silicon detectors ordered cylindrically around the beam axis at the interaction point. The innermost layer is in radial direction only 3.3 cm away from the interaction point and the outermost layer is 14.6 cm away. The SVT provides a spatial resolution in the z-direction of less than 70 μm [16] which is absolutely crucial in order to be able to resolve the separated vertices for the two B-mesons and thus being able to study CP-violation in the B-meson system.

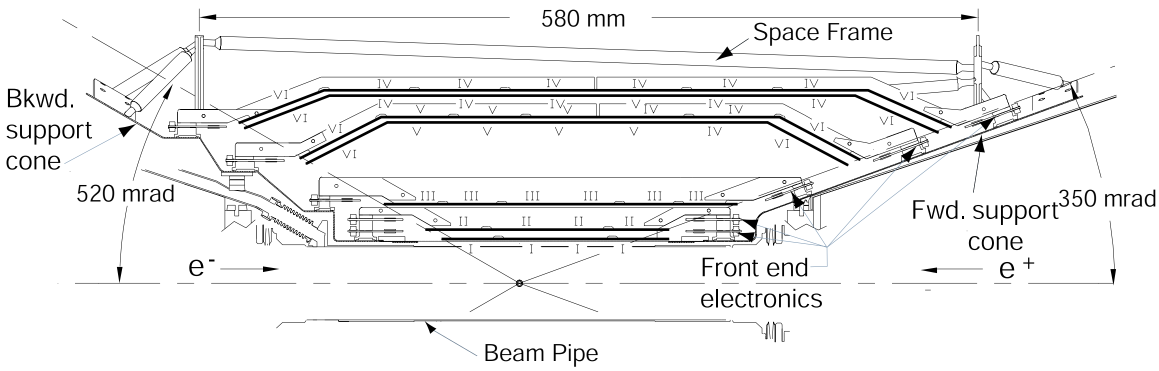

Figure 2.4. The *BaBar* Silicon Vertex Tracker (SVT). (side view) [16]

2.3.2 The Drift Chamber

The *BaBar* drift chamber (DCH) is a 280 cm long cylinder with an inner radius of 23.6 cm and an outer radius of 80.9 cm (see Figure 2.5). The drift chamber is, like other parts of the detector, asymmetric in the forward–backward design in order to account for the asymmetric beam energies. The wires in the tracking volume are arranged in 10 super-layers of 4 layers of wires each, summing up to a total of 40 layers of wires. The super–layers have a slightly different orientation with respect to each other in order to be able to achieve a three-dimensional track reconstruction. The first super–layer is oriented exactly along the beam axis, the second and third one are tilted with an opposite angle with respect to the beam axis. The fourth layer is again oriented along the beam axis and this pattern is continued until the last super–layer is again oriented along the beam axis. The volume around the wires is filled with a Helium–based drift gas. A schematic overview of the DCH is shown in Figure 2.5.

With this configuration, the drift chamber performance for spatial resolution is better than 140 μm. Charged particles produced at the interaction point need at least a transverse momentum of about 100 MeV in order to reach the DCH. The tracking device (SVT and DCH) is located inside of an axial 1.5 T magnetic field.

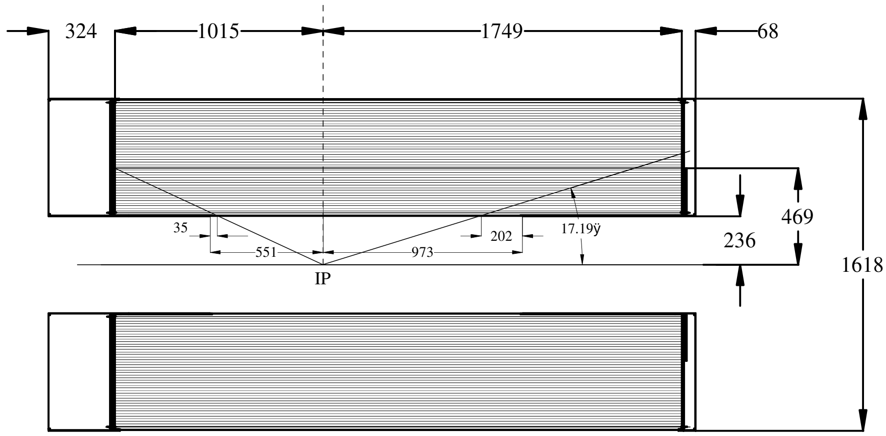

Figure 2.5. The *BaBar* drift chamber (DCH). (side view)

From the curvature of a reconstructed track in the tracking systems of the *BaBar* detector (SVT and DCH), one can deduce the momentum of the associated particle. The Lorentz force acting on a particle with charge q and velocity $\vec{v}$ propagating in a magnetic field $\vec{B}$ is (without the presence of an electric field)

$$\vec{F}_{Lorentz} = q\left(\vec{v} \times \vec{B}\right) \ . \tag{2.1}$$

The centrifugal force is

$$\vec{F}_{centrifugal} = m\frac{|\vec{v}|^2}{r} \ , \tag{2.2}$$

where m is the mass of the particle and r is the radius of the track curvature. Since both forces have equal magnitude and opposite directions, one can combine these two equations and gets a relation between the charge q and the momentum $\vec{p}$ of the particle, the magnetic field, the angle between magnetic field and particle momentum $\alpha_{\vec{B}-\vec{p}}$ and the radius of the track curvature

$$|\vec{p}| = rq\left|\vec{B}\right|\sin\alpha_{\vec{B}-\vec{p}} \ . \tag{2.3}$$

2.3.3 The Detector of Internally Reflected Cherenkov Light

The detector of internally reflected Cherenkov light (DIRC) is designed to separate charged kaons from charged pions. If a charged particle travels in a medium faster than the speed of light in that medium, it emits Cherenkov light. The relation between the momentum of the charged particle and the angle between the particle's flight direction and the Cherenkov light cone emission angle is

$$\cos\theta_{Cherenkov} = \frac{1}{\beta n} \ , \tag{2.4}$$

where $n = 1.473$ is the refraction index of the medium and β is the velocity of the charged particle normalized to the vacuum speed of light.

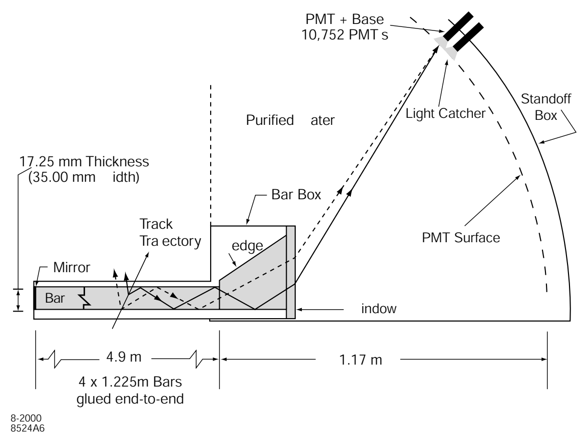

Figure 2.6. The *BaBar* Detector of Internally Reflected Cherenkov Light (DIRC). (side view) [16]

The DIRC is an array of 4.9 m long, 3.5 cm wide and 1.7 cm high bars made of synthetic fused silica, a translucent material in which Cherenkov light can be produced. There are a total of 144 bars arranged in 12 groups of 12 bars each. The Cherenkov light travels inside these bars towards a toroidal water tank at the backward end of the detector. The emission angle is preserved in these internat reflections due to the high accuracy of the parallel quartz–bar surfaces. Finally, an array of photomultiplier tubes detects the Cherenkov light at the backward end of this water tank. From the position and time of the detection in the photomultiplier tubes, an image of the initially produced Cherenkov light cone is inferred. This process is illustrated in Figure 2.6.

The separation between charged pions and kaons relies on their different masses. With the same momentum (measured by the tracking devices, see Sections 2.3.1 and 2.5), particles with different masses have different velocities and thus produce Cherenkov light at different angles. The separation only works if the charged particles are faster than the speed of light in the bars. A charged pion starts producing Cherenkov light if its momentum is larger than 129 MeV/c and a charged kaon has to have a momentum larger than 457 MeV/c in order to produce Cherenkov light. The number of Cherenkov photons produced increases with the momentum of the charged particle and a sufficient number of photons is needed in order to separate them from the background. Thus, charged pions can be separated from charged kaons reliably only, if the momentum of these particles is larger than about 600 MeV.

2.3.4 The Electromagnetic Calorimeter

The electromagnetic calorimeter (EMC) is an array of 6580 Thallium-doped Cesium-Iodide (CsI(Tl)) crystals. This part of the detector covers a polar angle of $-0.775 \leq \cos(\theta) \leq 0.962$ in the laboratory frame, corresponding to $-0.916 \leq \cos(\theta) \leq 0.895$ in the center of momentum frame. If a particle hits the very forward or backward end of the EMC, a part of the energy of this particle will not be deposited in a crystal of the EMC. Some of this particle energy will escape on these edges of the EMC. Thus, for analysis purposes, the solid angle coverage is slightly smaller. Two photodiodes are mounted at the rear end of each crystal. These photodiodes convert scintillation light produced by an electromagnetic shower inside the crystals into a measurable electric pulse. In the radial direction, the calorimeter is placed between the DIRC and the magnet cryostat. A schematic overview of the EMC design is shown in Figure 2.7.

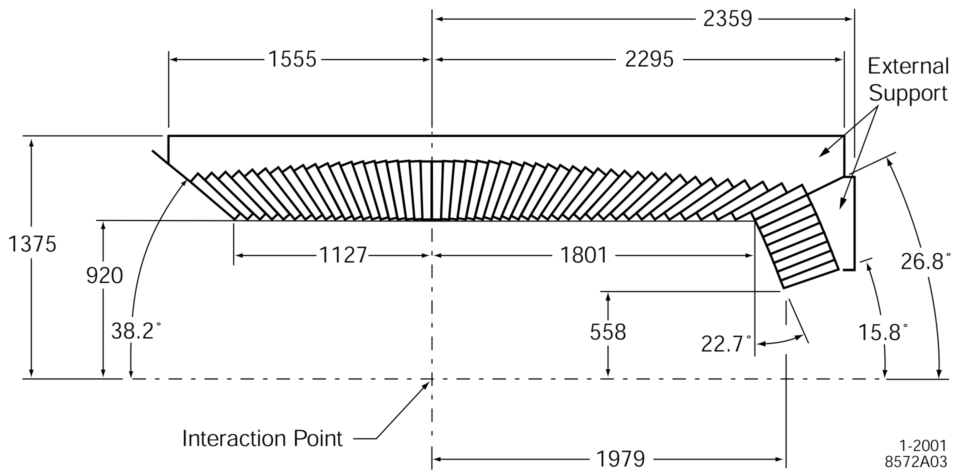

Figure 2.7. The *BaBar* Electromagnetic Calorimeter (EMC). (side view) [16]

The EMC is designed to be capable of detecting photons (coming from π^0 and η decays) very efficiently in the energy range of 20 MeV up to 9 GeV. The design energy resolution is of the order of 1-2%. Also a high angular resolution was a design goal. The achieved position resolution of a few mm translates into an angular resolution of a few mrad. The energy–dependent resolutions are for the energy resolution ($\oplus$ means sum in quadrature)

$$\frac{\sigma_E}{E} = \frac{a}{\sqrt[4]{E(\,\mathrm{GeV})}} \oplus b \tag{2.5}$$

and for the angular resolution

$$\sigma_\theta = \sigma_\phi = \frac{c}{\sqrt{E(\,\mathrm{GeV})}} + d \tag{2.6}$$

with $a = (2.32 \pm 0.30)\,\%$, $b = (1.85 \pm 0.12)\,\%$, $c = (3.87 \pm 0.07)\,mrad$ and $d = (0.00 \pm 0.04)\,mrad$ [16].

The crystals are arranged in two sections. The first section is a cylindrical arrangement of 48 rings with 120 crystals each. This barrel covers in polar angle in the laboratory frame $-0.775 \leq \cos(\theta) \leq 0.892$. A conical end cap consisting of 8 rings with a total of 820 crystals is mounted in addition in the forward direction. This end cap covers in the forward direction in the laboratory frame $0.893 \leq \cos(\theta) \leq 0.962$ in polar angle. The gap between barrel and end cap is of the order of 2 mm.

Most of the support structure and all of the electronics is mounted at the radial outer end of the crystals in order to minimize the material in front of the crystals. This results in less than $0.3 - 0.6\,X_0$(radiation length) in front of the crystals.

2.3.5 The Instrumented Flux Return

The outer part of the *BaBar* detector has three main purposes:

- Magnetic flux return in the iron yoke,
- Muon detection,
- Neutral hadron detection.

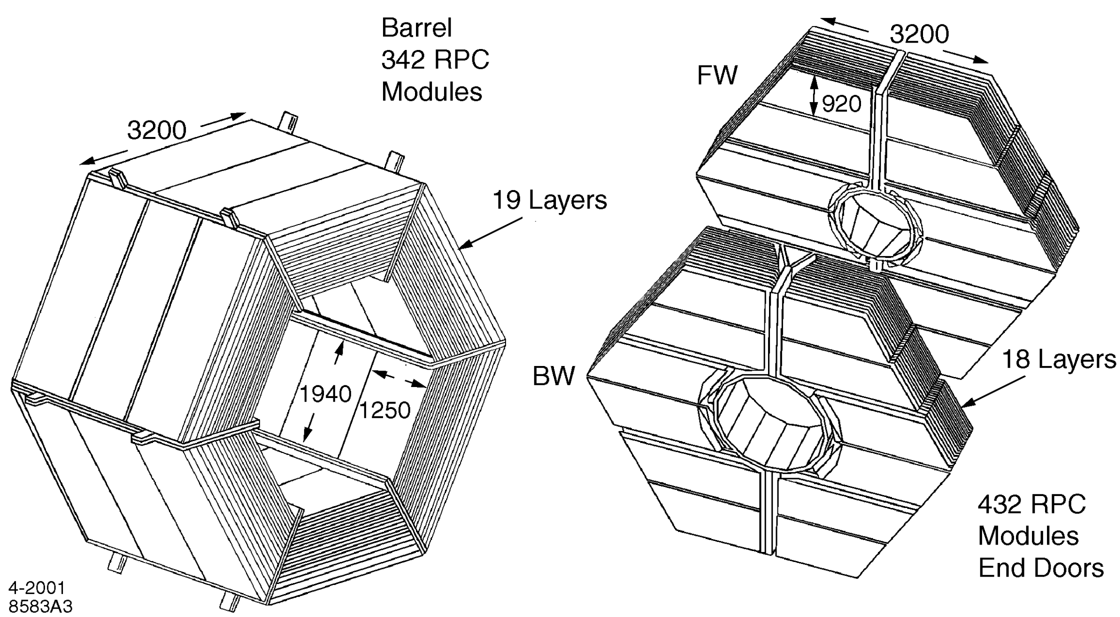

Figure 2.8. The *BaBar* Instrumented Flux Return (IFR). [16]

The Instrumented Flux Return (IFR) consists of a barrel and two end caps. The iron for the magnetic yoke is in radial direction separated into 18 plates. In the barrel, the nine innermost plates are 2 cm thick and 3.5 cm apart, the next four plates are 3 cm thick and 3.2 cm apart followed by three 5 cm thick plates and two 10 cm thick plates, all 3.2 cm apart. The end caps have a similar layout, the two differences are that all plates are 3.2 cm apart and that the outer two plates are 5 cm and 10 cm thick. The barrel is furthermore segmented in azimuthal direction into six sectors forming a uniform hexagon. The two end caps as well as the barrel layout can be seen if Figure 2.8.

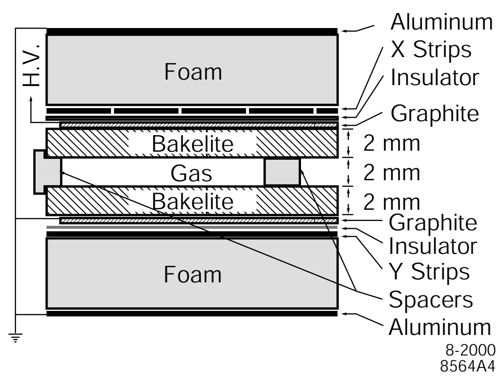

Figure 2.9. The *BaBar* Resistive Plate Counters (RPCs). These particle detectors are mounted in the gaps between the iron plates of the IFR [16].

The gaps between the iron plates are instrumented with resistive plate counters (RPCs) [17] in order to detect muons and neutral hadrons. The basic layout of these RPCs is the following: Two graphite plates are separated by a 6 mm thin gap. One of the plates is electrically grounded and the other is at an 8 kV electric potential. In between these two graphite plates is first a 2 mm thin layer of a bakelite with a high bulk resistivity ($10^{10} - 10^{11} \Omega\,\mathrm{cm}$), followed by a 2 mm thin gap filled with a gas with high absorption coefficient for ultraviolet light, followed by another 2 mm thin layer of the same bakelite. Aluminum strips are glued on the outside of the graphite plates, separated by an insulator. The signal is read out capacitively from these strips. The design of the RPCs can be seen in Figure 2.9.

A signal is induced when a charged particle traverses the RPC. The charged particle can either be a muon coming from the inside of the detector or a charged particle coming from a hadronic shower due to a hadron interacting in the material of the IFR (or upstream). A discharge is produced at the point where the charged particle traversed the gas, due to the high electric field. When the discharge occurs, the electrons travel to the electrode and ionize more gas molecules on their way. When they arrive at the bakelite, they remain there for a sufficient time due to the high resistivity of the bakelite and locally, there is now only an electric field between the surface of the bakelite facing the gas gap (where the electrons accumulated) and the graphite electrode on the other side of the bakelite. But there is no electric field in the gas any more, thus the discharge is stopped. On the other hand, the high absorption coefficient for ultraviolet light of the gas prevents photons of this discharge to travel in the gas and produce a secondary discharge away from the primary one. Since the spacing between the two charges (the graphite electrode on one side and the accumulated electrons on the other side) differs from the larger distance between the two graphite plates, the capacitance of this system changes and this signal is read out by the strips on the outside.

CHAPTER 3

ANALYSIS OVERVIEW

3.1 Introduction

This analysis has been done in collaboration with Mark Convery (Stanford Linear Accelerator Center), Ping Tan and Sridhara Dasu (University of Wisconsin, Madison), Patrick Spradlin (University of California, Santa Cruz) and my advisor Stéphane Willocq (University of Massachusetts, Amherst). We reconstructed four different K^* decay modes: $K^{*0} \rightarrow K^+\pi^-$ (Patrick Spradlin), $K^{*0} \rightarrow K^0_s\pi^0$ and $K^{*+} \rightarrow K^0_s\pi^+$ (Ping Tan) and $K^{*+} \rightarrow K^+\pi^0$, which I have performed and which this document is dealing with.

3.2 Event Signatures

The most striking signature of a $B \rightarrow K^*\gamma$ decay is the presence of a very high-energy photon in the event. In the system of the B meson decaying into the signal mode, the photon energy is about half the B meson mass. This still holds for the center of momentum (CM) frame of the whole event since the B mesons have only a momentum of 341 MeV/c in the CM frame. In each event, the highest energy photon is selected and required to have an energy between 1.5 GeV and 3.5 GeV in the CM frame. A photon is a cluster in the electromagnetic calorimeter with no associated charged track.

Also, the event has to contain a well–reconstructed charged track which is identified as a kaon. The excellent charged particle identification capabilities of the BaBar detector will be very useful for this analysis. The most important information for

Kaon identification is provided by the DIRC; in addition, dE/dx information from the drift chamber is used to distinguish different types of charged particles.

The last particle needed to be able to reconstruct the signal B meson is a π^0. The $\pi^0 s$ can be obtained by computing the invariant mass of any pair of photons in the event (which have to fulfill some quality requirements) and requiring that the computed invariant mass of this photon pair be close to the nominal π^0 mass of $(134.9766 \pm 0.0006)\,\mathrm{MeV}/c^2$ [10].

3.3 Major Backgrounds

The major background for this analysis originates from $e^+e^- \to q\bar{q}$ events (where q = u,d,s,c). The most outstanding signature of a signal event, the high-energy photon, can be mimicked in the following ways:

- The process $e^+e^- \to q\bar{q}\gamma$ can occur due to initial state radiation (ISR) or final state radiation. In particular, a photon due to ISR can have very high energy and thus fake a photon from a signal event.

- The high-energy photon can be a decay product of a high-energy $\pi^0(\eta)$. This high-energy $\pi^0(\eta)$ can decay into a photon pair with very asymmetric energies and the low-energy photon can be lost, e.g. by going along the beam pipe. Or the two photons from the high-energy $\pi^0(\eta)$ can be in the same cluster in the calorimeter and thus be identified as only one photon.

Due to the jetlike structure of these so-called continuum events, the high-energy photon is highly correlated with the energy flow of the rest of the event. This is not the case for an isotropic signal event since the B mesons have only a momentum of about $341\,\mathrm{MeV}/c$ in the CM frame.

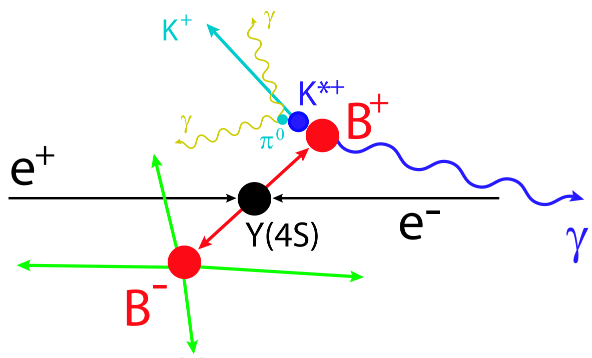

(a) A signal event.

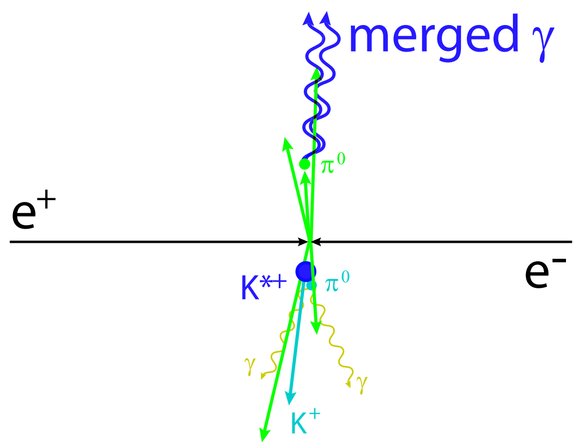

(b) A continuum background event with a high energy π^0.

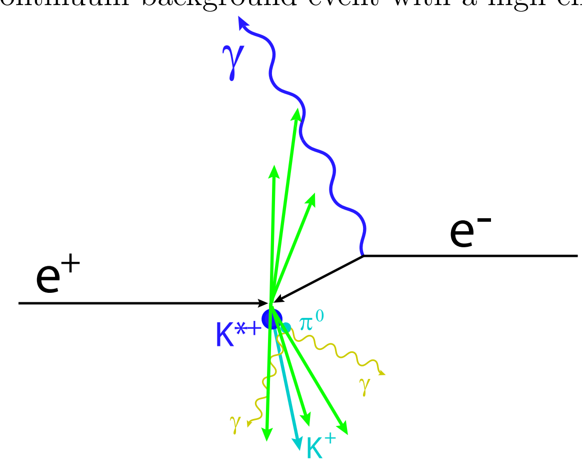

(c) A continuum background event with ISR.

Figure 3.1. Event signatures. All plots are shown in the CM frame.

3.4 Expected Yields

Using the assumed branching fraction for $B \to K^*\gamma$ of $(4.0 \pm 0.4) \times 10^{-5}$ (see Section 1.2), one expects in the total dataset of 81.3 fb^{-1} a total number of 3530 ± 353 $B^+ \to K^{*+}\gamma + c.c.$ events. Due to the isospin factor of 1/3, the expected total number of $B^+ \to K^{*+}\gamma,\ K^{*+} \to K^+\pi^0\ +\ c.c.$ events is thus 1177 ± 118. With the hope of increasing the efficiency from the previous BaBar measurement [12] from 12.9% for this mode to about (16-20)%, the number of expected observed signal events would be $(188-235)^{+24}_{-19}$. The errors stated here are simply the 10% uncertainty of the assumed branching fraction.

Also, the continuum background suppression is expected to be improved by a factor of 1.5–2 due to the combination of signal–background separating variables in a neural network similar to the one used in the $B \to \rho\gamma$ analysis performed by BaBar [18].

3.5 A Blind Analysis

This analysis is done "blind" which means that all the analysis optimizations and considerations are based on so called Monte Carlo (MC) simulations (see Section 3.6.1) of the physics at the particle level and their interaction with each other and the detector material. Only at the very end, after the whole analysis procedure is fixed, the real data (see Section 3.6.2) is used instead of the Monte Carlo. The continuum Monte Carlo (see Section 3.6.1) can be verified with offpeak data. Offpeak data has been collected in a mode where the collision energy $\sqrt{s}$ is reduced by 40 MeV. This is sufficiently away from the $\Upsilon(4S)$ resonance so that no B mesons can be produced any more. Therefore, there cannot be a signal event in the offpeak data.

Since Monte Carlo is a computer simulation, the type of a generated particle is truly known. This Monte Carlo truth information is used to optimize the analysis with respect to the efficiency of the true signal events (referred to as truth matched MC hereafter).

3.6 Data Samples

3.6.1 Monte Carlo

In this analysis, Monte Carlo simulations have been used (they are referred to as SP4 Monte Carlo or simply MC in the remainder of this thesis). The samples are listed in Table 3.1. All $B \rightarrow K^{*}\gamma$ and $B \rightarrow X_{s(d/u)}\gamma$ events have been excluded from the generic B Monte Carlo samples. Furthermore, all $B^{+} \rightarrow K^{*+}\gamma$, $K^{*+} \rightarrow K^{+}\pi^{0}$ events have been excluded from the $B^{+} \rightarrow K^{*+}\gamma$ generic Monte Carlo sample. Also, a cut on the generated hadronic mass $> 1.1\,\mathrm{GeV}/c^{2}$ has been applied for the generic $B \rightarrow X_{s(d/u)}\gamma$ Monte Carlo samples. The nominal $B \rightarrow X_{s(d/u)}\gamma$ samples are the ones with the b-quark mass hypothesis of $m_b = 4.80\,\mathrm{GeV}/c^{2}$. Samples with different b-quark masses have been used for systematic studies or to gain more statistics where necessary. When the word "generic" is used, it means that the particle decays into all possible modes according to the Particle Data Group (PDG) [10], this is also true for the $B \rightarrow K^{*}\gamma$ generic Monte Carlo simulations; here, the K^{*} decays into all possible final states.

3.6.2 Real Data

The real data used for this analysis is the combined RUN1 and RUN2 dataset. The total number of onpeak events of this combined dataset is 1.1×10^{9}. Within that sample, there are $(88.2 \pm 1) \times 10^{6}$ $\Upsilon(4S) \rightarrow B\bar{B}$ events, which corresponds to an integrated luminosity of 81.3 fb^{-1}(see Table 3.1). An equal B^{+}/B^{0} production at the $\Upsilon(4S)$ resonance has been assumed .

Mode	Amount (events)	Integrated luminosity (fb^{-1})	Production cross section (nb)
$B^0 \to K^{*0}\gamma,\ K^{*0} \to K^+\pi^-\ +\ c.c.$	$72,000$	$2,571.4$	1.05
$B^0 \to K^{*0}\gamma,\ K^{*0} \to K_s^0\pi^0\ +\ c.c.$	$16,000$	$3,341.7$	1.05
$B^+ \to K^{*+}\gamma,\ K^{*+} \to K^+\pi^0\ +\ c.c.$	$18,000$	$1,285.7$	1.05
$B^+ \to K^{*+}\gamma,\ K^{*+} \to K_s^0\pi^+\ +\ c.c.$	$16,000$	$1,663.5$	1.05
$e^+e^- \to c\bar{c}$	$56,817,800$	42.1	1.30
$e^+e^- \to u\bar{u}, d\bar{d}, s\bar{s}$	$83,392,000$	39.9	2.09
$e^+e^- \to \tau^+\tau^-$	$42,958,300$	45.7	0.94
$B^0\overline{B}^0$ *generic*	$155,287,100$	295.8	1.05
B^+B^- *generic*	$150,426,700$	286.5	1.05
$B^0 \to K^{*0}\gamma$ *generic* $+\ c.c.$	$108,000$	2571.4	1.05
$B^+ \to K^{*+}\gamma$ *generic* $+\ c.c.$	$114,000$	2714.3	1.05
$B^0 \to X_{sd}\gamma\ +\ c.c.\ (m_b = 4.80\,\mathrm{GeV})^{1)}$	$110,000$	291.0	1.05
$B^0 \to X_{sd}\gamma\ +\ c.c.\ (m_b = 4.65\,\mathrm{GeV})$	$78,000$	206.3	1.05
$B^0 \to X_{sd}\gamma\ +\ c.c.\ (m_b = 4.75\,\mathrm{GeV})$	$18,000$	47.6	1.05
$B^0 \to X_{sd}\gamma\ +\ c.c.\ (m_b = 4.95\,\mathrm{GeV})$	$76,000$	201.1	1.05
$B^+ \to X_{su}\gamma\ +\ c.c.\ (m_b = 4.80\,\mathrm{GeV})^{1)}$	$106,000$	280.4	1.05
$B^+ \to X_{su}\gamma\ +\ c.c.\ (m_b = 4.65\,\mathrm{GeV})$	$72,000$	190.5	1.05
$B^+ \to X_{su}\gamma\ +\ c.c.\ (m_b = 4.75\,\mathrm{GeV})$	$18,000$	47.6	1.05
$B^+ \to X_{su}\gamma\ +\ c.c.\ (m_b = 4.95\,\mathrm{GeV})$	$76,000$	201.1	1.05
Off–Peak data	$117,041,128$	9.49	
On–Peak data	$1,093,418,668$	81.3	

Table 3.1. Monte Carlo and data samples used in this analysis. (Second column: Total numbers; Third column: Corresponding integrated luminosity; Fourth column: Assumed production cross-section at the $\Upsilon(4S)$ resonance. [15]). $^{1)}$Nominal samples.

CHAPTER 4

EVENT SELECTION

4.1 Skim Requirements

The skim requirements are cuts which keep most of the signal events but remove events from the continuum like bhabhas, radiative bhabhas, dimuons and probably most important many hadronic events with no high–energy photon.

4.1.1 Number of Reconstructed Tracks

The first requirement is that there be at least two charged tracks in the event which fulfill the following criteria (referred to as "GoodTracksLoose" (GTL) criteria in *BaBar* lingo):

- The number of hits in the drift chamber (DCH, see Section 2.3.2) must be more than 12.
- The transverse momentum must be larger than 100 MeV/c.
- The track must have come closer than 1.5 cm to the beam axis.
- The track must have come closer than 10 cm to the nominal beam spot, measured along the z (beam) direction.
- The momentum of the track must be less than 10 GeV/c.

The first two requirements ensure that the particle traverses a sufficiently long path through the tracking device (SVT and DCH) to be reliably reconstructed. The last three requirements ensure that the track is not due to a cosmic ray event.

4.1.2 R_2

Also, the ratio R_2 of the 2^{nd} to the 0^{th} Fox-Wolfram moment is computed in the CM frame as

$$R_2 = \frac{H_2}{H_0}, \tag{4.1}$$

with H_l being the Fox-Wolfram moment defined in [19] as

$$H_l = \sum_{i,\ j} \frac{|\vec{p}_i|\,|\vec{p}_j|}{s} P_l(\cos\phi_{ij}), \tag{4.2}$$

where $\vec{p}_{i/j}$ are the momenta of two particles in the CM frame, ϕ_{ij} is the angle between these two momenta, P_l are Legendre polynomials and s is the square of the CM energy. R_2 is required to be less than 0.9. This removes some portion of continuum background events since it is a measure of an event being jetlike. Continuum background events ($e^+e^- \to f\bar{f}$, where f = u, d, s, c or a charged lepton) are in the CM frame in general two rather collimated bunches of particles back to back. This is due to the large excess of kinetic energy and the conservation of energy and momentum. On the other hand, $e^+e^- \to \Upsilon(4S) \to B\bar{B}$ events are almost isotropic since the $\Upsilon(4S)$ resonance is only about $20\,\mathrm{MeV}/c^2$ heavier than the sum of the two B meson masses and thus there is almost no excess of kinetic energy available which could go into the momenta of the B mesons.

4.1.3 Energy of the Highest Energy Photon

In a signal event, the decay of the B meson is a two–body decay into a $K^{*\pm}$ meson and a high energy photon. Thus, the energy of this photon is in the rest frame of the B meson approximately half of the B meson mass. Furthermore, since the B meson has a very low momentum in the CM frame due to the small mass difference between the $\Upsilon(4S)$ and the sum of two B mesons, the energy of this photon is also in the CM frame approximately half of the B meson mass. Thus, the CM energy distribution of the high energy photon peaks at approximately half of the B mass, with a long tail on the low energy side due to missing energy in the calorimeter. Thus a cut on the energy of the highest energy photon in the event is applied to suppress continuum events with no high energy photon, π^0 or η, and $e^+e^- \to \gamma\gamma$ events. The requirement on the highest energy photon in the event is thus $1.5\,\mathrm{GeV} < E_{\gamma\ high} < 3.5\,\mathrm{GeV}$. This cut is rather loose as can be seen in Figure 4.1 (c). Since the photon CM momentum is used to compute m_{ES} (see Section 4.6), a tight cut on the CM energy would be correlated with m_{ES} (the momentum and the energy are the same for a massless particle like the photon). A correlation of m_{ES} with any other variable is not wanted since this variable is used in the fit.

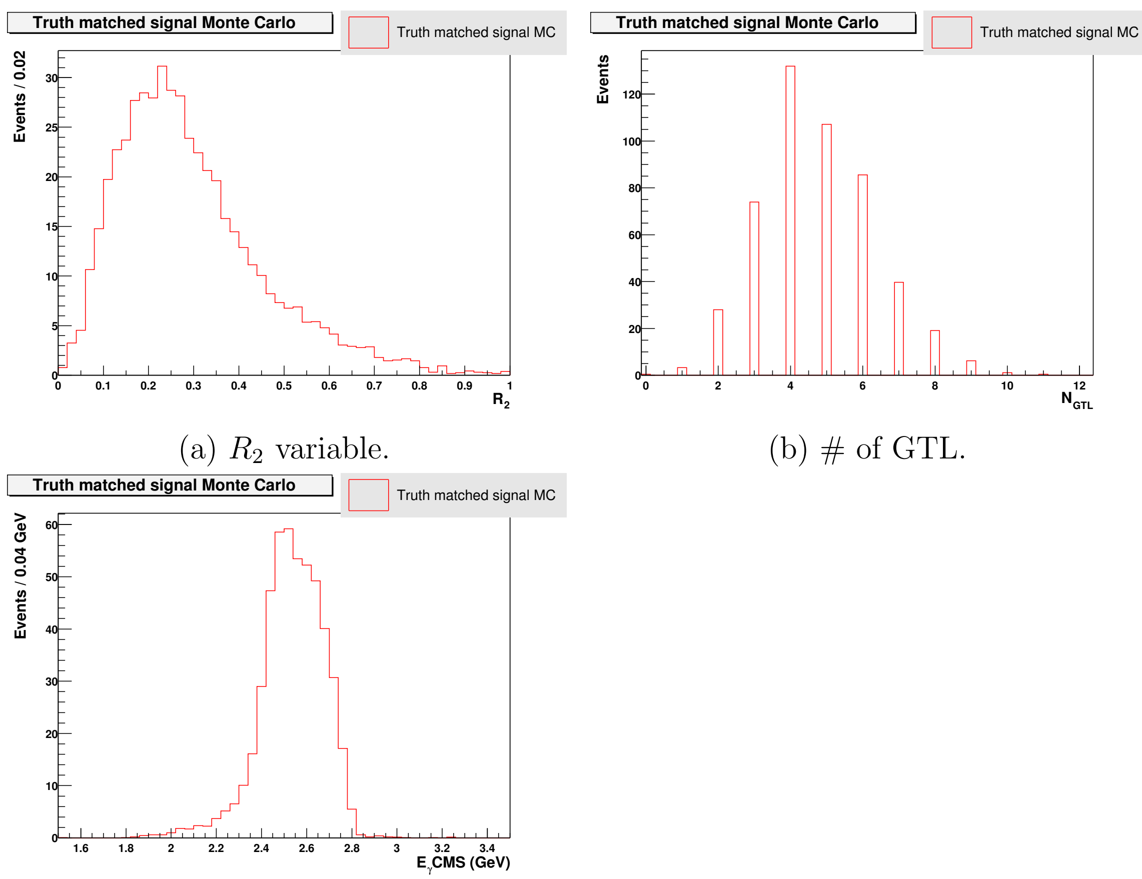

(a) R_2 variable.

(b) # of GTL.

(c) E_γ in the CM frame.

Figure 4.1. Skim variables for truth matched signal Monte Carlo. No cuts are applied.

4.2 High Energy Photon Selection

The high energy photon is detected as an energy deposition in the EMC (see Section 2.3.4). A photon produces an electromagnetic shower via pair production in the crystals of the EMC. In general, this electromagnetic shower spreads out over several EMC crystals. A number of adjoining (connected at at least one corner) crystals with energy deposited in them is called a cluster. A local maximum (bump) within this cluster is identified as a photon, if no charged track points directly to it.

Besides the requirement of the CM energy of the photon being in the range 1.5–3.5 GeV (see Section 4.1.3), there are further requirements which shall ensure that it is indeed a high energy photon coming directly from a two–body B meson decay.

- The cluster in the EMC caused by the photon is required not to have any noisy or dead channels.
- If a noisy crystal is overlooked by the EMC monitoring, it can fake an energy deposition and thus a photon. Because of this, it is required that the photon has deposited energy in more than four crystals with a circular lateral energy distribution.
- A single photon causes a shower and thus the distribution of energy deposited in the crystals is circular around the centroid of the bump. The energy deposition caused by two very close photons (e.g. a π^0 or η decay with very collimated decay product photons due to Lorentz boost) is more ellipsoidal. This is measured by the second moment variable defined as

$$L_2 = \sum_{crystal\ i} \frac{E_i \left[(\theta_i - \theta_C)^2 + (\phi_i - \phi_C)^2 \right]}{\sum_i E_i}, \tag{4.3}$$

  where θ_C and ϕ_C are the angular coordinates of the centroid of the bump and θ_i and ϕ_i are the angular coordinates of the ith crystal of the bump. A bump caused by a single photon has a smaller second moment than a bump caused by two photons. Thus, the second moment of the photon is required to be less than 0.002 $(\text{mrad})^2$.

- The EMC covers a polar angle of $-0.775 \leq \cos(\theta) \leq 0.962$ in the laboratory frame. An electromagnetic shower spreads out over several crystals in the EMC. In order to ensure that the shower is fully contained inside, the photon is required to be away from the edges of the EMC. Furthermore, the photon needs to be within the acceptance of the tracking device (SVT and DCH, Sections 2.3.1 and 2.3.2 respectively) in order to ensure that the energy deposited in the EMC is not due to a charged track. Also, beam backgrounds are possible sources of energy deposition in the EMC close to the beam pipe. Thus, the photon is required to be within $-0.74 \leq \cos(\theta) \leq 0.93$ in the laboratory frame.

- The closest charged or neutral bump is required to be at least 25 cm away from the centroid of the bump caused by the photon in consideration. This requirement reduces contamination due to hadronic split off as well as high energy π^0s and ηs decaying into a close pair of photons. A hadronic split of is a hadron producing a hadronic shower inside the calorimeter and one of the hadrons in this shower traverses a few crystals before inducing a secondary hadronic shower. The crystals detecting the secondary hadronic shower are not necessarily connected to the crystals detecting the primary shower.

- As already mentioned π^0 and η decays constitute a major background source for the high energy photon. Therefore, the high energy photon is required not to be consistent with originating from a π^0 or η decay. Therefore, the photon is paired with all other photons in the event, provided their energies are more than 50 MeV for the π^0 veto and more than 250 MeV for the η veto. The threshold energies for the other photon reduce spurious combinations with low energy background photons. The higher threshold for the photon from η decays is due to higher mass of the η and thus the decay products (photons) have higher energy. The two–photon invariant mass windows which have been vetoed are [0.115—0.155] GeV/c^2 for the π^0 veto and [0.505—0.587] GeV/c^2 for the η veto.

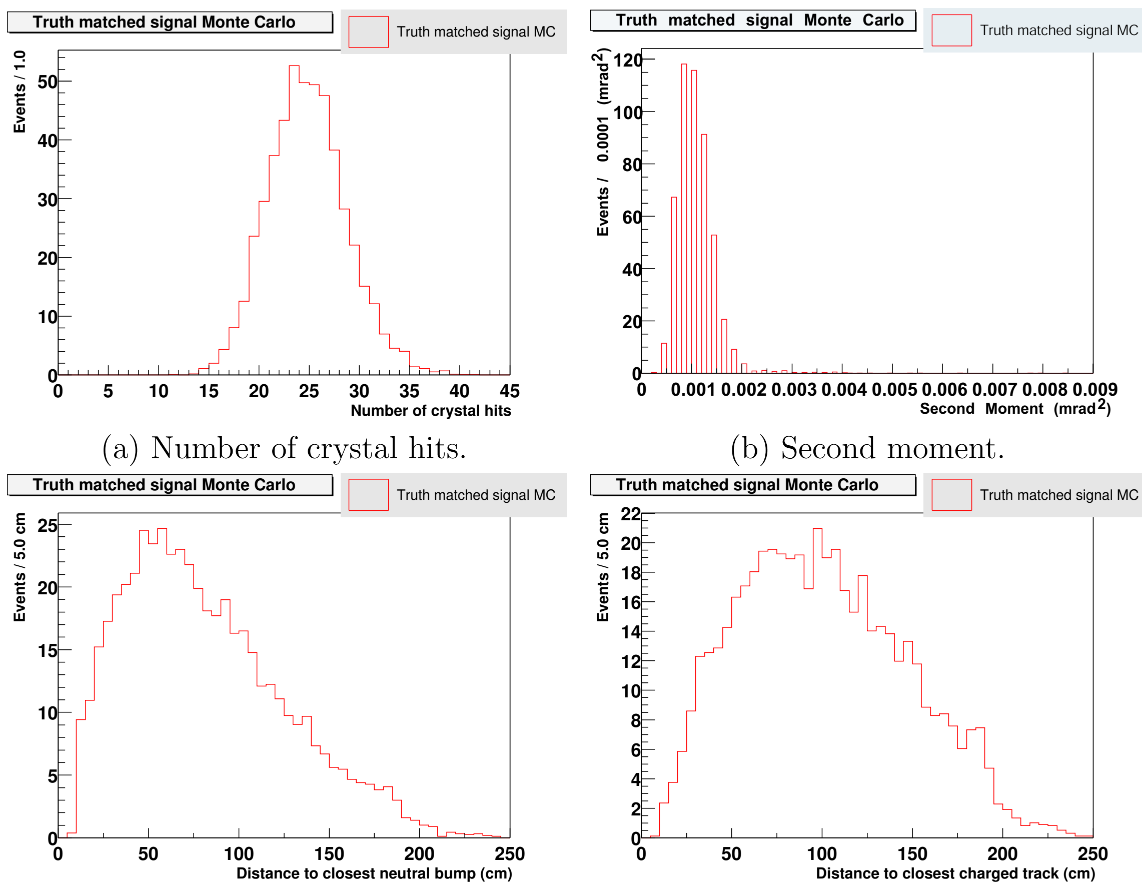

(a) Number of crystal hits.

(b) Second moment.

(c) Distance to closest neutral bump.

(d) Distance to closest charged track.

Figure 4.2. High–energy photon quality variables. Shown is truth matched signal Monte Carlo only.

4.3 π^0 Selection

In order to reconstruct a π^0, the four-momenta of two photons (EMC bumps with no associated charged track) are combined. There are two requirements on these two photons:

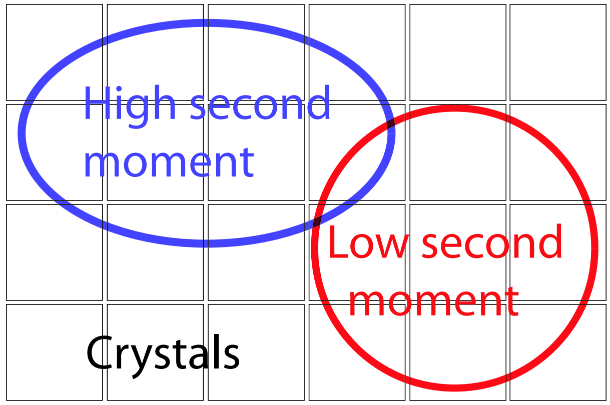

Figure 4.3. Illustration of the second moment variable. The low second moment is caused by a single photon and thus circular. If two photons hit the EMC very close, an elliptical distribution and thus a higher second moment is the result.

- They are both required to have an energy of at least 30 MeV. This cut is applied in order to reduce beam–related background photons or noise in the EMC electronics.
- Also, both photons are required to have a LAT of less than 0.8, where the LAT is a shape variable defined in Section 4.3.1.

Furthermore, the resulting π^0 candidate has to have an energy greater than 200 MeV in the laboratory frame. A π^0 mass constrained fit is applied to improve the π^0 energy resolution. A cut on the "unfitted" mass of [115—150] MeV/c^2 has also been applied. The two–photon invariant mass after all π^0 selection cuts is shown in Figure 4.4, together with the momentum distribution of the π^0s in the CM frame.

4.3.1 The Lateral Shower Shape

Electromagnetic showers have a different lateral energy distribution than hadronic showers. In general, a hadronic shower has a wider lateral distribution. This difference can be quantified in the LAT variable defined as [20]

$$LAT = \frac{\sum_{i=3}^{N} E_i r_i^2}{\sum_{i=3}^{N} E_i r_i^2 + E_1 r_0^2 + E_2 r_0^2}, \tag{4.4}$$

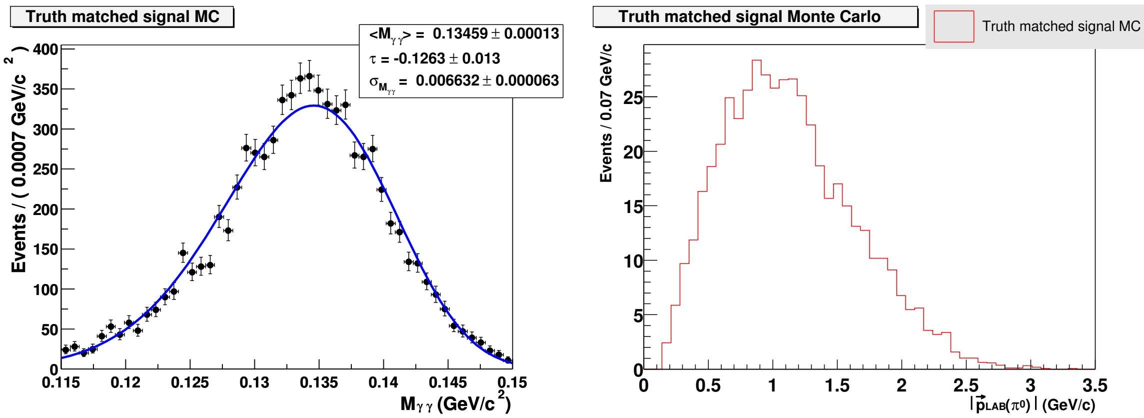

(a) $\gamma\gamma$ mass peak.

(b) π^0 candidate momentum.

Figure 4.4. $\gamma\gamma$-mass peak and momentum for π^0 candidates in signal MC. (a) A novosibirsk function has been fitted to the $\gamma\gamma$ invariant mass peak. (b) The momentum of the π^0 candidate in the laboratory frame. The π^0-candidate is Monte Carlo truth matched. No cuts are applied in order to gain statistics.

where

- N is the number of crystals hit by the shower,
- E_i is the energy deposited in the i-th crystal, ordered in decreasing energy starting with 1 being the highest energy.
- r_i is the lateral radius between the centroid of the shower and the i-th crystal,
- $r_0 = 5\,\text{cm}$, which is roughly the width of a crystal and thus the distance between two crystal centers.

Since the Molière radius for the CsI(Tl) crystals of the EMC is 3.8 cm, most of the energy of an electromagnetic shower is deposited within only 2–4 crystals. This is not the case for a hadronic shower. A hadronic shower spreads out over more crystals in the EMC and thus the LAT variable is on average larger than for an electromagnetic shower.

4.4 Kaon Selection

A charged track is identified as a kaon if it fulfills the following two requirements:

- The charged track must satisfy the GTL requirements described in Section 4.1.1.
- The charged track must be identified as a Kaon based on the so–called "PidKaonSMSSelector Tight" described in the following Section 4.4.1. [21].

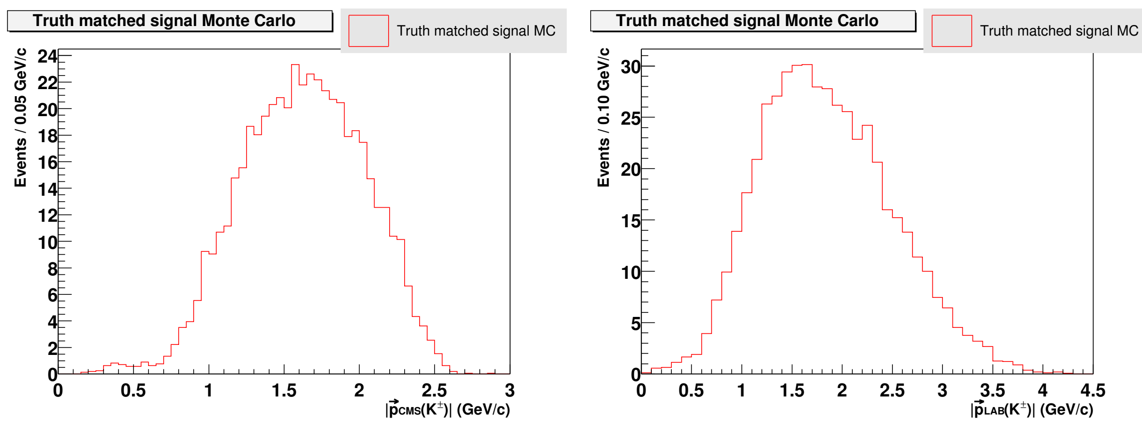

(a) CM frame. (b) Laboratory frame.

Figure 4.5. Kaon momenum in CM and laboratory frame for signal MC. The candidate is truth matched and no cuts are applied in order to gain statistics.

4.4.1 Kaon Particle Identification

One of the outstanding capabilities of the *BaBar* detector is the excellent charged particle identification system and especially the capability of separating charged kaons from charged pions and protons. This excellent separation power of the detector is due to the DIRC (2.3.3).

In the momentum regime above 0.7 GeV/c (in the laboratory frame), only the information from the DIRC is used for the kaon selector chosen ("PidKaonSMSSelector Tight") [22]. This is the momentum regime where most of the signal kaons are (see Figure 4.5 (b)). For the few events in the momentum range of 0.6 GeV/c – 0.7 GeV/c measured in the laboratory frame, information from the SVT and the DCH is also used to identify charged particles. If the laboratory–frame momentum of a charged particle is less than $0.6\,\mathrm{GeV}/c$, only information from the SVT and the DCH is used for kaon identification. This is due to the fact that kaons with such low momentum do not produce Cherenkov light in the quartz bars of the DIRC, their momentum is below Cherenkov threshold according to the formula

$$\left|\vec{p}_{lab}(K^{\pm})\right| > \frac{m(K^{\pm})c}{\sqrt{n^2-1}} \approx 0.46\,\mathrm{GeV}/c, \tag{4.5}$$

where c is the vacuum speed of light, $m(K^{\pm}) \approx 0.494\,\mathrm{GeV}/c^2$ is the mass of the particle (in this case the kaon) and $n = 1.473$ is the refraction index for the quartz bars. Between this threshold for producing Cherenkov light at all and the above stated lower limit of $0.6\,\mathrm{GeV}/c$ is still a gap. This is due to the fact that the number of produced Cherenkov photons is too small to separate them from the background.

The charged particle identification in the SVT and the DCH is based on dE/dx measurements for the track in consideration. Charged particles lose energy when they traverse a medium due to scattering with the electrons and nuclei in the medium. For the charged particle identification in the tracking devices of the *BaBar* detector, a parameterization of the Bethe-Bloch formula is used.

But the overwhelming portion of kaons is identified by the DIRC due to the Cherenkov effect. A specific charged particle produces a specific number of Cherenkov photons in the DIRC depending on the type of the particle, its charge, momentum and position in the DIRC. A lookup table relates the number of expected photons to these parameters. A maximum likelihood fit is performed on the reconstructed emission angle of all measured individual photons. The result of this fit is the measured Cherenkov angle for each track, as well as the number of signal and background photons. Background photons can be suppressed by fitting simultaneously to the photon arrival time [23]. The parameterization for the central value of the Cherenkov

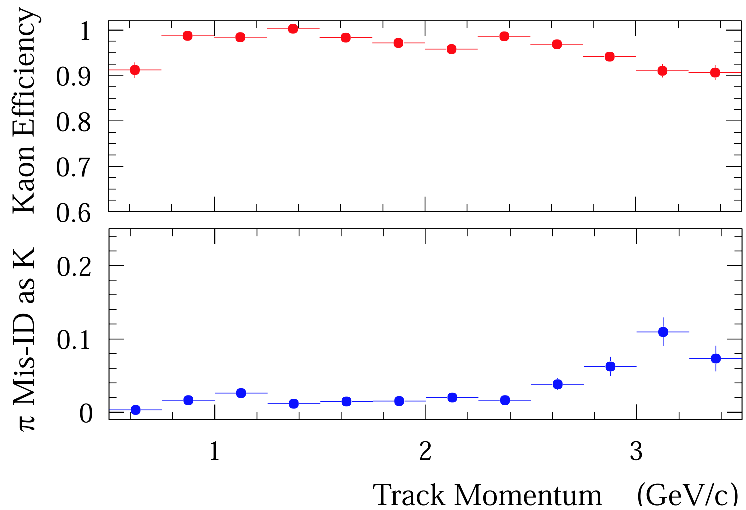

Figure 4.6. Charged kaon selector efficiencies. (Top) charged kaon selector efficiency and (bottom) misidentification probability vs. track momentum determined with a $D^0 \rightarrow K^-\pi^+$ data sample [16].

angle follows Equation (2.4), where the refraction index of the quartz bars is fixed to $n = 1.473$.

The total likelihood for a kaon is based on a normalized product of a gaussian and a poisson probability. The gaussian probability is based on the expected Cherenkov angle, its fitted value and the error on this fit value. The poisson probability is based on the number of expected photons and number of signal and background photons also obtained from the maximum likelihood fit. The performance of this technique can be seen in Figure 4.6.

4.5 $K^{*\pm}$ Selection

In order to obtain the $K^{*\pm}$ candidate, a simple addition of the four-momenta of the kaon and pion is performed. A cut on the invariant mass of this particle combination around the nominal $K^{*\pm}$ mass of $891.66\,\mathrm{MeV}/c^2$ [10] is applied:

- Cut on the $K^\pm\pi^0$ invariant mass: $0.8\,\mathrm{GeV}/c^2 < m_{K^\pm\pi^0} < 1.0\,\mathrm{GeV}/c^2$

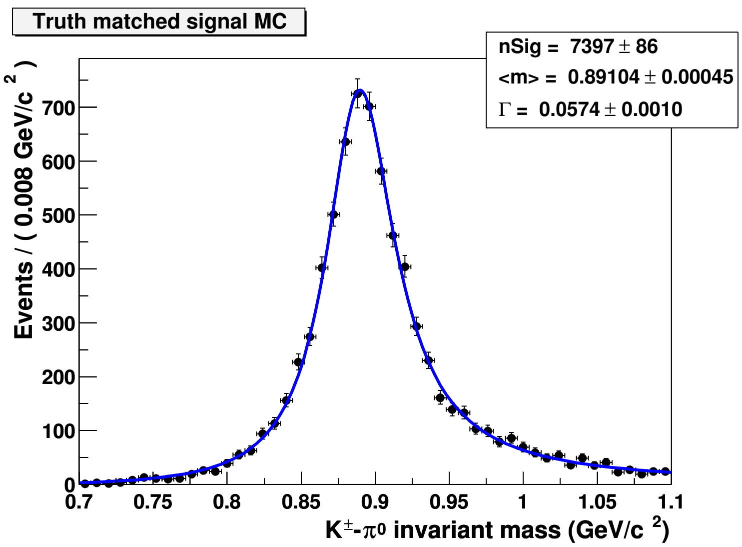

Figure 4.7. $K^{\pm}\pi^0$ invariant mass distribution for signal Monte Carlo. The $K^{*\pm}$ mass peak has been fitted with a relativistic Breit–Wigner function, see Equation (A.5) and the candidate is Monte Carlo truth matched.

4.6 $B^{\pm}$ Selection

The B meson candidate is reconstructed by combining the four momenta of the high–energy photon with the $K^{*\pm}$ candidate. Two independent variables are used.

The first variable is ΔE. This is simply the reconstructed energy of the B candidate shifted by the expected energy of the B meson, both computed in the CM frame. The expected energy of the B meson is simply half of the total CM energy $\sqrt{s}/2$ which is the energy of one of the incoming beams in the CM frame. Thus, the definition of ΔE is

$$\Delta E = E_\gamma + E_{K^{*\pm}} - \frac{\sqrt{s}}{2} \ . \tag{4.6}$$

With this definition, the correctly reconstructed signal events should form a peak centered at zero in ΔE.

The second variable is m^0_{ES} which is usually called “beam energy substituted mass” (or also “beam constrained mass”). In order to compute it, one invokes the relativistic mass–energy–momentum relation, the usual way of calculating the invariant mass from its energy and momentum. But with one important trick: The momentum of the B meson candidate is very small, thus an error on the momentum measurement dues not have so much of an impact as an error on the energy measurement will have. One can now use the knowledge of the initial state instead, namely half of the total available CM energy which is equal to the energy of one of the incoming beams in the CM frame. The beam energies are known to a precision of the order of 1–2 MeV, much better than any energy measurement of a final state particle in the detector. Using this knowledge, the definition of m^0_{ES} becomes

$$m^0_{ES} = \frac{1}{c}\sqrt{\frac{s}{4} - (\vec{p}_{K^{*\pm}} + \vec{p}_\gamma)^2} \ . \tag{4.7}$$

An additional improvement of this variable can be made by assuming that the m^0_{ES} resolution is dominated by the energy resolution of the high–energy photon. The impact of the limited resolution can be reduced by rescaling the four momentum of the photon in such a way as to satisfy $\Delta E = 0$ for the B candidate

$$p'_\gamma = \frac{\frac{\sqrt{s}}{2} - E_{K^{*\pm}}}{E_\gamma} \cdot p_\gamma \ , \tag{4.8}$$

and by using this momentum for the computation of a rescaled energy–substituted mass

$$m_{ES} = \frac{1}{c}\sqrt{\frac{s}{4} - \left(\vec{p}_{K^{*\pm}} + \vec{p}'_\gamma\right)^2} \ . \tag{4.9}$$

The improvement in the energy resolution can be seen by comparing the truth matched signal Monte Carlo peak in m^0_{ES} with the peak in m_{ES} (see Figure 4.8).

The analysis makes use of a fit region and a signal region, defined as:

- Fit region: $(-0.3\,\mathrm{GeV} < \Delta E < 0.3\,\mathrm{GeV}) \times (5.2\,\mathrm{GeV}/c^2 < m_{ES} < 5.29\,\mathrm{GeV}/c^2)$
- Signal region: $(-0.2\,\mathrm{GeV} < \Delta E < 0.1\,\mathrm{GeV}) \times (5.27\,\mathrm{GeV}/c^2 < m_{ES} < 5.29\,\mathrm{GeV}/c^2)$

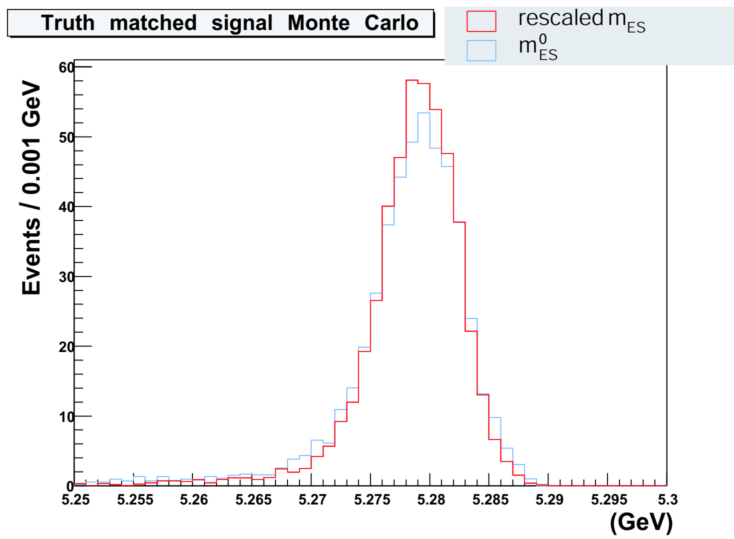

Figure 4.8. Comparison of the resolution of m^0_{ES} with m_{ES}. Only truth matched signal Monte Carlo candidates have been selected and no cuts have been applied in order to gain statistics.

A scatter plot together with the corresponding projections is shown for a wider ΔE range in Figure 4.9.

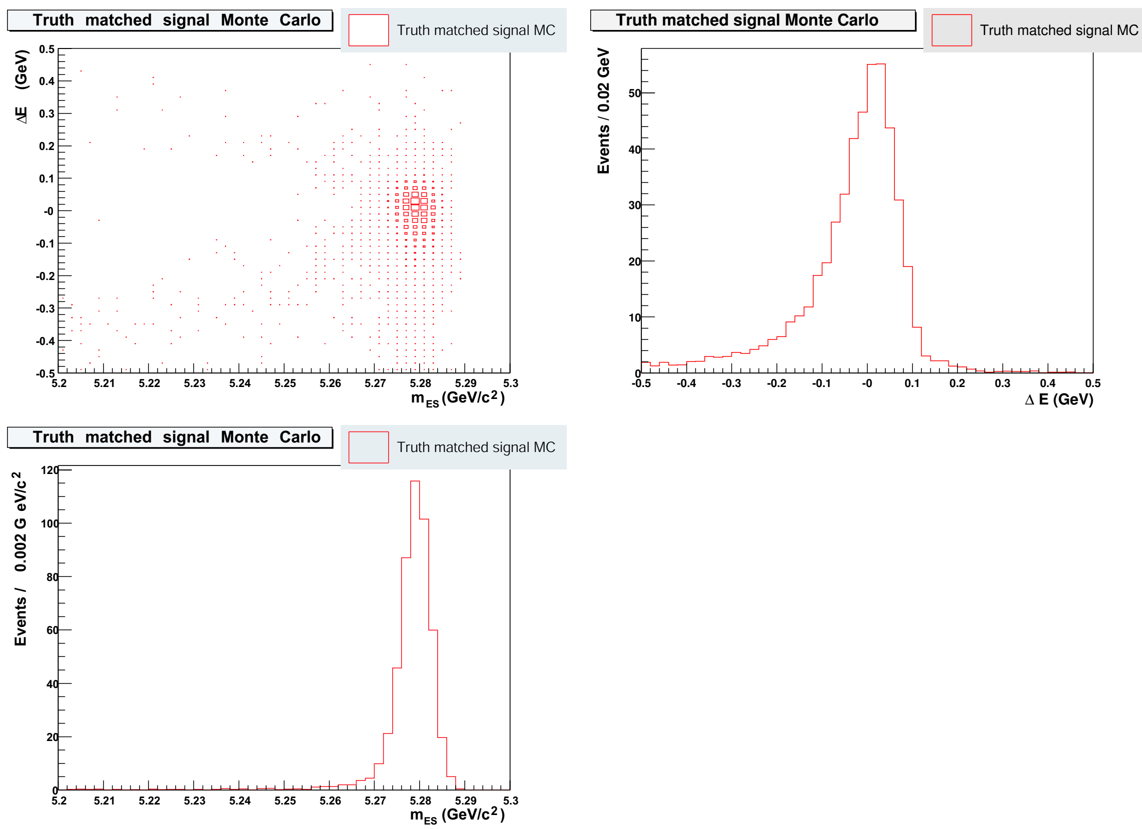

Figure 4.9. Scatter plot of ΔE vs. m_{ES} for truth matched signal Monte Carlo. No cuts have been applied in order to gain statistics.

CHAPTER 5

BACKGROUND SUPPRESSION WITH A NEURAL NETWORK

5.1 Introduction to Neural Networks

A neural network–based analysis has an intrinsic advantage over an analysis based on a series of cuts on individual variables. The neural network is able to consider correlations between variables and thus find a better separation between signal and background. One can, for example, consider the task of separating sample A (e.g. signal events) from sample B (e.g. background events) in the variable X_1 (see Figure 5.1(a)) and the same separation of A and B in X_2. A simple cut on both variables X_1 and X_2 would not be an optimal separation of A and B. A neural net can find a better separation by considering the correlation between X_1 and X_2 (see Figure 5.1(b)).

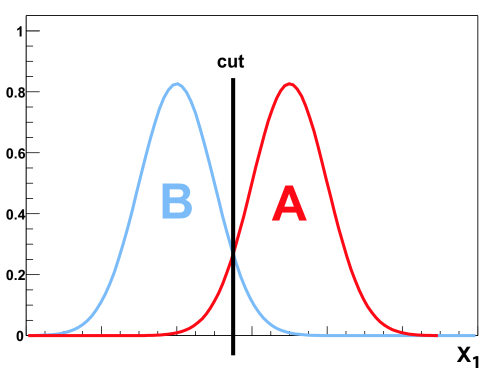

(a) Separation of two samples A and B in X_1.

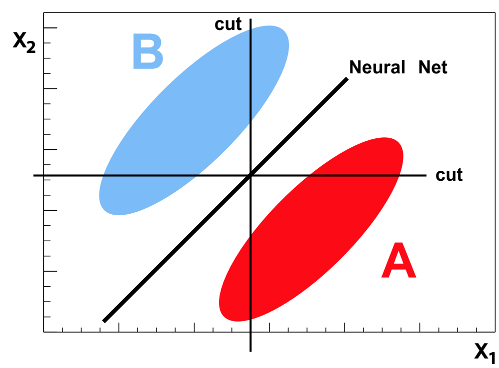

(b) Two dimensional plot of variable X_1 and X_2.

Figure 5.1. A one dimensional cut. (a) Separation of two samples in the variable X_1. (b) Separation of these two samples in two variables with two individual cuts and with a neural network.

One can also imagine more complicated correlations between two variables, for example something like the situation shown in Figure 5.2. The neural network is in principle able to use the complicated correlation between the different variables (here only X_1 and X_2 for simplicity) in order to find the best achievable separation between signal (A) and background (B).

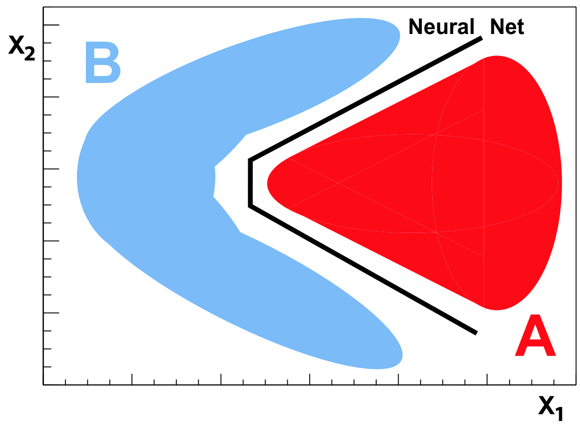

Figure 5.2. A two dimensional cut compared to a neural network. A more complicated correlation between X_1 and X_2. A neural net is in principle able to find a good separation between A and B.

A cut can be understood as a step function $\Theta(X - X')$, where events are kept if $\Theta(X - X') = 1$ and rejected if $\Theta(X - X') = 0$. The separation found by a neural net in Figure 5.1(b) can be thus written as $\Theta(aX_1 + bX_2 + c)$ and the complicated shape in Figure 5.2 can be understood as a combination of step functions

$$\Theta\left(\Theta\left(a_1X_1 + b_1X_2 + c_1\right) + \Theta\left(a_2X_1 + b_2X_2 + c_2\right) + \Theta\left(a_2X_1 + b_2X_2 + c_2\right) - 2\right) \ . \tag{5.1}$$

This combination of step functions takes on the value 0 in region B and 1 in region A, thus it can be identified with the desired discrimination.

A neural net for the above example can be visualized as seen in Figure 5.3. The values of two inputs X_1 and X_2 are combined at three hidden nodes Y_j, altered by

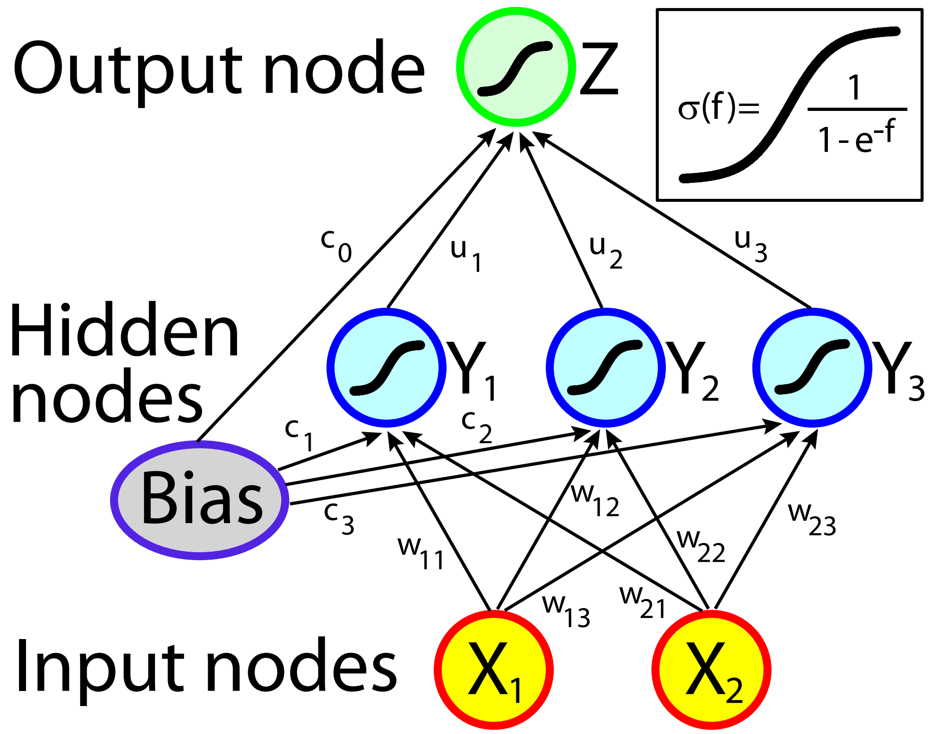

Figure 5.3. Neural network visualization.

weights w_{ij} and biases c_j (with $i = 1, 2$ and $j = 1, 2, 3$). The inputs y_j to these hidden nodes Y_j are computed as $y_j = \sum_i w_{ij} x_i + c_j$. This is equivalent to the argument of the step functions in example above. But the step function is replaced in a neural net with a function whose first derivative is smooth, in this case the function is the sigmoid function $\sigma(y_j) = 1/(1 + e^{-y_j})$. This so–called transfer function needs to have a smooth first derivative due to the training procedure of the neural net (see Section 5.2). Also, in case of overlap regions of signal and background events, the smooth $\sigma(y_j)$ transfer function allows the neural net to assign a signal probability to each event rather than classify it absolutely like it would be done if a step function is used as the transfer function.

The outputs of the hidden nodes $g_j = \sigma(y_j)$ are then again combined with weights u_j and a single bias c_0 to the input $z = \sum_j u_j g_j + c_0$ of the last node, the output node Z. The final output of the neural net is $NN_{out} = \sigma(z)$. The complete neural net can be described in the mathematical formula

$$NN_{out} = \sigma\left(\sum_j u_j \left[\sigma\left(\sum_i w_{ij}x_i + c_j\right)\right] + c_0\right) \ . \tag{5.2}$$

For the interested reader, [24] is a good source of information about neural networks.

5.2 Neural Network Training

The important task is now to determine the optimal combination of weights w_{ij} and u_j and biases c_j and c_0. In order to measure the performance of a given neural net, an analog to the "χ^2" for histogram fitting is used, the "sum–squared error" (SSE) is defined as:

$$SSE\left(w_{ij}, u_j\right) = \sum_{a=1}^{N} \left[NN_{out}\left(\vec{x}_a; w_{ij}, u_j\right) - F\left(\vec{x}_a\right)\right]^2 \ , \tag{5.3}$$

where $\vec{x}_a$ is the vector of input variables for the ath event, $NN_{out}\left(\vec{x}_a; w_{ij}, u_j\right)$ is the previously defined neural net output with the weights as parameters and $F\left(\vec{x}_a\right)$ is the desired output, e.g. 0 if the input was a background event and 1 if the input was a signal event. The SSE can be minimized in the same way as the minimization for a χ^2 fit, via gradient descent. First, the derivative of the SSE is computed relative to changes in the weights u_j, these weight coefficients are altered such that the SSE is minimized. Since the desired output of the hidden nodes is not known, the next step in the optimization is to compute the new weights u_j. With these new weights, the desired output for the hidden nodes can be computed and then, the weights from the input nodes to the hidden notes w_{ij} can be optimized in a similar way. Now, the SSE of the hidden node needs to be computed and differentiated with respect to the weights w_{ij}. Then, the changes for these weights can be computed. This procedure is called "backpropagation", for obvious reasons.

The derivative of the SSE is needed in this procedure. Thus, the derivative of the transfer function is also needed and the step function cannot be used as a transfer function for this optimization procedure.

For the training of the neural net for this analysis, the input consists of truth matched signal Monte Carlo (from the generic $B^{\pm} \rightarrow K^{*\pm}\gamma$ Monte Carlo sample) and the same number of continuum background events. For both samples, only events within the fit region are selected and also all the cuts explained in Chapter 4 are applied. The continuum background sample consist of three parts, uds, $c\bar{c}$ and $\tau^{+}\tau^{-}$ events. Events from these subsamples are chosen in that number that they correspond to the same integrated luminosity. The desired neural net output for a signal event is 1 and for a continuum background event it is 0. Both samples are divided into two parts of equal size, one part is used for training the neural net and the second is used for validation. The validation with a different data sample is required in order to ensure that the neural net is not overtrained. Overtraining occurs when the neural net learns statistical fluctuations in the training sample.

The performance of the neural net is quantified by the "mean squared error" (MSE):

$$MSE = \frac{SSE}{Number\ of\ events}\ . \tag{5.4}$$

It is computed after each cycle for both the training and validation sample. If the neural net overtrains, the MSE for the validation sample does not decrease any more while the MSE for the training sample keeps decreasing after each cycle. The neural network is optimized at the minimum of the MSE for the validation sample.

5.3 Neural Network Algorithm

The "Stuttgart Neural Network Simulator" (SNNS) [25] is the neural network implementation used for this analysis. A ROOT interface called RooSNNS has been developed for setting up the network and training it. Also, it makes it possible to use conveniently the ROOT files which contain the data as input for the neural network.

5.4 Input Variables to the Neural Network

The neural network used for this analysis relies on the following 23 input variables which are:

- The cosine of the helicity angle $\cos(\theta_H)$ of the $K^{*\pm}$ described in Section 5.4.1.
- $\cos(\theta_B)$ described in Section 5.4.2.
- The event shape variable $\cos(\theta_T)$ described in Section 5.4.3.1.
- 18 energy cones described in Section 5.4.3.2.
- R_2' described in Section 5.4.4.
- The net flavor of the event described in Section 5.4.5.

All these variables have discrimination power, which means that their shape is different for signal and continuum background events.

5.4.1 Helicity Angle of the $K^{*\pm}$

The helicity angle θ_H of the $K^{*\pm}$ meson is the angle between the momentum vector of the $K^{\pm}$ and the momentum vector of the $B^{\pm}$ meson, computed in the rest frame of the $K^{*\pm}$. The θ_H distribution for a signal event is expected to follow a $\sin^2(\theta_H)$ function. This is due to conservation of helicity in the ultra–relativistic limit and the nature of the decay: A vector meson decaying into two scalar mesons.

The signal and background shapes of this variable can be seen in Figure 5.4.

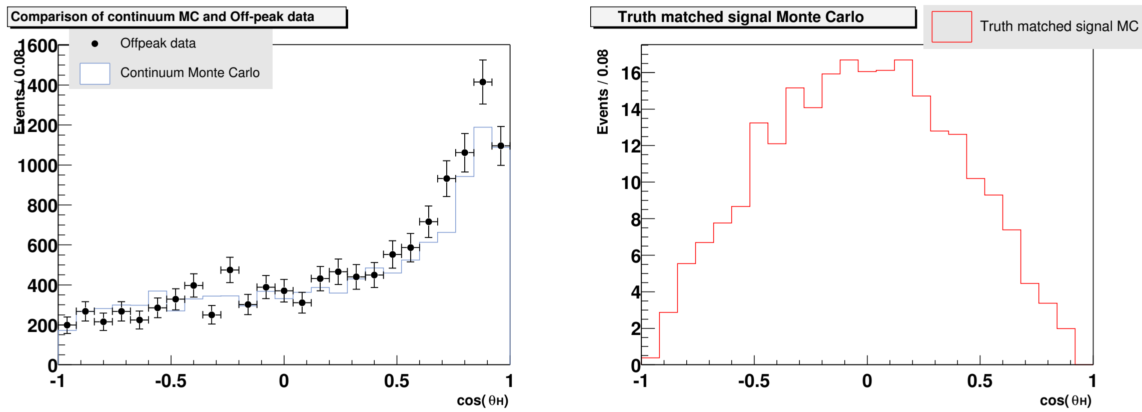

(a) Continuum background.

(b) Signal Monte Carlo.

Figure 5.4. Helicity distribution. Distributions of $\cos(\theta_H)$ for (a) continuum background from offpeak data (points) and Monte Carlo (histogram) and (b) truth matched signal Monte Carlo. All cuts but the neural net cut are applied.

5.4.2 $\cos(\theta_B)$

The variable θ_B is the angle between the momentum vector of the B meson candidate and the beam direction computed in the CM frame. This is basically the helicity angle for the $\Upsilon(4S)$ meson. Since the $\Upsilon(4S)$ is also a vector meson and the two B mesons are scalars, the expected distribution of θ_B is also a $\sin^2(\theta_B)$ distribution, just like in the case of the helicity angle of the $K^{*\pm}$ (see Section 5.4.1). The expected signal distribution of $\cos(\theta_B)$ is shown in Figure 5.5 (b). Since there is no true B meson candidate in a continuum event, the distribution of $\cos(\theta_B)$ is expected to be flat, as can be seen in Figure 5.5 (a).

5.4.3 Event Shape Variables

5.4.3.1 $\cos(\theta_T)$

The thrust angle θ_T is the angle between the high-energy photon and the thrust axis of the rest of the event computed in the CM frame. The thrust axis of the event $\hat{T}$ is defined as the axis which maximizes the sum of the particle momenta alon this axis. The thrust T is related to this axis by

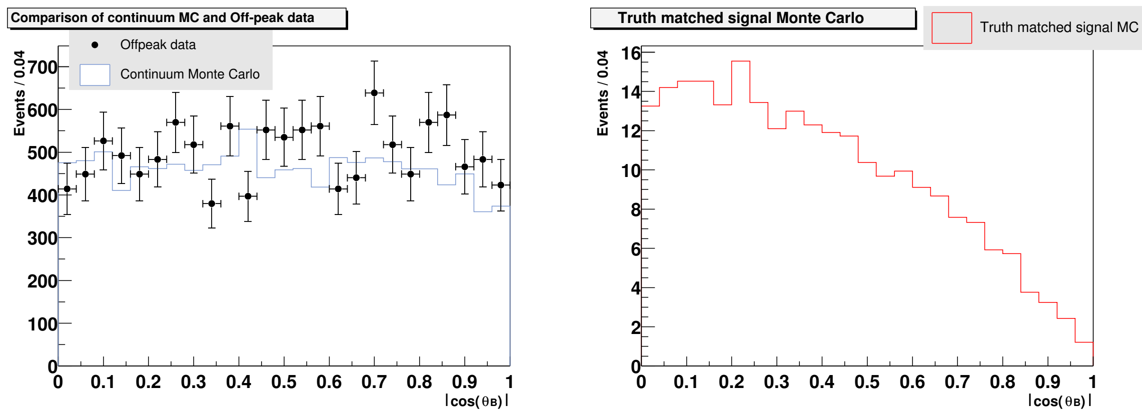

(a) Continuum background. (b) Signal Monte Carlo.

Figure 5.5. $\cos(\theta_B)$ distribution. The shape for continuum background Monte Carlo (blue) and overlaid offpeak data (black circles) is shown in Figure (a). The same distribution for truth matched signal Monte Carlo is shown in red in Figure (b). All cuts but the neural net cut are applied.

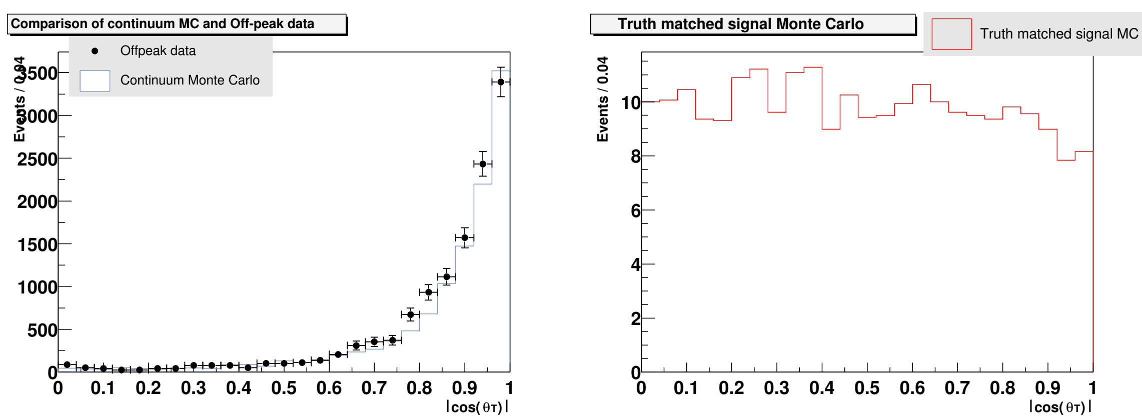

(a) Continuum background. (b) Signal Monte Carlo.

Figure 5.6. $\cos(\theta_T)$ distribution. The shape for continuum background Monte Carlo (blue) and overlaid offpeak data (black circles) is shown in Figure (a). The same distribution for truth matched signal Monte Carlo is shown in red in Figure (b). All cuts but the neural net cut are applied.

$$T = \frac{\sum_i \left| \hat{T} \cdot \vec{p}_i \right|}{\sum_i |\vec{p}_i|} \ , \tag{5.5}$$

where $0.5 < T < 1.0$. T close to 1 corresponds to a jet like event and T close to 0.5 corresponds to an isotropic B meson event. The daughters of the signal B meson ($K^{*\pm}$ and π^0) are excluded for the determination of the thrust axis, but all other neutral and charged candidates in the event are used.

Due to the small 3-momentum of the B meson, signal events are very isotropic. Thus, the momentum direction of the high energy photon is uncorrelated with the daughters of the other B meson. The distribution of $|\cos(\theta_T)|$ is thus expected to be flat as can be seen in Figure 5.6 (b). This is not the case for continuum background events. As mentioned before, a continuum background event is mostly a pair of two back–to–back jets. The high–energy photon originates usually from a high energy π^0 or η decaying in one of these jets. Thus, the momentum direction of the high energy photon is almost identical with the direction of one of the jets. For continuum background events, θ_T is thus expected to be close to 0° or 180°. The absolute value of $\cos(\theta_T)$ is thus expected to peak around 1 for a continuum background event, as can be seen in Figure 5.6 (a).

5.4.3.2 18 Energy Cones

The energy cones provide additional means to distinguish spherical B meson events from jet–like continuum background events. The CM frame momentum of each track and photon not associated with the signal B meson is compared to the CM frame momentum of the high–energy photon. The angle between each of these momentum vectors and the momentum vector of the high–energy photon is computed and associated with one of 18 angular bins ranging from parallel to antiparallel with the CM frame momentum of the high–energy photon (see Figure 5.7). The energy of all tracks and photons in each of these angular bins is summed up. Thus, one obtains 18

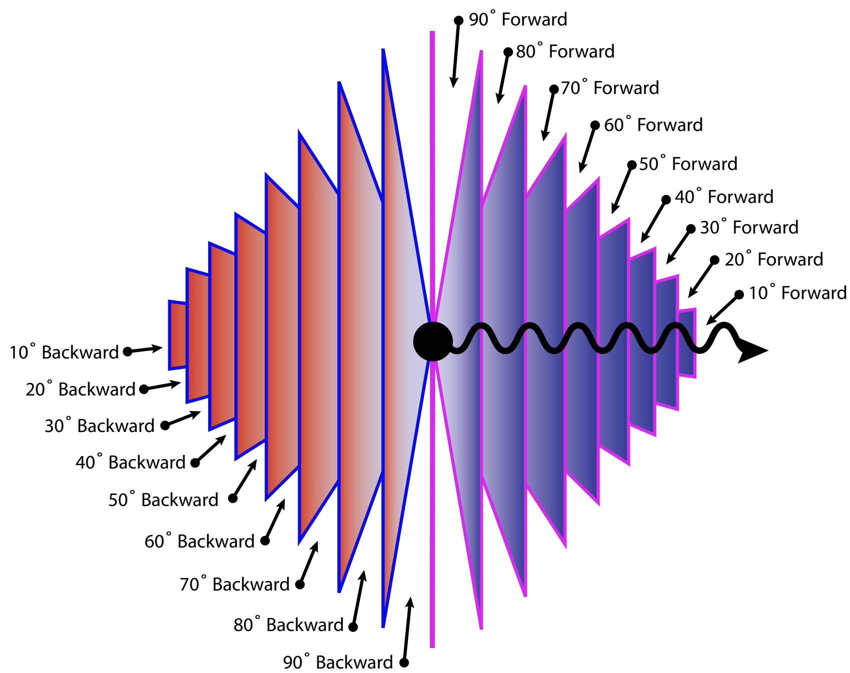

Figure 5.7. Energy cones. They are ordered around the momentum of the high energy photon in the CM frame. The energy in each cone is the sum of the energies of tracks and photons whose momenta point into the specific cone.

variables characterizing the energy distribution in the event with respect to the CM frame momentum of the high–energy photon.

As mentioned before, the high energy photon is in a continuum background event expected to be within one of two back–to–back particle jets. Thus, for a continuum background event, most of the energy of the event is expected to be within the cones parallel and antiparallel to the photon momentum in the CM frame (see Figure 5.8). This is not the case in a B meson event. Since a B meson event is more spherically symmetric, the energy is expected to be more evenly distributed in all the energy cones (see Figure 5.9).

5.4.4 R_2'

The R_2' variable is similar to R_2 and it is computed in almost the same way. The only difference is that it is not computed in the CM frame as R_2 is. Rather, the

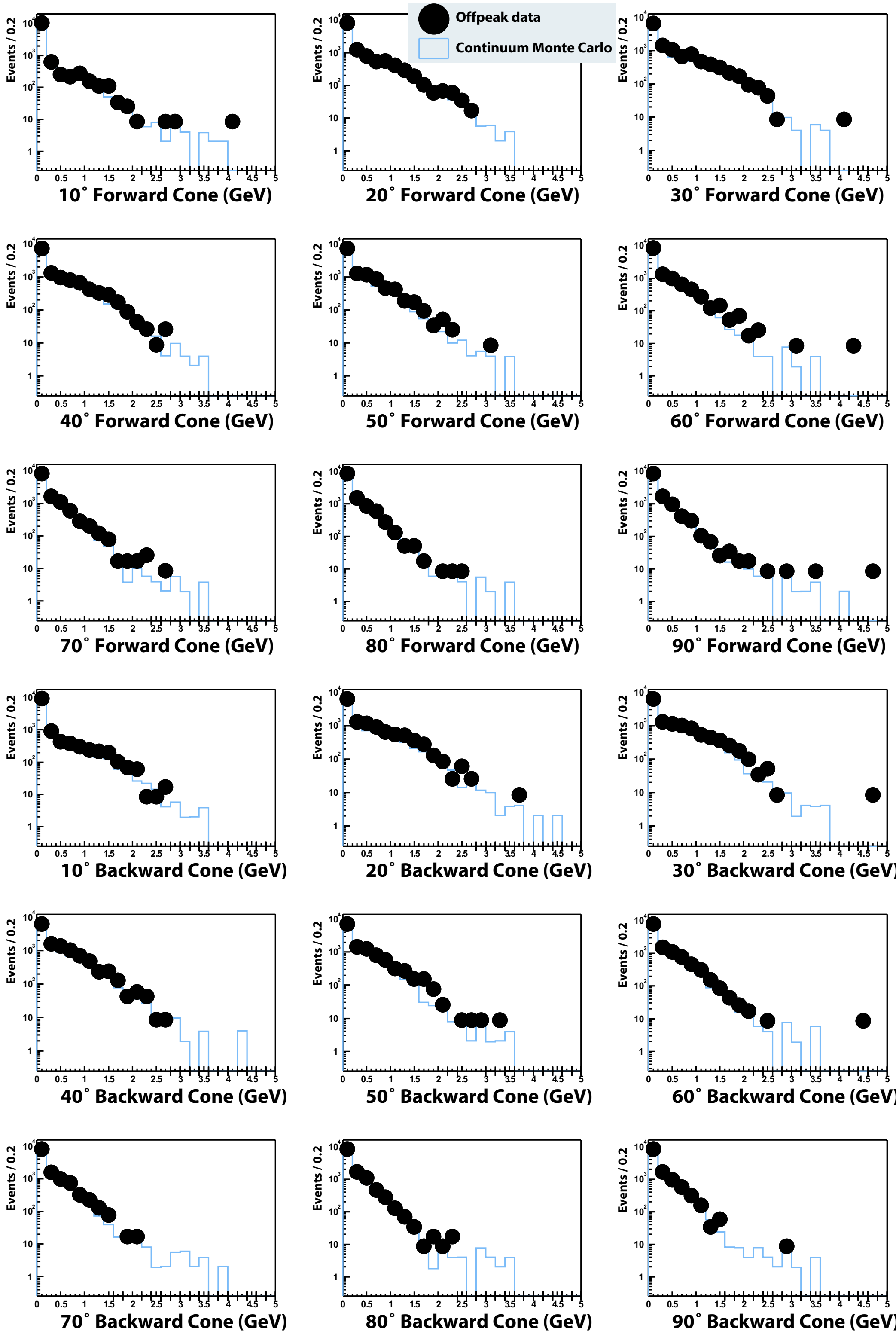

Figure 5.8. Continuum background energy cones. The continuum background Monte Carlo (blue) overlaid with offpeak data (black). All cuts but the neural net cut are applied.

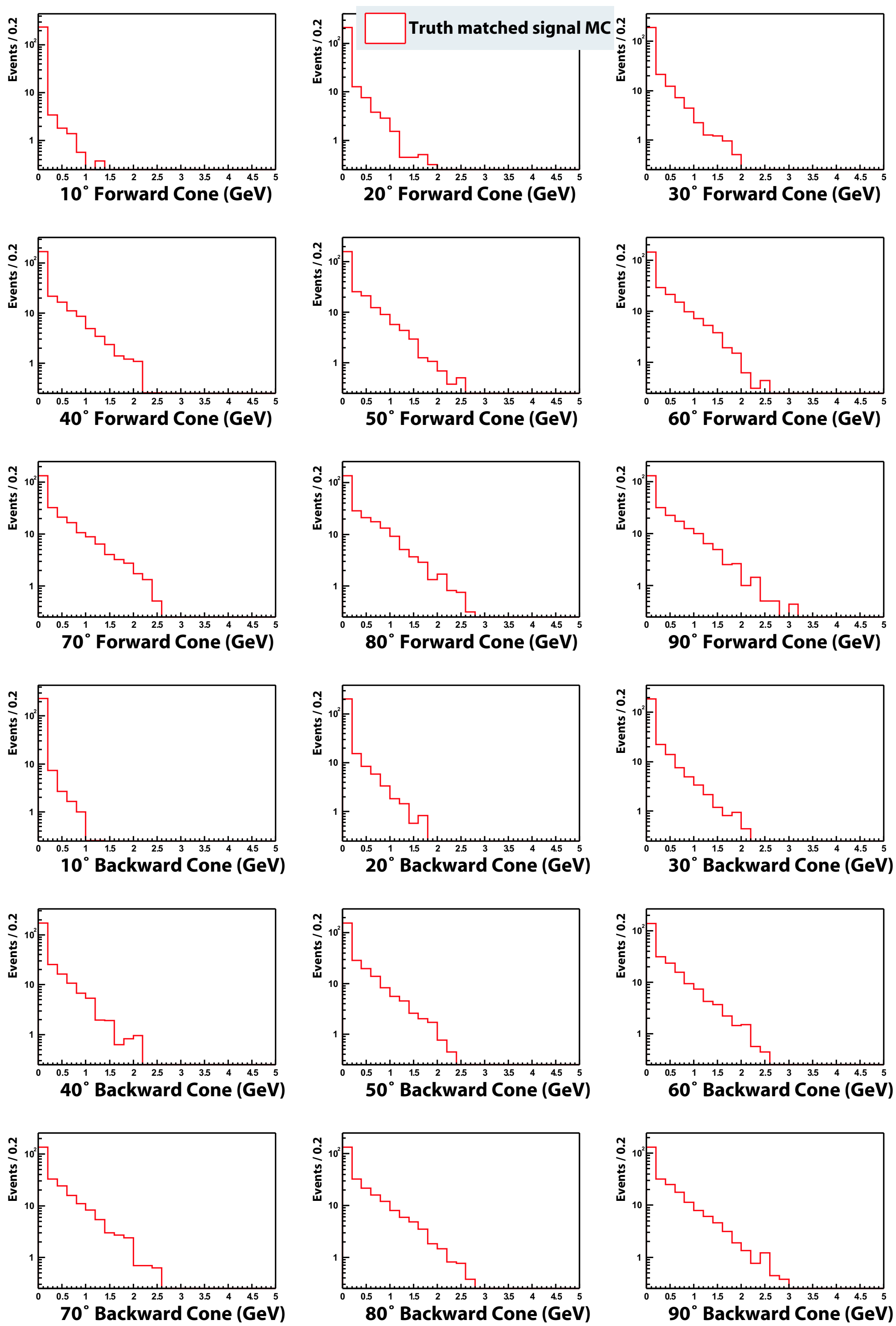

Figure 5.9. Signal energy cones. The truth matched signal Monte Carlo candidates have been selected only (red). All cuts but the neural net cut are applied.

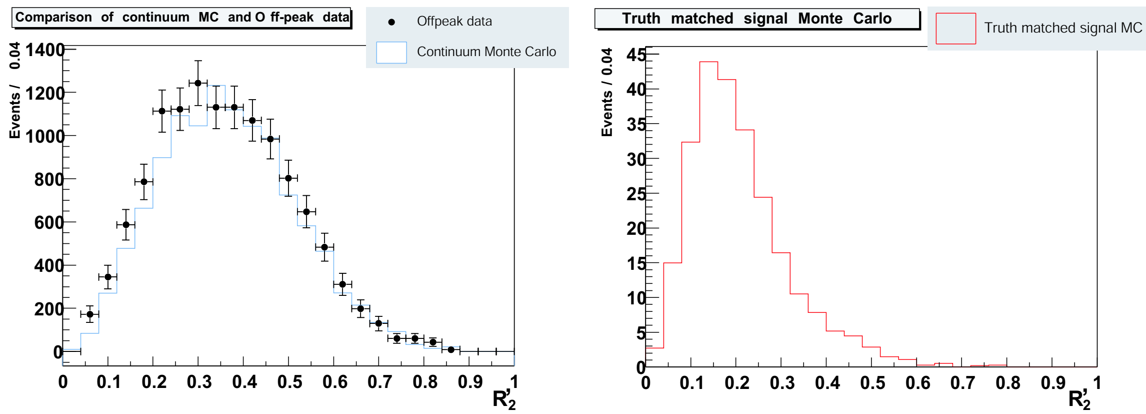

(a) Continuum background. (b) Signal Monte Carlo.

Figure 5.10. Distribution of R_2'. The shape for continuum background Monte Carlo (blue) and overlaid offpeak data (black circles) is shown in (a). The same distribution for truth matched signal Monte Carlo is shown in red (b). All cuts but the neural net cut are applied.

high–energy photon is removed from the event and the rest frame of the remaining particles is used for computing R_2'. The idea of "removing" the high–energy photon from the event is to be sensitive to ISR events. By going to the rest frame of the high energy photon coming from ISR, one recovers two back–to–back final state particle jets in the event. The signal and background shapes of this variable can be seen in Figure 5.10.

5.4.5 Net Flavor of the other B

The net flavor variable looks at the rest of the event which are all particles but the kaon, pion and high–energy photon considered as the signal B meson decay products. If a specific event is an event containing a signal decay, the particles in the rest of the event are decay products of the other B meson in the event. The idea of the net flavor variable is to look at properties of this other B meson candidate in the event. Due to the flavor changing weak B meson decay, the decay products of the B meson can contain the following:

- An unpaired charged kaon,

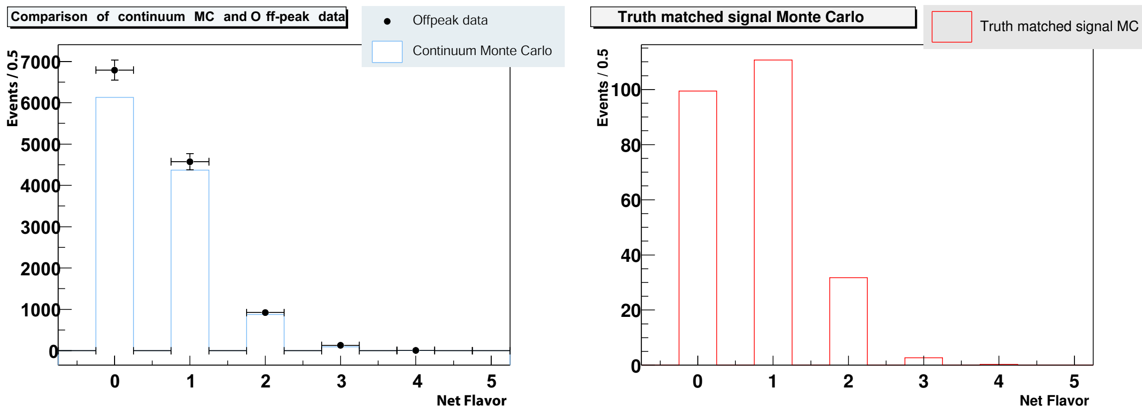

(a) Continuum background. (b) Signal Monte Carlo.

Figure 5.11. Flavor variable. This variable is shown for continuum background Monte Carlo (blue) and overlaid offpeak data (black circles) is shown in (a). The same distribution for truth matched signal Monte Carlo is shown in red (b). All cuts but the neural net cut are applied.

- an unpaired electron (or positron),
- an unpaired muon,
- an unpaired slow charged pion,
- several K_S^0.

An unpaired charged kaon can be produced due to a weakly decaying B or D meson. An $e^+e^- \to s\bar{s}$ event produces a charged kaon pair (positive and negative), but not a single unpaired charged kaon. A single unpaired kaon can occur if a pair of charged kaons was produced in the first place but one of them decayed inside the detector (i.e. before it reaches the DIRC). The remaining kaon is then a single unpaired kaon.

A similar situation is given for the single unpaired electron or muon. Both the B mesons and the D mesons can undergo a semileptonic decay where a single unpaired electron or muon is produced together with a (not observed) neutrino. This is not likely to occur in a light quark event. The events of the type $e^+e^- \to l^+l^-$ produces a charged lepton pair, but not a single unpaired charged lepton. Another source of a charged lepton pair is pair production. A possible source of a single unpaired muon in an $e^+e^- \to s\bar{s}$ event is a decay of a charged kaon inside the detector ($c\tau(K^\pm) = 3.713\,\text{m}$ [10]). A single unpaired muon and a muon–type neutrino are in 63.43 % of those decays the decay products.

A unpaired slow charged pion can be produced in the decay chain $B^- \to D^{*+}X$, $D^{*+} \to D^0\pi^+$.

Another source of unpaired charged particles of the categories considered above is loosing one of those particles (originally produced in a pair) in the detector, e.g. if its momentum is along the beam pipe.

The knowledge of the above differences between B meson decays and non–B meson decays can be utilized for separating the signal from the background. A new variable is computed with the following quantities:

1. The net kaon number is defined as: N_K = Number of K^+− Number of K^-. The kaon must be identified with the "PidKaonSMSSelector Tight" described in Section 4.4.1.

2. The net electron number is defined as: N_e = Number of e^+− Number of e^-. The electron must be identified with a selector similar to the "PidKaonSMSSelector Tight", but tailored for electrons. In addition, $|\vec{p}_{CMS}(e)| > 0.5\,\text{GeV}/c$ is required.

3. The net muon number is defined as: N_μ = Number of μ^+− Number of μ^-. The muon must be identified with a selector similar to the "PidKaonSMSSelector Tight", but tailored for muons. In addition, $|\vec{p}_{CMS}(\mu)| > 1.0\,\text{GeV}/c$ is required.

4. The net slow charged pion number is defined as: $N_{(slow\ \pi^\pm)}$ = Number of slow π^+− Number of slow π^-. Here, slow means that $|\vec{p}_{CMS}(\pi)| < 0.250\,\text{GeV}/c$ is required. For the angle between the pion momentum and the thrust axis of the event, $\cos(\theta_{Thrust,|\vec{p}_{CMS}(\pi)|}) > 0.8$ is required. Also, distance of closest approach

to the beam axis is required to be $d_0 < 0.5\,\text{cm}$. In the z direction (the direction of the electron beam), the track must be within $-2\,\text{cm} < z_0 < 0.8\,\text{cm}$.

5. The number of K_s^0 is simply: $N_{K_s^0}$ = Number of K_s^0. The K_s^0 candidate must be successfully vertexed (via its decay products $\pi^+\pi^-$) and its mass must fulfill the requirement $0.480\,\text{GeV}/c^2 < m_{\pi^+\pi^-} < 0.516\,\text{GeV}/c^2$. Also, the angle $\theta_{[Disp,|\vec{p}_{CMS}(K_s^0)|]}$ between the CM frame momentum of the K_s^0 and the vector connecting the beam spot with the K_s^0 vertex is computed and the requirement $\left|cos(\theta_{[Disp,|\vec{p}_{CMS}(K_s^0)|]}\right| > 0.98$ needs to be fulfilled. Furthermore, the K_s^0vertex needs to be at least 1 mm displaced from the beam spot. (The beam spot is the primary vertex of charged tracks averaged ever a number of runs.)

These categories are exclusive and hierarchical, meaning the following: If a track is identified as a kaon, it will contribute to the first category and to no other. For the electron identification, only the remaining tracks are considered. Of course, all tracks associated with the signal $B^\pm \to K^{*\pm}\gamma$ are excluded from this computation. The combined net flavor is then defined as:

$$N_{\mathcal{F}} = |N_K| + |N_e| + |N_\mu| + \left|N_{(slow\ \pi^\pm)}\right| + N_{K_s^0}\ . \tag{5.6}$$

Continuum background and signal distributions of $N_{\mathcal{F}}$ can be seen in Figure 5.11.

5.5 Neural Network Performance

The neural network has been setup with 200 hidden nodes in one layer and one output node. The desired neural network output is 1 for a signal event and 0 for a continuum background event. The neural network was trained for 900 cycles with "BackpropChunk" as training function. The difference between this training function and "Backprop" (see Section 5.2) is that the weights are not altered after each event, but after a chunk of 20 events. The development of the MSE during the training can be seen in Figure 5.12 (a) for both training and validation samples. The performance of the neural net is shown in Figure 5.12 (b). This plot shows the fraction of the continuum background that is rejected vs. the fraction of the signal that is kept, for both the training and validation samples. The cross in this plot indicates the performance of a series of usual cuts on the three angles $\cos(\theta_{H,B,T})$. Since the neural network can keep with the same background rejection efficiency more signal events, it performs better than the series of simple cuts do. That both training and validation samples show the same performance is an indication that the neural network was not overtrained. This can also be seen by comparing the output for the two samples and noting that they are the same within errors (see Figure 5.12 (c) and (d)). A comparison of the neural network output for continuum background Monte Carlo with offpeak data can be seen in Figure 5.12 (e). The offpeak data agrees well with the continuum Monte Carlo. A cut optimization of the neural network output has been done with the goal of maximizing the significance $S/\sqrt{S+B}$, where S is the number of signal events and B is the number of background events, in the signal region. The plot of the significance vs. cut value on the neural network output can be seen in Figure 5.12 (f).

The most powerful input to the neural network is $\cos(\theta_T)$. This can already be seen by noting the big shape difference of the continuum background and signal distributions of this variable (see Figure 5.6). The inclusion of the 18 energy cones and especially the net flavor variable in the neural network results only in a slight improvement of the continuum background suppression. This can also be noted by realizing that these variables are not very different for continuum background and signal events as can be seen in Figure 5.8, Figure 5.9 and Figure 5.11.

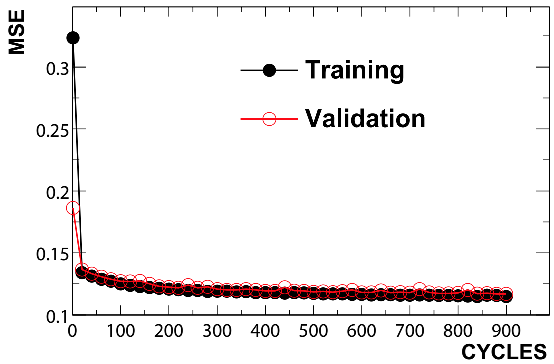

(a) MSE learning curve.

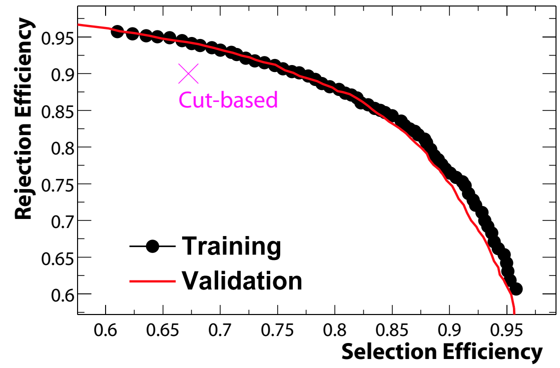

(b) Selection– vs. rejection efficiency.

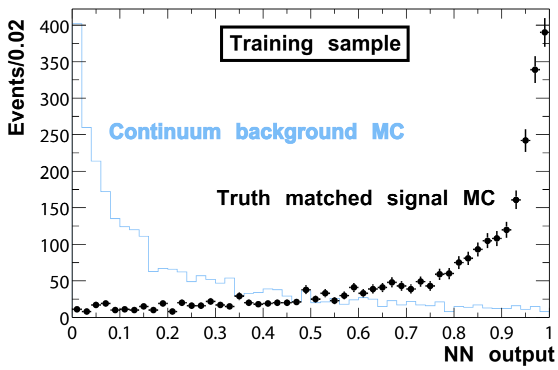

(c) NN training output.

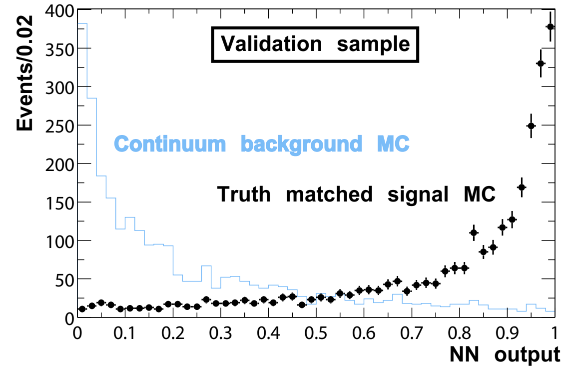

(d) NN validation output.

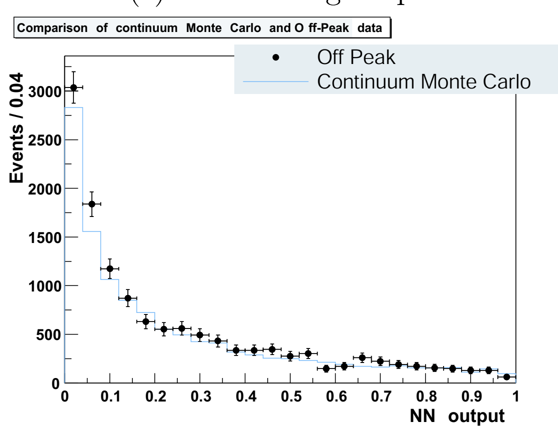

(e) NN background output comparison.

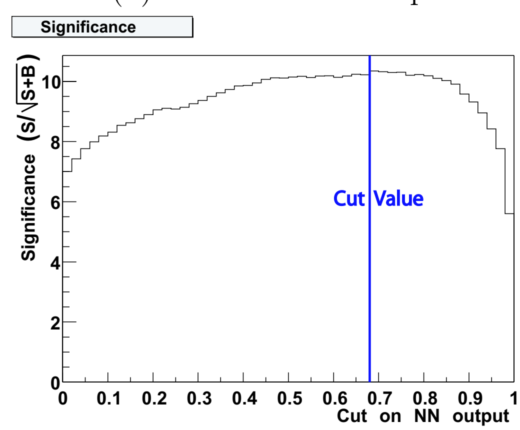

(f) NN cut optimization.

Figure 5.12. Neural network training and validation. The learning curve (MSE vs. cycles) is shown in (a), both for the training and validation samples. The efficiency curve for training and validation samples is shown in (b), the cross marks the achieved efficiency for optimized single cuts on the three $\cos(\theta_{H,B,T})$ variables. The NN output is shown for the training– (c) and validation–sample (d), where the red is the continuum Monte Carlo and the black is signal Monte Carlo. A comparison of the NN output is shown in (e) for continuum Monte Carlo and offpeak data. The significance curve for the cut optimization is shown in (f), the cut value is indicated by the vertical line.

CHAPTER 6

EXPECTED YIELDS

6.1 Best $B^{\pm}$ Candidate Selection

Since there are multiple B meson candidates in each event, the best candidate per event needs to be selected. The total CM energy of a good B meson candidate should be close to half of the total CM energy available. Thus, for a good B meson candidate, ΔE is close to zero. After all the analysis cuts are applied, the B meson candidates remaining in the fit region are considered. Of those B meson candidates, the one with the smallest absolute value of ΔE is selected. This selection removes about 3.5% of the truth matched signal events as can be seen in Table 6.1.

6.2 Signal Yield

The effects of all the cuts on the number of truth matched signal events can be seen in Table 6.1. The cut which removes most of the truth matched signal is the first one in this table. This cut actually consists of several parts from which the finding of a B candidate in the event is reducing the number of events the most. This is due to the limited solid angle coverage of the detector. Since four particles need to be found in the event, the probability of having one of them outside the detector coverage is high.

The most important number in this table is 18.9% for the cumulative overall efficiency (with truth match released). All signal events will be classified as signal, even if the event is not correctly reconstructed, e.g. the true signal pion can be lost and a pion originating from the other B meson can be used to form the signal B meson candidate. If the truth match is required, the signal efficiency drops to 16.5%. The misreconstructed signal events account for the efficiency difference between truth matched event and event without a required truth match.

6.3 B Meson Background Distributions

As mentioned before, by far the largest background contribution comes from continuum events. Nevertheless, there is some non negligible background due to a real B meson decaying into a non signal mode. This B meson background can be classified in three categories:

- The "crossfeed" background category consists of events with a real $B \rightarrow K^*\gamma$ decay (charged or neutral), but not from signal $K^{*\pm} \rightarrow K^\pm\pi^0$ decays. One of the other $B \rightarrow K^*\gamma$ decay modes can occur but due to picking one of the particles needed for forming a signal candidate from the other B meson in the event, this event gets identified as a signal event. For example a $K^{*0} \rightarrow K^+\pi^-$ decay from a neutral B meson can occur, and the correct high energy photon and kaon has been used to reconstruct the B meson, but the charged pion gets swapped for a neutral pion from the other B meson in the event. As a result, such an event gets identified as a signal event.

- The "downfeed" background is a real $b \rightarrow s\gamma$ transition which does not hadronize as a $B \rightarrow K^*\gamma$ decay, but as a higher–mass K^* resonance and possibly higher particle multiplicities in the final state. These higher multiplicity final states can contain the same final state particles as a signal event (high energy photon, charged kaon and neutral pion) and in addition one or more pions. Since these additional pions carry away only a small portion of the total energy, the event can still be reconstructed as a signal event. This missing energy will show up in a broad ΔE peak shifted to negative values.

Section	Cut	Passed	Rel. ϵ (%)	Cum. ϵ (%)
	$B^+ \rightarrow K^{*+}\gamma(K^{*+} \rightarrow K^+\pi^0)$ events generated and processed	18000		
4.1	Beta Skim/Candidate Finding/Truth Match	7708	42.8	42.8
4.2	High-Energy Photon Quality			
	No problematic channels	7605	98.7	42.2
	$N_{xtal} > 4$	7605	100.0	42.2
	Second Moment < 0.002	7455	98.0	41.4
	$-0.74 < \cos\theta_\gamma < 0.93$	7327	98.3	40.7
	25 cm Isolation from Neutral bumps	6801	92.8	37.8
	25 cm Isolation from Charged bumps	6651	97.8	37.0
	π^0 Veto	6416	96.5	35.6
	η^0 Veto	6154	95.9	34.2
4.4	Charged-Track Quality			
	$K^\pm$ Track requirements	5794	94.2	32.2
	$K^\pm$ particle ID	4734	81.7	26.3
4.5	$K^\pm\pi^0$ invariant mass requirement			
	$0.8\,\mathrm{GeV}/c^2 < m_{K^\pm\pi^0} < 1.0\,\mathrm{GeV}/c^2$	4171	88.1	23.2
4.6	Fit Region			
	$-0.3\,\mathrm{GeV} < \Delta E < 0.3\,\mathrm{GeV}$	4033	96.7	22.4
	$5.2\,\mathrm{GeV}/c^2 < m_{ES} < 5.29\,\mathrm{GeV}/c^2$	4033	100.0	22.4
5.5	Neural Net Cut			
	$NN_{OUT} > 0.68$	3078	76.3	17.1
6.1	Best Candidate Selection			
	Best Candidate Selection	2973	96.6	16.5
	Overall efficiency (truth matched)	2973		16.5
	Overall efficiency (releasing truth match)	3403		18.9
	Expected signal yield in 81.3 fb^{-1}	215.2		

Table 6.1. Cut table for signal Monte Carlo. The last column states the cumulative efficiency and the second last column states the relative efficiency of the cut.

- Another B meson background category is due to all other B meson decays but $b \to s\gamma$ transitions. As an example, the $B \to K^*\eta$ ($\eta \to \gamma\gamma$) decay can occur where the η can decay in the laboratory frame into two photons with very different energies and the low energy photon is not reconstructed, therefore, the η is not vetoed and the high–energy photon from the η decay is identified as the high–energy photon from a $B \to K^*\gamma$ decay.

The ΔE and m_{ES} distributions for the three different types of B meson backgrounds can be seen in Figure 6.1 for the neutral B meson decays and in Figure 6.2 for the charged B meson decays.

6.4 Background Yields

The expected background yields before the neural net cut is applied can be seen in Table 6.2. The expected off peak data yield is included for comparison with the continuum background Monte Carlo. At this stage of the analysis the Monte Carlo agrees with the offpeak data within three standard deviation. The same table with neural net cut applied and thus with overall expected number of events in the onpeak data is shown in Table 6.3. The expected off peak data yield is again included for comparison with the continuum background Monte Carlo. In this case the Monte Carlo agrees with the offpeak data within one standard deviation. Thus, the neural net cut improves the agreement between offpeak data and continuum Monte Carlo.

6.5 Combined Shapes in the Fit Region

The ΔE and m_{ES} distributions for all Monte Carlo samples combined according to their integrated luminosities can be seen in Figure 6.3 (a) for the ΔE shape and in Figure 6.3 (b) for the m_{ES} shape.

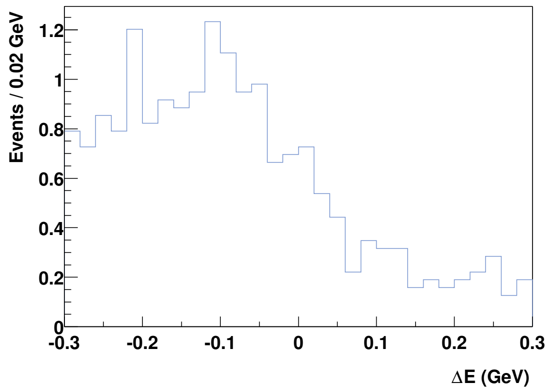

(a) $B^0 \to K^{*0}\gamma$ generic + *c.c.* Monte Carlo ΔE distribution.

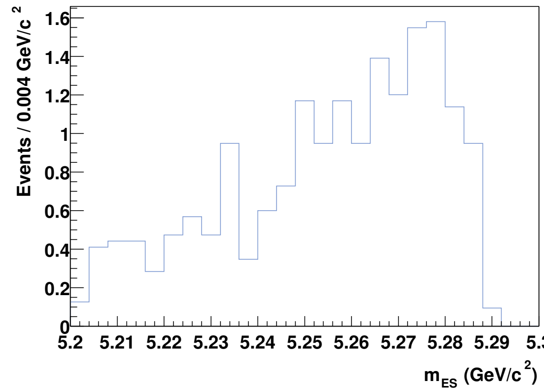

(b) $B^0 \to K^{*0}\gamma$ generic + *c.c.* Monte Carlo m_{ES} distribution.

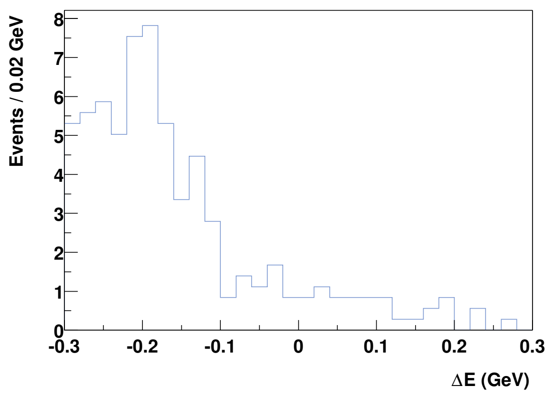

(c) $B^0 \to X_{sd}\gamma$ + *c.c.* Monte Carlo ΔE distribution.

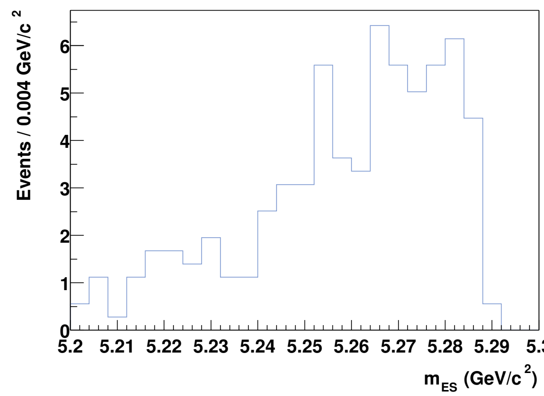

(d) $B^0 \to X_{sd}\gamma$ + *c.c.* Monte Carlo m_{ES} distribution.

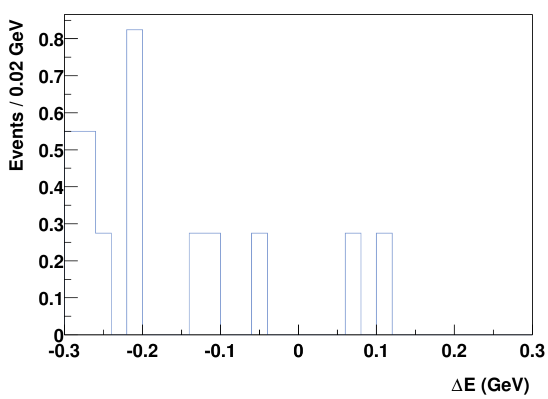

(e) $B^0\bar{B}^0$ generic Monte Carlo ΔE distribution.

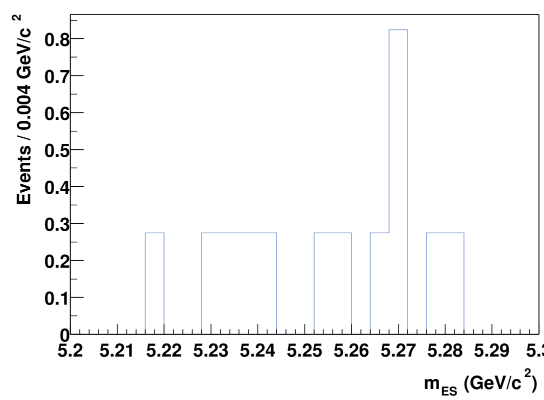

(f) $B^0\bar{B}^0$ generic Monte Carlo m_{ES} distribution.

Figure 6.1. Neutral B meson background shapes in the fit region. The plots on the left hand side show the ΔE distributions and the plots on the right hand side show the m_{ES} distributions. All analysis cuts are applied.

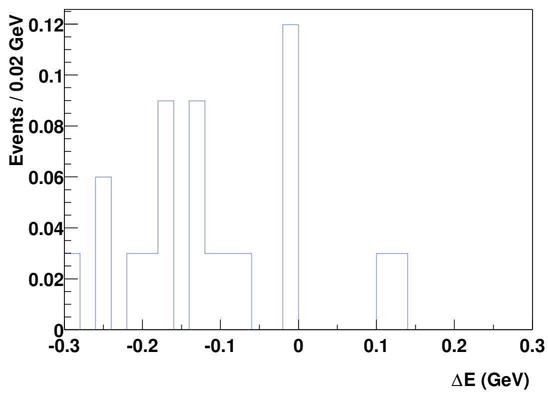

(a) $B^{\pm} \to K^{*\pm}\gamma$ generic Monte Carlo ΔE distribution.

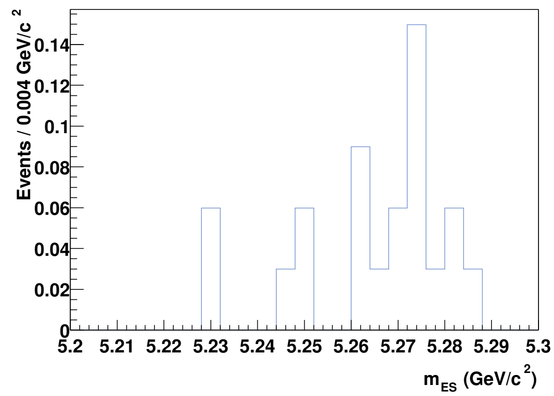

(b) $B^{\pm} \to K^{*\pm}\gamma$ generic Monte Carlo m_{ES} distribution.

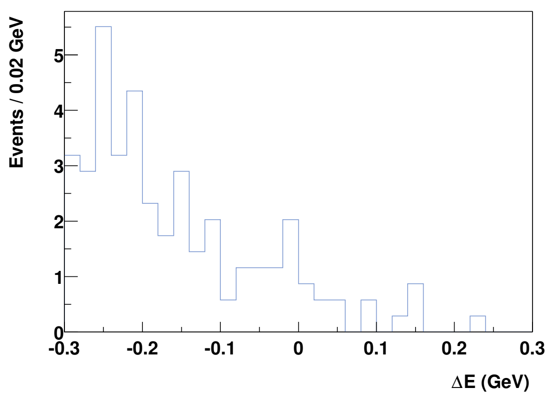

(c) $B^{+} \to X_{su}\gamma\ +\ c.c.$ Monte Carlo ΔE distribution.

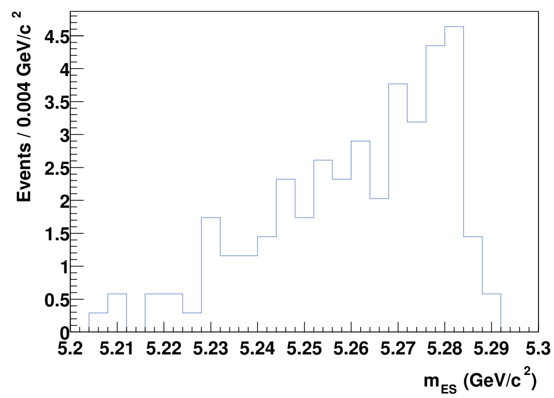

(d) $B^{+} \to X_{su}\gamma\ +\ c.c.$ Monte Carlo m_{ES} distribution.

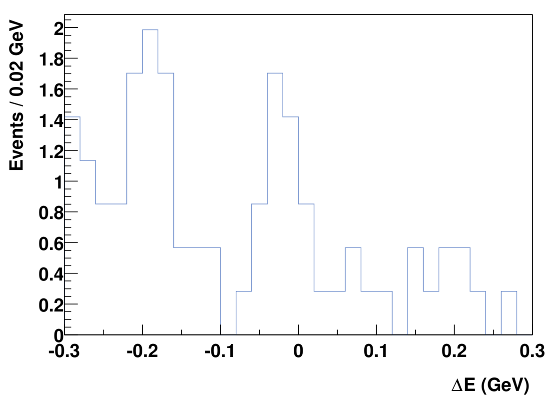

(e) $B^{+}B^{-}$ generic Monte Carlo ΔE distribution.

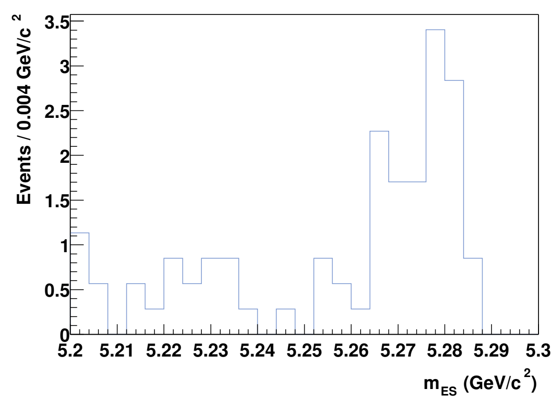

(f) $B^{+}B^{-}$ generic Monte Carlo m_{ES} distribution.

Figure 6.2. Charged B meson background shapes in the fit region. The plots on the left hand side show the ΔE distributions and the plots on the right hand side show the m_{ES} distributions. All analysis cuts are applied.

		All cuts except NN	
	Lumi. (fb^{-1})	Raw Yield	81.3 fb^{-1} Exp.
$B^0\bar{B}^0$ generic	295.79	39	10.7 ± 1.7
B^+B^- generic	286.53	155	44.0 ± 3.5
$B^0 \to X_{sd}\gamma$ + c.c.	291.00	413	115.3 ± 5.7
$B^+ \to X_{su}\gamma$ + c.c.	280.42	274	79.4 ± 4.8
$B^0 \to K^{*0}\gamma$ generic + c.c.	2571.43	1763	55.8 ± 1.3
$B^+ \to K^{*+}\gamma$ generic + c.c.	2714.29	46	1.4 ± 0.2
Sum of B backgrounds			306.6 ± 8.5
$e^+e^- \to u\bar{u}, d\bar{d}, s\bar{s}$	39.90	3732	7604.3 ± 124.5
$e^+e^- \to c\bar{c}$	42.09	1822	3519.6 ± 82.5
$e^+e^- \to \tau^+\tau^-$	45.70	151	268.6 ± 21.9
$uds + c\bar{c} + \tau^+\tau^-$			11392.5 ± 151.0
Off-Resonance Data	9.49	1440	12335.1 ± 325.1

Table 6.2. Background yields without neural net cut applied. The errors stated are purely statistical.

		All cuts with NN	
	Lumi. (fb^{-1})	Raw Yield	81.3 fb^{-1} Exp.
$B^0\bar{B}^0$ generic	295.79	13	3.6 ± 1.0
B^+B^- generic	286.53	73	20.7 ± 2.4
$B^0 \to X_{sd}\gamma$ + c.c.	291.00	240	67.0 ± 4.3
$B^+ \to X_{su}\gamma$ + c.c.	280.42	137	39.7 ± 3.4
$B^0 \to K^{*0}\gamma$ generic + c.c.	2571.43	569	18.0 ± 0.8
$B^+ \to K^{*+}\gamma$ generic + c.c.	2714.29	20	0.6 ± 0.1
Sum of B backgrounds			149.6 ± 6.1
$e^+e^- \to u\bar{u}, d\bar{d}, s\bar{s}$	39.90	295	601.1 ± 35.0
$e^+e^- \to c\bar{c}$	42.09	202	390.2 ± 27.7
$e^+e^- \to \tau^+\tau^-$	45.70	6	10.7 ± 4.4
$uds + c\bar{c} + \tau^+\tau^-$			1002.0 ± 44.9
Off-Resonance Data	9.49	119	1019.4 ± 93.4

Table 6.3. Background yields with neural net cut applied. The errors stated are purely statistical.

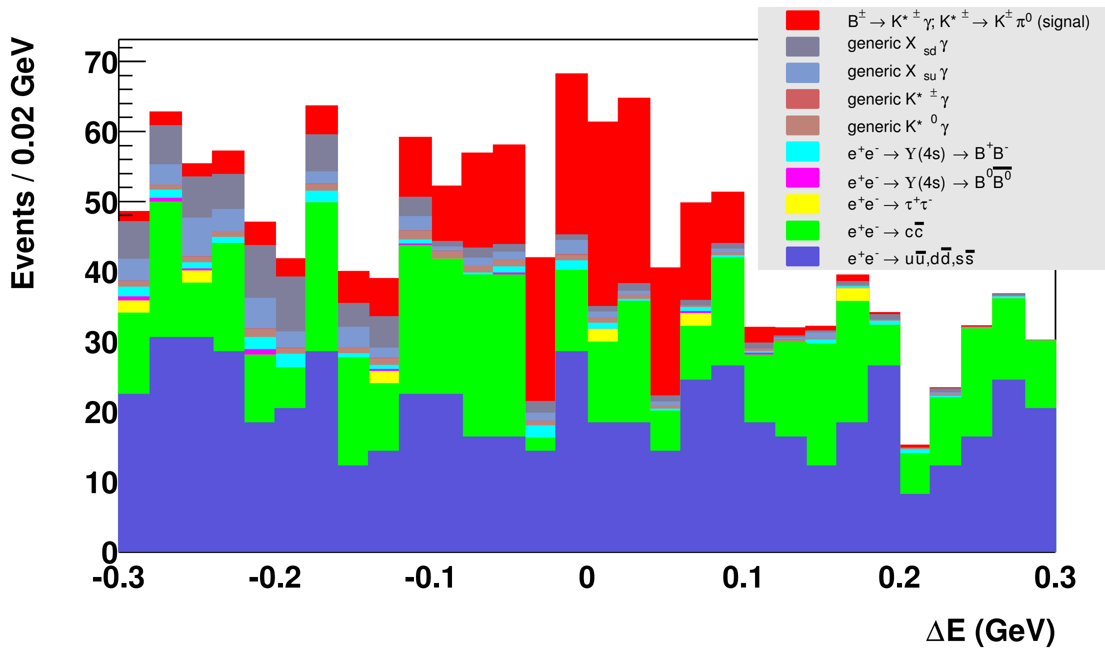

(a) Monte Carlo ΔE distribution.

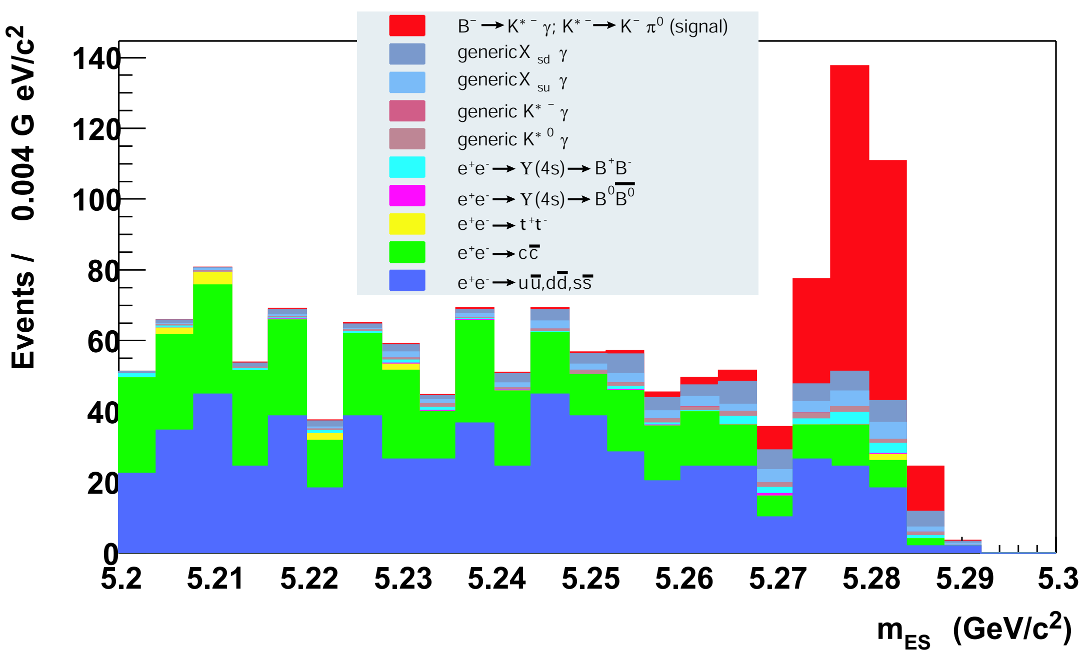

(b) Monte Carlo m_{ES} distribution.

Figure 6.3. Combined Monte Carlo distributions in the fit region. The upper plot shows the ΔE distribution and the lower plot shows the m_{ES} distribution. All analysis cuts are applied and the signal events are not required to be truth matched.

CHAPTER 7

SIGNAL FIT

7.1 Overview

The final fit to the real data is done with a two dimensional probability density function (PDF) in ΔE and m_{ES}. The two dimensional region in which the fit is performed has been defined previously in Section 4.6, as a reminder,

- Fit region: $(-0.3\,\mathrm{GeV} < \Delta E < 0.3\,\mathrm{GeV}) \times (5.2\,\mathrm{GeV}/c^2 < m_{ES} < 5.29\,\mathrm{GeV}/c^2)$.

In comparison with the one dimensional fit in m_{ES} done in the previous analysis [12], the extension to a two dimensional fit allows for the determination of the number of B background events. Therefore, there is no need to correct the signal yield in the end due to peaking B background events in m_{ES}. The most distinct feature of the B background is its rising shape for negative ΔE values. The fit performed in this analysis therefore has three floating event yield parameters, one for the signal yield, one for the continuum background yield and one for the B background yield.

The signal is extracted with an unbinned maximum likelihood fit. Such a fit has the advantage of being free from binning systematics.

7.2 Construction of the Probability Density Function

As mentioned before, the PDF consists of three main parts for the onpeak data fit and another part for a simultaneous fit to the offpeak data:

- The PDF describing the signal events (not requiring truth match) has been built by multiplying two simple one–dimensional PDFs and extending the resulting shape function with a multiplicative poisson factor for the signal yield.

- The first one–dimensional PDF describes the signal in ΔE with a Crystal Ball function (see Appendix A) where the mean and the width of the peak are floating in the fit but the power n of the tail and the attachment point α of the tail are fixed to the values extracted from the signal Monte Carlo.
- The second one–dimensional PDF describes the signal in m_{ES} also with a Crystal Ball function (see Appendix A) where the mean and the width of the peak are again floating in the fit. The power n of the tail and the attachment point α of the tail are fixed to the values extracted from the signal Monte Carlo.

• The continuum background events are described with a two–dimensional PDF consisting of two simple one–dimensional PDFs multiplied with each other. The resulting shape function is also extended with a multiplicative poisson factor for the continuum background yield. The two one–dimensional PDFs for the continuum background in the onpeak dataset are:

  - A first order polynomial with one floating parameter is used to describe the ΔE shape.
  - The m_{ES} shape is described with an Argus function (see Appendix A) where the endpoint E_{BEAM} is fixed to the kinematical endpoint of $5.29\,\mathrm{GeV}/c^2$. The Argus parameter ξ is allowed to float in the fit.

• The PDF describing the B background also consists of the product of two one dimensional PDFs. Again, the resulting shape function is also extended with a multiplicative poisson factor for the B background yield. These two PDFs are:

  - The ΔE shape is described by a Gaussian function (see Appendix A) with all parameters fixed (mean and σ) to the values extracted from Monte Carlo.

  - In m_{ES}, the B background events are described by a Novosibirsk function (see Appendix A) with all three parameters (mean, σ and the tail parameter τ) fixed to the values extracted from the corresponding Monte Carlo.

- In addition, a simultaneous fit to the offpeak dataset is performed. The PDF describing this part of the fit is the same PDF as used to describe the continuum background events in the onpeak dataset. The shape parameters are shared by these two fits. Thus, the simultaneous fit to the continuum background of the onpeak data and the offpeak data improves the separation between continuum background events and B background events in the onpeak dataset. The parameter for the number of offpeak events is fixed to the number of events in the offpeak data set.

The Crystal Ball function for the signal in ΔE is necessary to account for energy leakage from the high–energy photon and the π^0 in the EMC (see Section 2.3.4). Thus the ΔE signal distribution is expected to have a long tail at negative ΔE values. Also, the m_{ES} distribution is expected to be slightly asymmetric. m_{ES} has been rescaled by adjusting the high–energy photon momentum in order to account for the energy leakage of this high–energy photon in the EMC. But the photons originating from the π^0 also experience some energy leakage in the EMC. Thus, even in the high energy photon rescaled m_{ES} distribution there is a residual asymmetry due to the energy leakage of the π^0. This is accounted for by using the Crystal Ball function for the signal in m_{ES}.

An overview of the functions for the different parts of the total PDF is given in Table 7.1. The results of the separate one–dimensional fits to the Monte Carlo samples are shown in Figure 7.1. The result of the fit to the combined onpeak Monte Carlo sample and simultaneously to the offpeak data can be seen in Figure 7.2. The projections to the different Monte Carlo sub samples (b) and to the offpeak data (c) are also shown in the same figure.

	Function used
signal ΔE	Crystal Ball (2)
signal m_{ES}	Crystal Ball (2)
Continuum background ΔE and offpeak data ΔE	1^{st}-order polynomial (1)
Continuum background m_{ES} and offpeak data m_{ES}	Argus (1)
B-meson background ΔE	Gaussian (0)
B-meson background m_{ES}	Novosibirsk (0)

Table 7.1. Used functions to build the combined PDF. The number of floating shape parameters is given between parenthesis.

7.3 Correlations between ΔE and m_{ES}

The total PDF assumes no correlation between ΔE and m_{ES} for the individual components. This is checked with the events passing all the selection criteria. The result is shown in Table 7.2 and shows no large correlations for background events. The relatively large correlation between ΔE and m_{ES} for signal Monte Carlo has been studied further with embedded toy Monte Carlo studies (see Section 7.6).

Continuum MC	-0.021
Off-peak Data	0.058
Generic B MC	0.018
Signal MC	0.185

Table 7.2. Correlations between ΔE and m_{ES}. Shown are continuum background Monte Carlo, off-peak data, generic B Monte Carlo and signal Monte Carlo correlations. The events are required to be in the fit region and to satisfy all selection criteria.

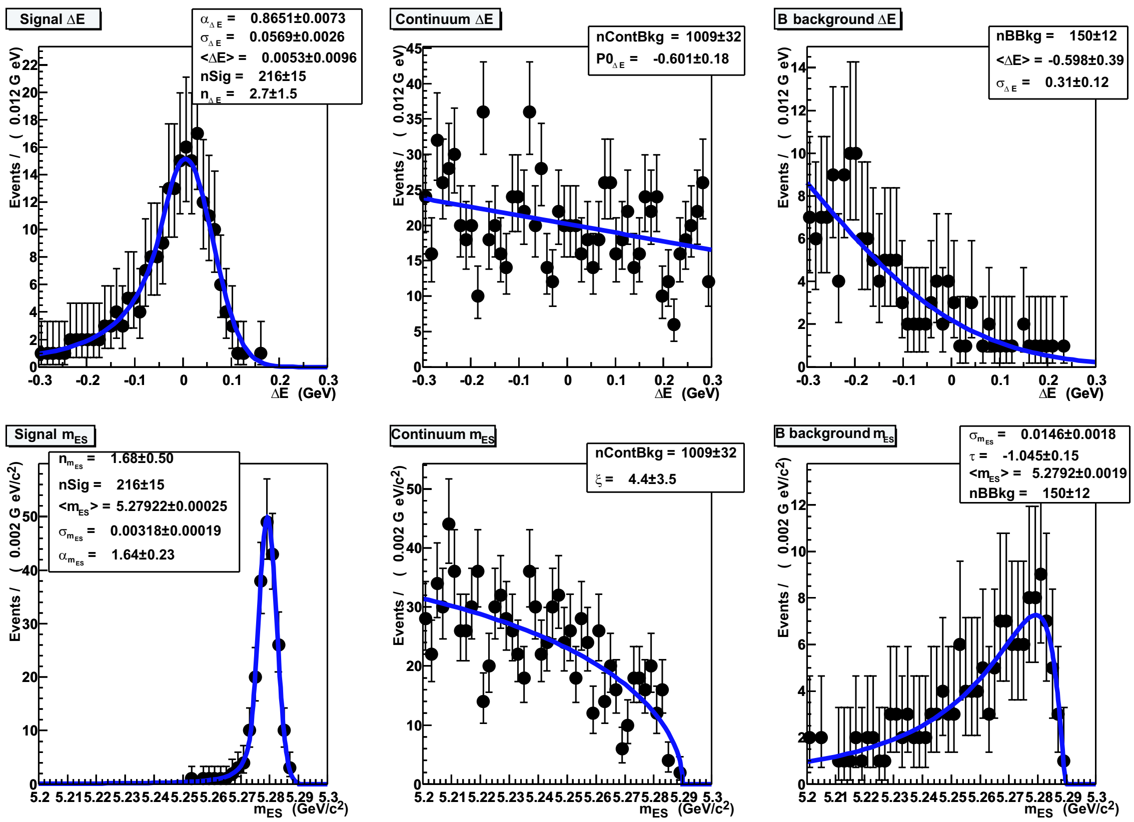

(a) Six separate fits to Monte Carlo.

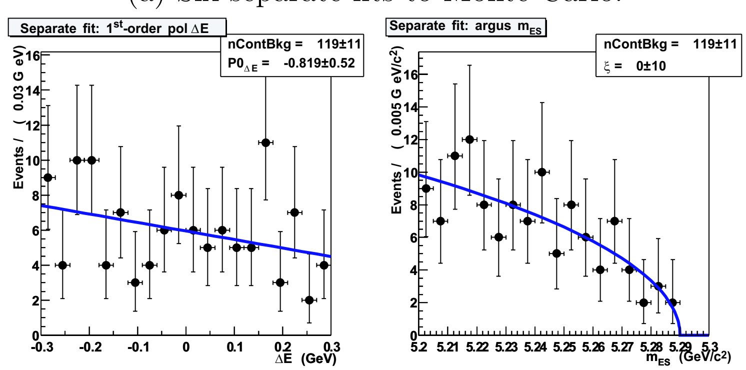

(b) Fit to off-peak data in ΔE and m_{ES}.

Figure 7.1. Separate fits to individual Monte Carlo distributions. First plot: Six separate fits to the six different parts of the SP4 Monte Carlo. First Row (ΔE): signal (no truth match is required), continuum background, B background. Second Row (m_{ES}): signal (no truth match is required), continuum background, B background. Second plot: Fit to offpeak data in ΔE and m_{ES}

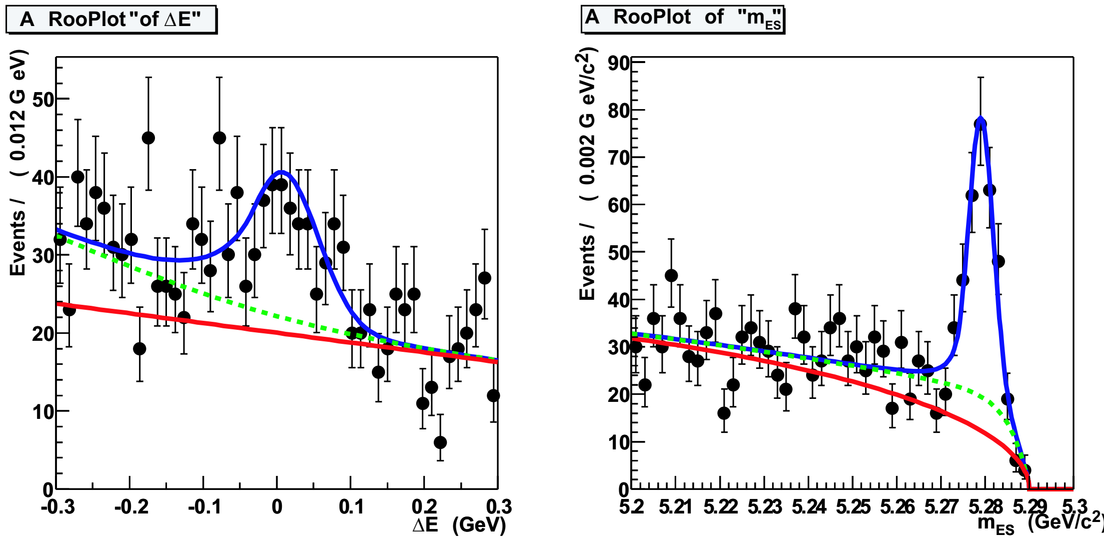

(a) Combine fit to Monte Carlo.

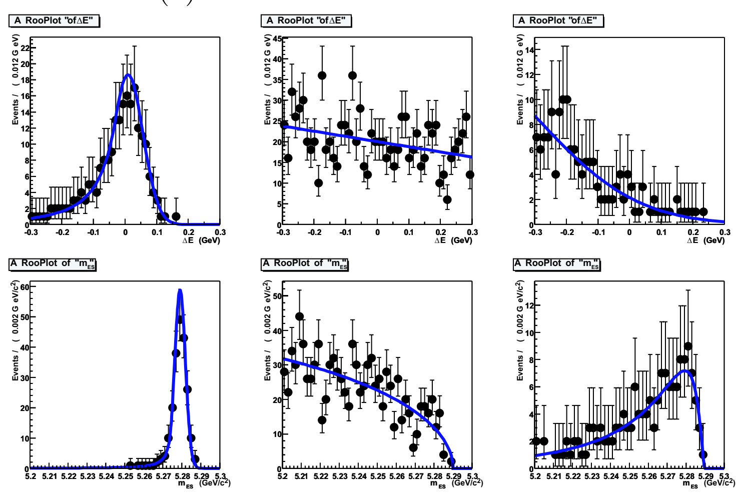

(b) Projections of the combined fit to the different Monte Carlo sub-samples.

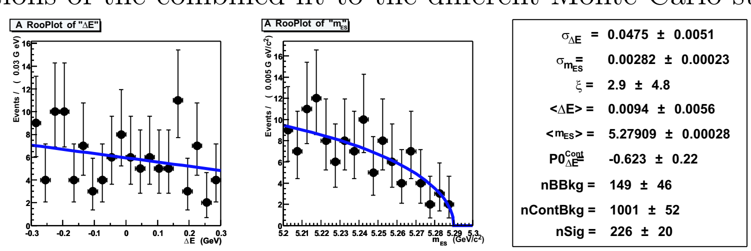

(c) Projections of the combined fit to the off-peak data and fit parameters.

Figure 7.2. Full fit to SP4 Monte Carlo. First plot: Combined simultaneous fit to the SP4 Monte Carlo and to the off-peak data for $K^{*+} \rightarrow K^+\pi^0$ (blue = signal, green-dashed = B-background, red = continuum background MC). Second Plot: Projections to the different Monte Carlo sub-samples; first Row (ΔE): non truth matched signal, continuum background, B background. Second Row (m_{ES}): non truth matched signal, continuum background, B background. Third plot: Projection to the offpeak data in ΔE (left) and m_{ES} (middle), the resulting fit parameters for the combined simultaneous fit are listed on the right.

7.4 Monte Carlo Studies

In order to test the self consistency of the PDF and also in order to study the changes in the fit results due to statistical fluctuations, "toy" Monte Carlo studies have been performed. A toy Monte Carlo experiment is a data sample that was generated according to the PDF line shapes obtained from the different fits to SP4 Monte Carlo. Also, the number of events generated for each sub sample (signal, continuum background and B background) is varied according to a Poisson distribution centered at the expected yields. With this technique, each toy Monte Carlo experiment is different from other toy Monte Carlo experiments due to statistical fluctuations. But on average, the parameter values used to generate these toy Monte Carlo experiments should be found by the fit. This is measured by a pull distribution for each of the floating parameters. The pull of parameter P is defined as

$$Pull(P) = \frac{Fit\ Result\ of\ P - Expected\ Value\ of\ P}{Fit\ Error\ of\ P}\ . \tag{7.1}$$

If the fit yields the expected answer on average, the pull distribution is a normal distribution with a width of 1 and a mean of 0. If the mean is significantly different from zero, the fit is biased for the parameter in question. If the width differs from 1, the fit uncertainty for the given parameter is either over– or under–estimated.

A set of 500 toy Monte Carlo experiments has been generated according to the PDF in Figure 7.1 with one exception: The ΔE shape for the B background was changed to a double–gaussian for the generation of the toy Monte Carlo experiments. Different functions have been tested to fit the Monte Carlo B background shape in ΔE and the double–gaussian has been found to describe the SP4 Monte Carlo the best as can be seen in Figure 7.3. For the fit, the usual gaussian distribution is chosen in order to keep the number of parameters as small as possible.

The Pull plots for the floating parameters can be seen in Figure 7.4. Furthermore, the negative log likelihood (NLL) for this set of toy Monte Carlo experiments is shown in Figure 7.7 (a). A significant deviation from the expected normal distribution is not seen. Only the widths of the pull plots for the continuum background shape parameters are significantly smaller the 1. This is due to the use of the same offpeak dataset in all toy Monte Carlo experiments.

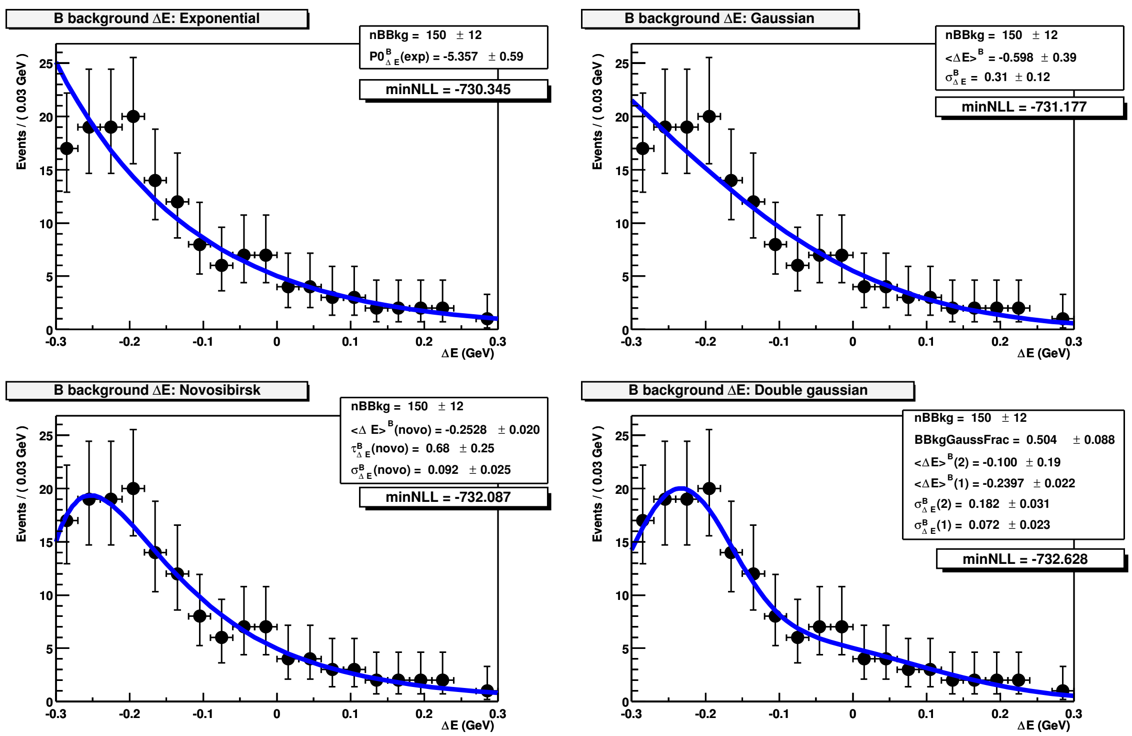

Figure 7.3. Comparison of ΔE line shapes for B background Monte Carlo.

7.5 Correlation between the Yields

The correlations between the three different yields have also been studied using the 500 toy Monte Carlo experiments. Scatter plots for different pairs of event yields are shown in Figure 7.5. The signal yield shows no strong correlation with the other two yields whereas the B background yield is anti–correlated with the continuum background yield (see Figure 7.5).

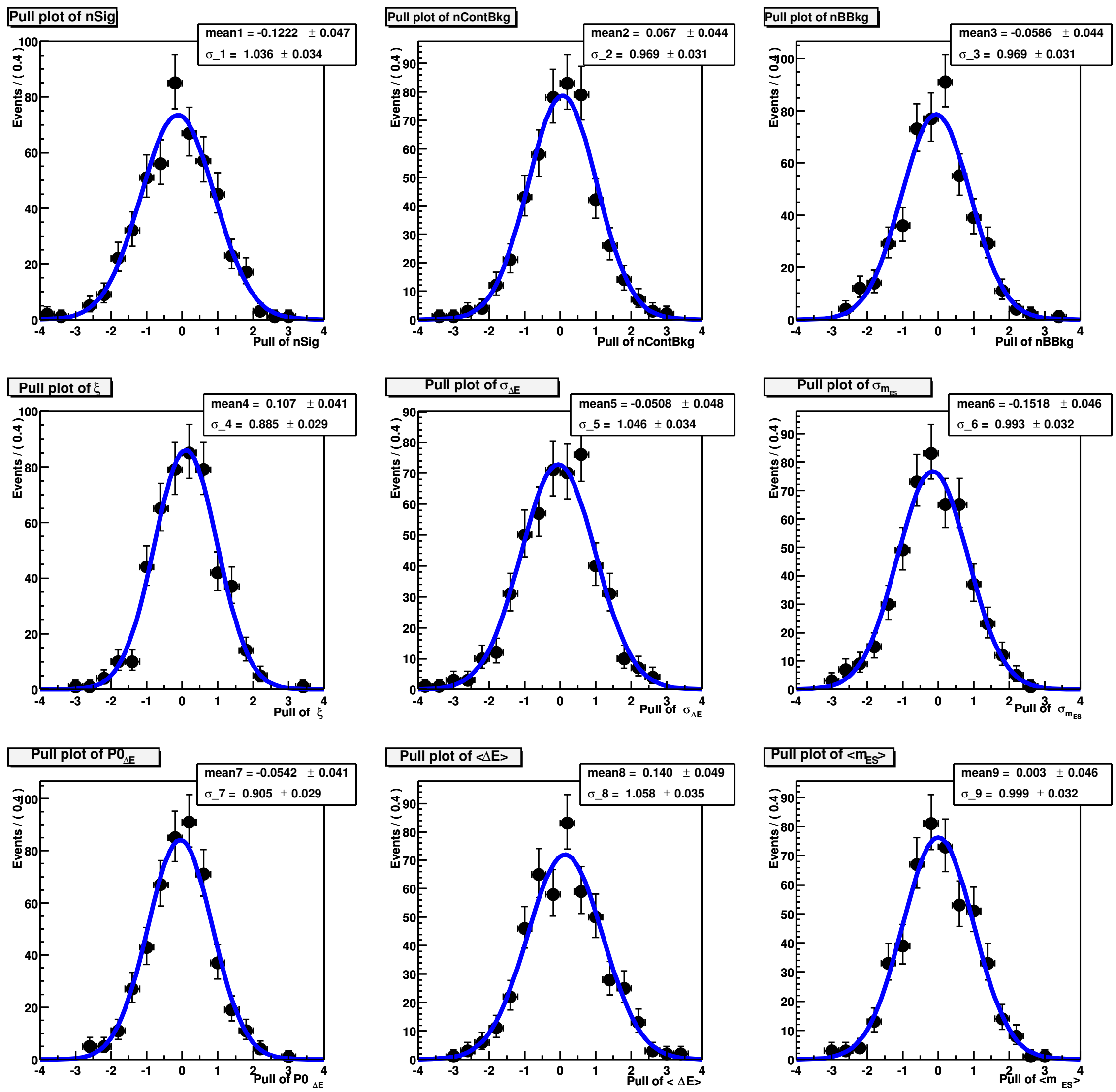

Figure 7.4. Pull distributions for pure toy Monte Carlo studies. Different PDFs have been used for the fitting and generating only in the ΔE shape of the B background.

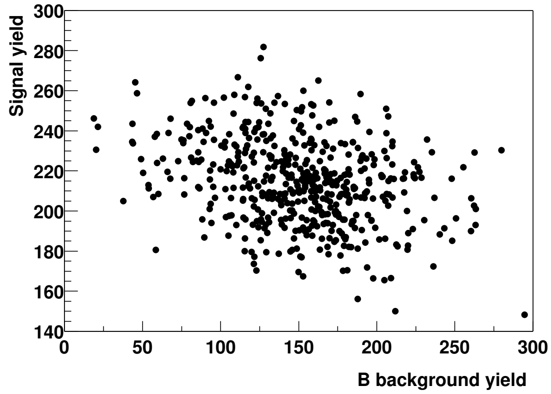

(a) Correlation between signal yield and continuum background yield.

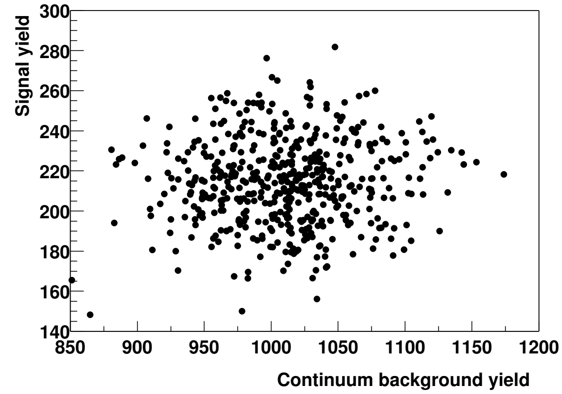

(b) Correlation between signal yield and B background yield.

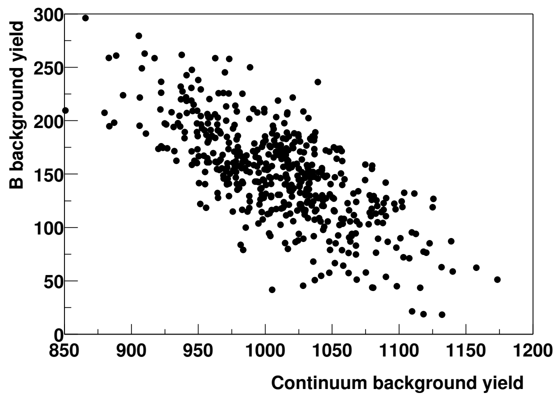

(c) Correlation between B background yield and continuum background yield.

Figure 7.5. Correlations between the three event yields. These data points are obtained from the fits to toy Monte Carlo experiments.

7.6 Embedded Toy Monte Carlo Studies

Embedded toy Monte Carlo studies make use of the availability of a large signal Monte Carlo dataset. This fully simulated dataset exceeds the expected number of signal events in the onpeak dataset by a factor of ≈ 16. This makes it possible to put together another set of toy Monte Carlo experiments by generating the background events as before according to the PDF line shapes but choosing the signal events from the fully simulated SP4 Monte Carlo. The number of signal events is chosen randomly from the fully simulated SP4 Monte Carlo according to a poisson distribution centered at the expected number of signal events. It is taken care of not choosing the same signal event for the same embedded toy Monte Carlo experiment.

The signal embedded toy Monte Carlo studies have been performed in order to study efficiency corrections due to correlations of the signal events between ΔE and m_{ES} and more important due to differences between the signal line shape parameterizations and the actual signal distributions.

A set of 500 signal embedded toy Monte Carlo experiments has been generated. The mean of each fit result is reliable, but the errors on the means of the fit results are too small due to the correlation between the signal events in one experiment and those in the other experiments. To compute the errors on the fit result average, one needs to take into account that only 16 independent signal experiments have been used. Thus, the correct error on the mean of the signal yield is computed by dividing the mean on the fit result error (see Figure 7.6) by the number of independent samples ($\sqrt{16}$). The shift between the number of expected signal events and the mean of the signal yield is $216 - 208.05 = 7.95 \pm 5.07$. Thus, the signal efficiency correction related with the uncertainty in the signal part of the fit is $208/216 = 0.963 \pm 2.4\%$. The NLL distribution for this signal embedded toy Monte Carlo study is shown in Figure 7.7 (b).

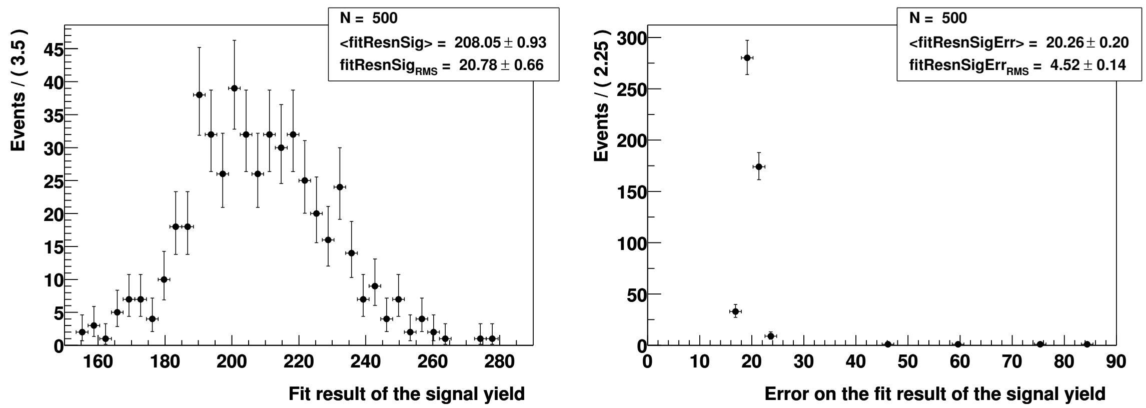

(a) Signal yield.

(b) Error on the signal yield.

Figure 7.6. Signal yield distribution for a embedded toy Monte Carlo study. (a) The signal yield is shown with its associated error (b).

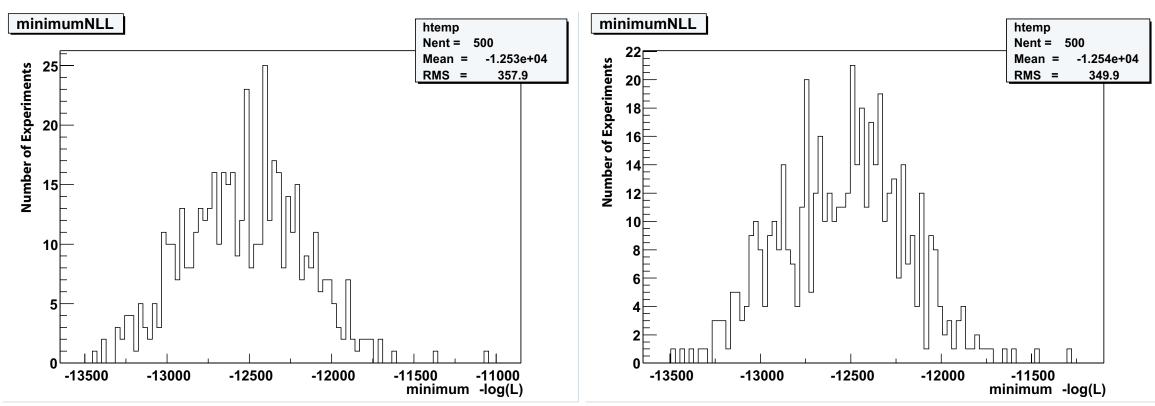

(b) NLL for pure toy Monte Carlo studies.

(c) NLL for signal embedded toy Monte Carlo studies.

Figure 7.7. Minimum negative log(Likelihood) for toy Monte Carlo studies. (a) For a pure toy Monte Carlo study and (b) for a signal embedded toy Monte Carlo study.

CHAPTER 8

SYSTEMATIC ERRORS

Sources of systematic error are extensively studied by specialized groups within the BaBar collaboration. Usually, one either has to simply use a number for a specific source of a systematic error or one is supposed to follow a recipe in order to determine the analysis–specific systematic error. Most systematic errors and efficiency corrections are due to differences between Monte Carlo and real data. These differences have been studied by analyzing a real data sample specifically suited for a study of the considered systematic error. This real data sample ("control sample") is compared with its corresponding Monte Carlo sample and the difference between these two is considered as an efficiency correction. The statistical error of this control sample is considered as a systematic error on the efficiency correction.

8.1 B Counting

A 1.1% systematic error on the number of $\Upsilon(4S)$ is considered. This error is due to the uncertainty in counting the number of processed $B\bar{B}$ events. This number is $(88.2 \pm 1.0) \times 10^6$ and thus leads to the 1.1% systematic error.

8.2 Tracking Efficiency Systematics

The systematic error for the GTL selection is taken into account by applying a bin–by–bin correction to the charged track in the signal event. The systematic error for this correction is 0.8%.

8.3 Charged Particle ID Systematics

The systematic uncertainty for the kaon identification efficiency has been taken into account with a 1% systematic error.

8.4 Neutrals Systematics

Two neutral candidates need to be considered in this analysis: The high–energy photon and the π^0. There are two main differences between neutral candidates in real data and in SP4 Monte Carlo. The first difference is the number of reconstructed π^0 as a function of energy. The second one is the difference in the π^0 mass width which is due to different energy resolution for photons in data and Monte Carlo.

These issues have been studied with a sample of $\tau^+\tau^-$ events by the Neutral Reconstruction Analysis Working Group, as described on their web page [26]. Following their recipe, the neutrals systematic study involves two steps. The first step consists of smearing and rescaling the energy of the photons to achieve better agreement in the π^0 width for data and Monte Carlo. The second step accounts for differences in the number of π^0s reconstructed in data and Monte Carlo by applying an energy–dependent π^0 killing.

Two kinds of errors are considered, correlated and uncorrelated errors. The overall correlated error is 7.5%, 2.5% for the high–energy photon and 5% for the π^0. This error comes from the error on the branching fraction for the τ decays used in the study (1.6%), the error on the analysis with and without photon energy smearing applied (2%), the error from the embedding of the π^0s in a hadronic event ($\tilde{1}$%) and in the case of two photons in the same EMC cluster, the difference in the fit line leads to another error (3%). The source for the uncorrelated error is dominated by statistics. Other sources for this error are the lower cut on the π^0 energy at 1 GeV in the τ study and the difference between a simple π^0 counting and the result of a fit to the π^0 mass peak.

The total error is then achieved by processing the signal Monte Carlo twice. First with applied smearing and rescaling of the energy of the photons and with the energy dependent π^0 killing alone. This first time, the uncorrelated errors are not considered in the processing. The same Monte Carlo is processed a second time taking also the uncorrelated errors into account. The difference in the numbers of signal events (no truth matching is required) in these two runs on SP4 signal Monte Carlo gives the uncorrelated error. To obtain the total error on the neutrals, the uncorrelated error is added in quadrature with the 7.5% correlated error. The result of these two different processing methods is listed in Table 8.1.

Number of signal events in fit region (raw numbers, no truth match required) for run				
without corrections	with corrections, no uncorrelated error	with corrections and uncorrelated error	Resulting uncorrelated error	Resulting total error
3,403	3,340	3,290	1.5%	7.6%

Table 8.1. Neutrals systematics. Obtaining the systematic error of the π^0 and the high energy photon from the number of events of signal events (no truth match required) for the runs with and without uncorrelated errors.

8.5 Photon Selection Systematics

The systematic errors for the π^0 and η veto cuts and the photon isolation cuts have been studied in the previous *BaBar* analysis [12]. The errors were found to be 1% and 2% respectively.

8.6 Neural Network Systematics

The systematics related to the neural network have been studied by Ping Tan using a $B \to D\pi$ control sample. The discrepancy between Monte Carlo and real data for this control sample is considered as an efficiency correction and the statistical error on this control sample is considered as a systematic error. The efficiency correction due to the neural network used in this analysis is found to be 0.998 with a systematic error of 2.7%.

8.7 B Background Systematics

The systematics due to the fixed line shapes for the B background are studied by varying these fixed parameters in the onpeak data fit and determining the effect on the signal yield. The parameters are varied by one sigma from the fit to Monte Carlo. The parameter variations are also combined in order to achieve maximal variations in the PDF shape. It is found that the signal yield changed by at most 3 events, corresponding to a systematic error of 1.2%.

8.8 Fit Model Systematics

The efficiency correction and the corresponding systematic error due to discrepancies between the line shapes of the PDFs and the actual event distribution in data needed to be studied. Describing a data distribution with a simple mathematical function (in this case a PDF) is not accurate. This difference has been studied with signal embedded toy Monte Carlo studies described in Section 7.6. The result of this study is an efficiency correction of 0.963 with a systematic error of 2.4%.

8.9 Monte Carlo Statistics

The signal efficiency is calculated with the signal Monte Carlo simulation. The uncertainty on the signal efficiency due to the statistics of this signal Monte Carlo is also considered as a systematic error.

Uncorrected Efficiency	0.189	
	Efficiency Correction	Systematic Error (σ)
B Counting	1.000	1.1%
Tracking Eff	0.995	0.8%
PID	1.000	1.0%
Neutrals Efficiency	0.981	7.6%
Distance cut	1.000	2.0%
$\pi^0(\eta)$ veto	1.000	1.0%
Neural network	0.998	2.7%
B background	1.000	1.2%
Fit Model	0.963	2.4%
MC statistics	1.000	1.7%
Total Correction	0.938	9.1%
Corrected Efficiency	0.177	9.1%
Sub-Mode Branching Fraction	0.333	

Table 8.2. Efficiency corrections and systematic errors. The efficiency corrections are multiplied and the systematic errors are summed in quadrature.

8.10 Total Systematic Error

A summary of all efficiency corrections together with the corresponding systematic errors is listed in Table 8.2. The total efficiency correction is 0.938 and the total systematic uncertainty on this is 9.1%.

CHAPTER 9

RESULTS

9.1 Unblinded Fit Results

The fit result to the onpeak data for the $K^{*+} \rightarrow K^+\pi^0$ mode is shown in Figure 9.1. The signal yield is $250.9^{+23.2}_{-21.8}$, approximately two sigmas higher than the assumed central value (see Table 1.3). The continuum background yield is 1124.1 $\pm$ 52.9, approximately 2.5 sigmas higher than expected; and the B background yield is 18.1 $\pm$ 44.9, about three sigmas lower than expected. A comparison between the results of the individual fits to the separate Monte Carlo samples and the combined fit to Monte Carlo and real data is shown in Table 9.1.

9.2 Discussion of B Background Yield

Since the fitted B background yield is much lower than expected, we thought about reasons for this. The first reason is that the B background yield is anticorrelated with the continuum background yield. Thus, a sizable portion of B background events is probably picked up by the continuum background part of the fit. Furthermore, there is a shift in ΔE between data and Monte Carlo. Since the B background is peaked at low ΔE, this shift cuts out about 20% of the B background events. Also, as suggested in [27], the ratio of one pion events vs. two pion events in the inclusive $B \rightarrow X_s\gamma$ Monte Carlo is too high by a factor of 2.5 with respect to real data. Since in ΔE, we are mostly sensitive to the one pion modes, this can also explain part of the low B background yield. A new toy Monte Carlo study has been performed based on these two assumptions:

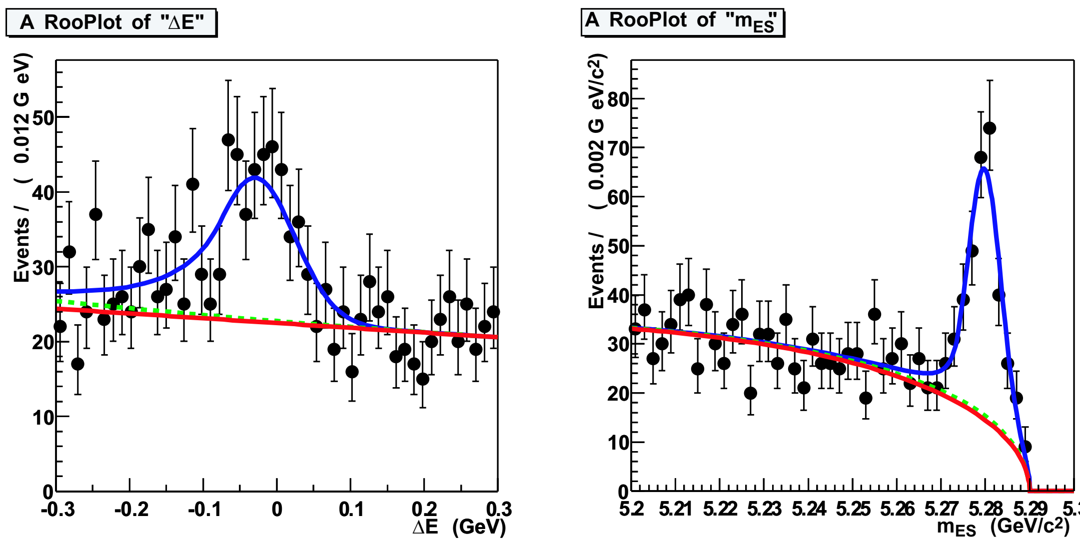

(a) On peak data.

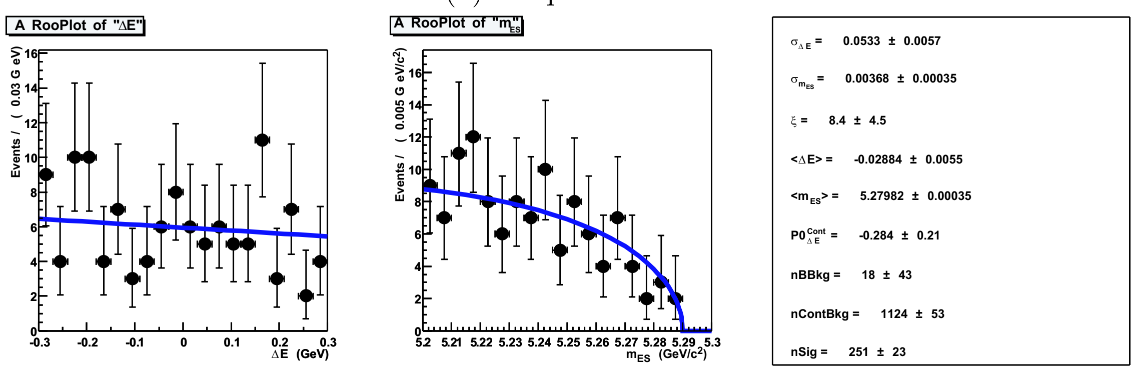

(b) Off peak data and fit results.

Figure 9.1. Fit result for the real data fit.

Fit parameter	Individual fits to Monte Carlo	Fit result for a combined fit to Monte Carlo	Real data
Signal Yield	216 ± 15	226 ± 20	250.9 ± 22.6
Continuum Background Yield	1009 ± 32	1001 ± 52	1124.1 ± 52.9
B Background Yield	150 ± 12	149 ± 46	18.1 ± 44.9
$< m_{ES} >$ (GeV/c^2)	5.27922 ± 0.00025	5.27909 ± 0.00028	5.2798 ± 0.00035
$< \Delta E >$ (GeV)	0.0053 ± 0.0096	0.0094 ± 0.0056	-0.0289 ± 0.0055
$\sigma_{m_{ES}}$ (MeV/c^2)	3.18 ± 0.19	2.82 ± 0.23	3.68 ± 0.35
$\sigma_{\Delta E}$ (MeV)	56.9 ± 2.6	47.5 ± 5.1	53.3 ± 5.7
ξ	4.4 ± 3.5	2.9 ± 4.8	8.36 ± 4.51
ξ (offpeak data)	0.0 ± 10	2.9 ± 4.8	8.36 ± 4.51
$P0_{\Delta E}$	-0.601 ± 0.18	-0.623 ± 0.22	-0.282 ± 0.213
$P0_{\Delta E}$ (offpeak data)	-0.819 ± 0.52	-0.623 ± 0.22	-0.282 ± 0.213

Table 9.1. Comparison of fit results between Monte Carlo and real data.

- Shift in ΔE by $-38\,\mathrm{MeV}$ and
- Scaling the inclusive $B \to X_s\gamma$ Monte Carlo down with a factor of 0.4.

The distribution of the fitted B background yield is shown in Figure 9.3(b) for this new toy Monte Carlo study. The comparison with the usual old toy Monte Carlo study (Figure 9.3(a)) shows that the probability of the observed low B background yield in the onpeak data increases from about 1% to about 10%.

9.3 The $K^\pm\pi^0$ Invariant Mass Peak

In order to ensure that all $K^{*\pm}$ candidates are really due to a $K^{*\pm}$ decay and not due to non resonant $K^\pm\pi^0$, the $K^\pm\pi^0$ invariant mass for signal events needs to be plotted. This plot is done by only choosing event from the ΔE–m_{ES} signal region and plotting the $K^\pm\pi^0$ invariant mass in a reasonable window around the expected $K^{*\pm}$ mass peak. In order to account for the non signal events (continuum and B background) in the signal region, the events from the m_{ES} sideband are subtracted from the signal region events. The events from the m_{ES} sideband are scaled in order

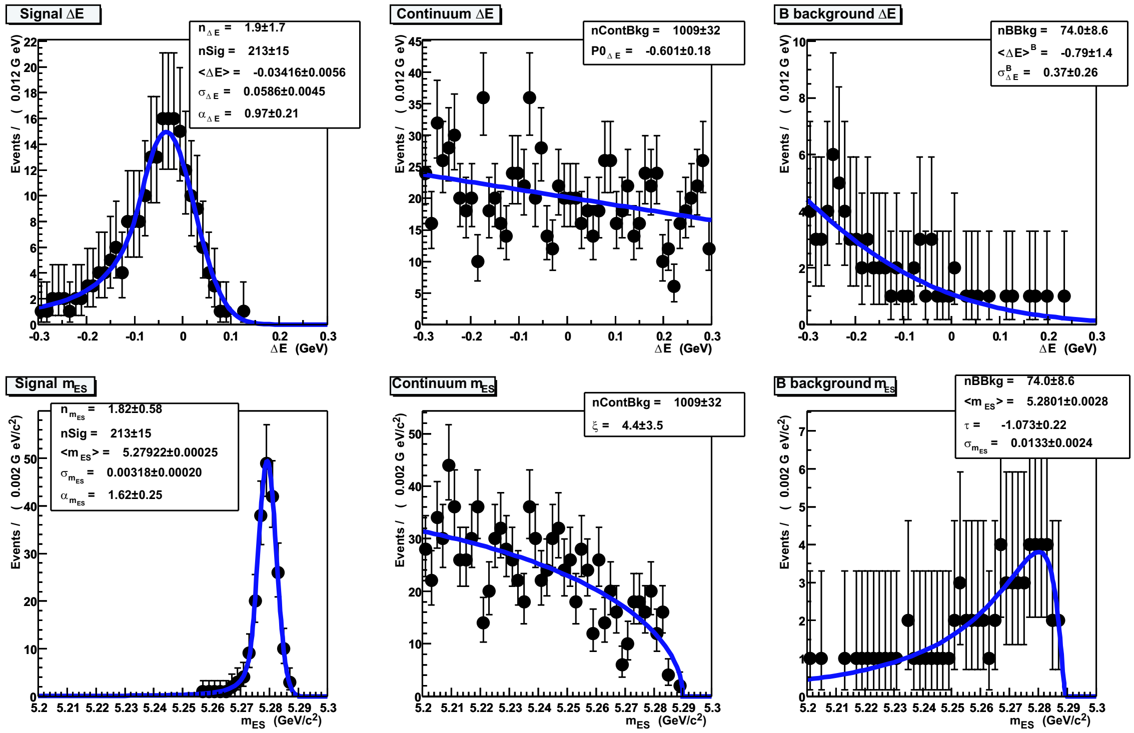

(a) Separate fits to the Monte Carlo.

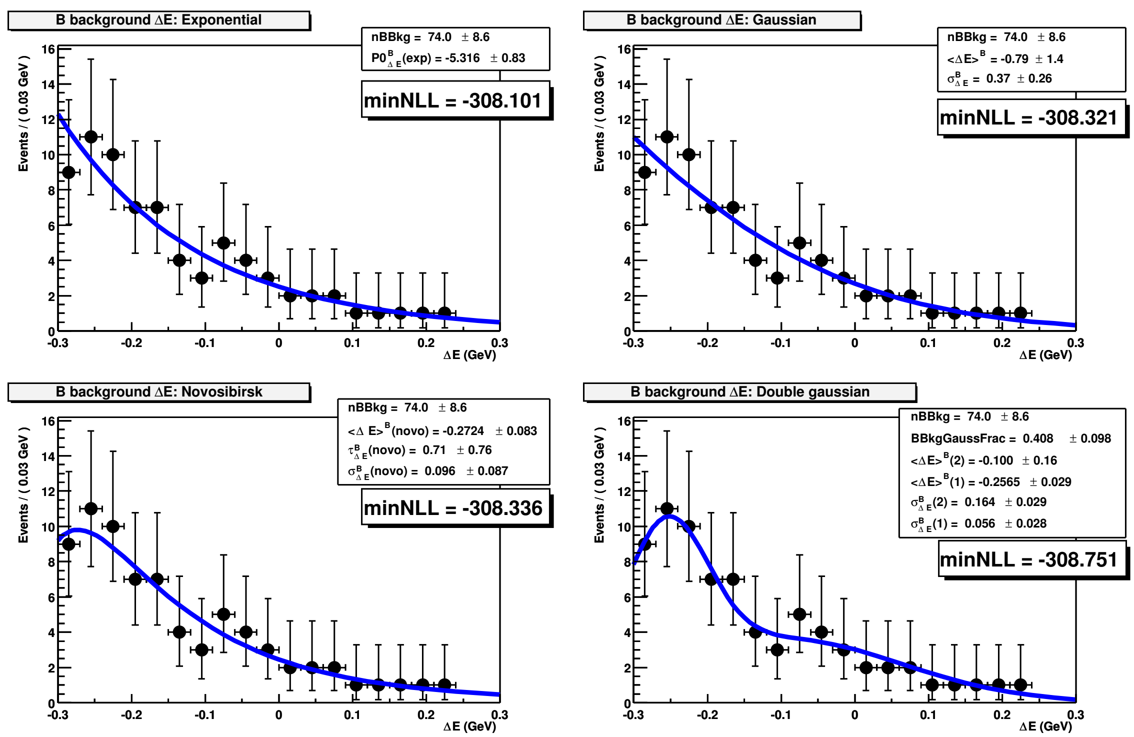

(b) Different B background shapes.

Figure 9.2. Lower assumed B background shapes. The reduction of the number of B background events is achieved by shifting the B background in ΔE according to the shift between Monte Carlo and real data and also by multiplying the $B \to X_{s/d}\gamma$ Monte Carlo by a factor of 0.4.

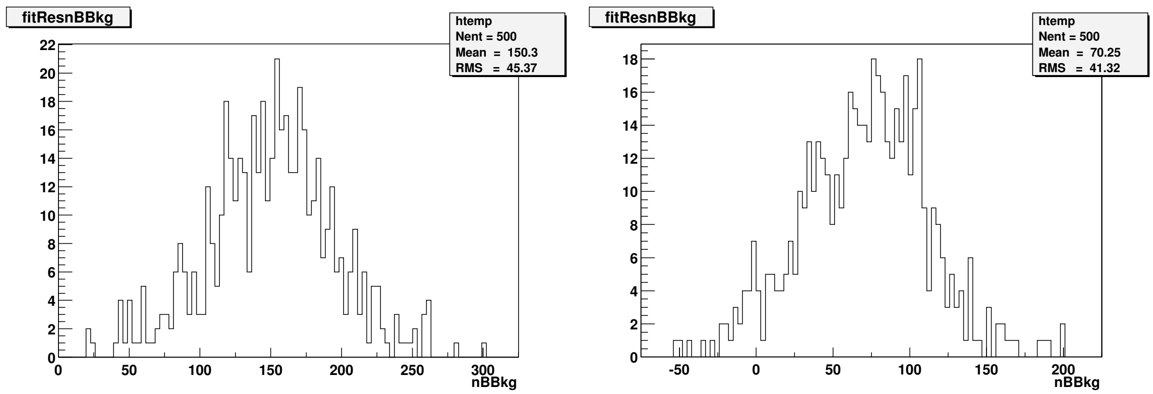

(a) 150 generated B background events. (b) 74 generated B background events.

Figure 9.3. Fitted B background yield. Two toy Monte Carlo studies have been performed with different number of B background generated. The plot on the left shows the fit result for the B background yield parameter (nBBkg) to a set of 500 toy Monte Carlo experiments generated with 150 B background events. The plot on the left shows the fit result for the B background yield parameter (nBBkg) to a set of 500 toy Monte Carlo experiments generated with 74 B background events.

to subtract the same number of events from the signal region than there are expected background events in that region. A relativistic Breit–Wigner distribution has been fitted to the background subtracted $K^{\pm}\pi^0$ invariant mass distribution (see Figure 9.4). The fitted width of the Breit–Wigner is $896.6 \pm 2.4\,\mathrm{MeV}/c^2$ about two sigmas higher than the tabulated position of the $K^{*\pm}$ peak [10]. The fitted Breit–Wigner width is $49.5 \pm 5.4\,\mathrm{MeV}/c^2$, perfectly consistent with the tabulated $K^{*\pm}$ width [10]. Since there is no indication for a flat component, the observed signal is consistent with originating from $B \to K^*\gamma$ decays exclusively.

9.4 Resulting Branching Fraction

The branching fraction is computed from the fit result of the signal yield. The corrected efficiency $\epsilon_{SIG} = 0.177$ is used as well as the systematic error in it. Also, a isospin factor for the decay $K^{*\pm} \to K^{\pm}\pi^0$ of 0.333 has been assumed; this is the branching fraction of this $K^{*\pm}$ decay mode $\mathcal{B}(K^{*\pm} \to K^{\pm}\pi^0)$. Furthermore, the number of $B\bar{B}$ events $N_{B\bar{B}} = 88.2 \times 10^6$ is needed. The branching fraction $\mathcal{B}$ for the

$B^{\pm} \to K^{*\pm}\gamma$ decay is then computed as

$$\mathcal{B}(B^{\pm} \to K^{*\pm}\gamma) = \frac{N_{SIG}}{\epsilon_{SIG} \cdot N_{B\bar{B}} \cdot \mathcal{B}(K^{*\pm} \to K^{\pm}\pi^{0})} = (4.83^{+0.45+0.48}_{-0.42-0.40}) \times 10^{-5} \ , \quad (9.1)$$

where the first error is statistical and the second is systematic. All the information needed for calculating the branching fraction is summarized in Table 9.2.

Signal Yield	Efficiency	$N_{B\bar{B}}(\times 10^{6})$	Isospin	$\mathcal{B}(B^{\pm} \to K^{*\pm}\gamma)(\times 10^{-5})$
$250.9^{+23.2}_{-21.8}$	0.177 ± 0.016	88.2	0.333	$4.83^{+0.45+0.48}_{-0.42-0.40}$

Table 9.2. Unblinded signal yield and branching fraction for Run1 + Run2 data.

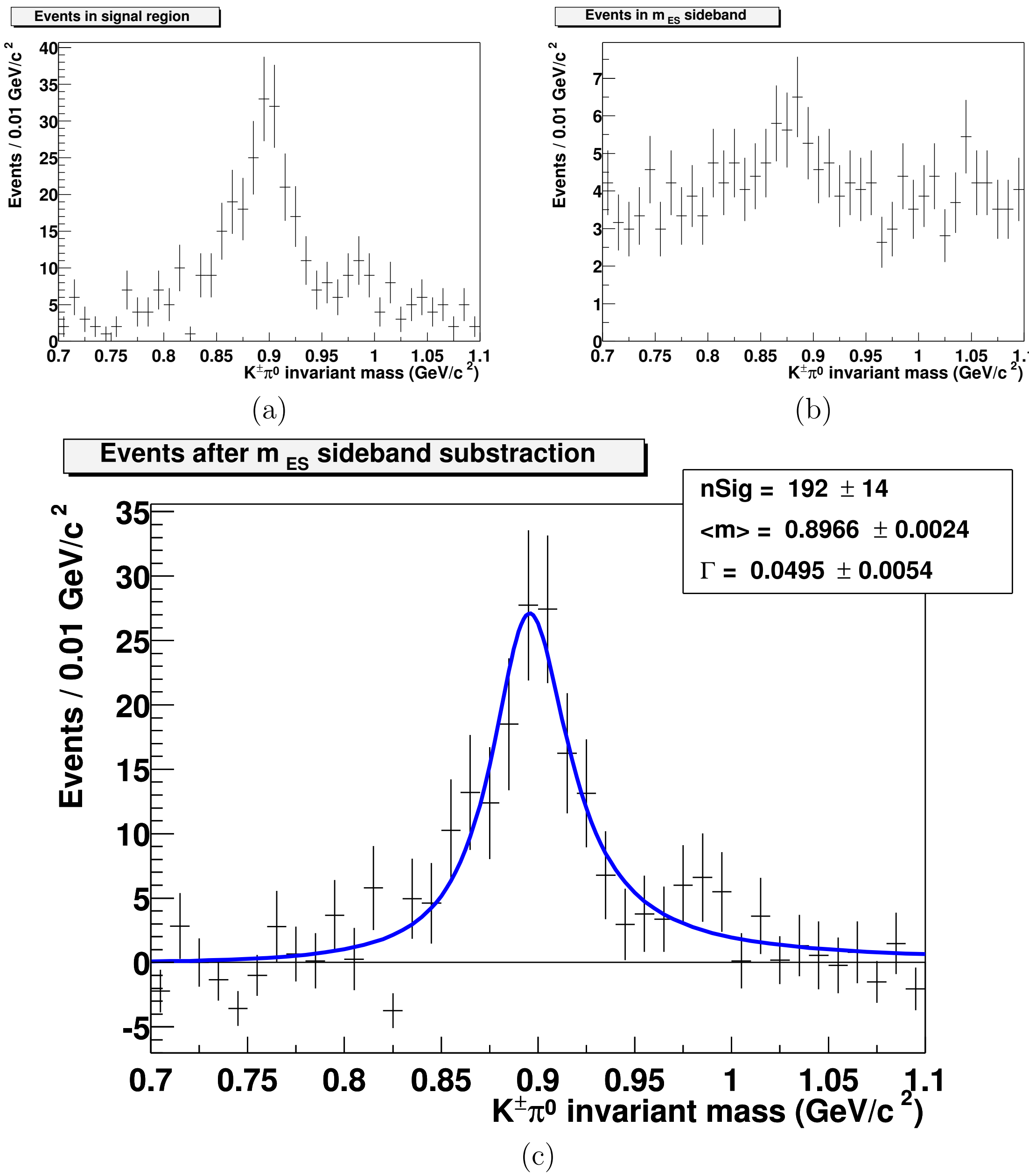

Figure 9.4. $K^{\pm}\pi^0$ invariant mass distribution for onpeak data. Distribution for (a) all selected onpeak data events, (b) events from the m_{ES} sideband scaled to the number of expected background events in the signal region. A relativistic Breit–Wigner distribution has been fitted to (c) background subtracted $K^{\pm}\pi^0$ invariant mass distribution.

CHAPTER 10

CONCLUSION

We have studied the rare radiative penguin decay $B^{\pm} \to K^{*\pm}\gamma$ with $K^{*\pm} \to K^{\pm}\pi^{0}$ using a sample of $(88.2 \pm 1.0) \times 10^{6}$ $B\bar{B}$ events collected with the BaBar detector at the the PEP-II asymmetric energy $e^{+}e^{-}$ collider, operating at a center of momentum energy of 10.58 GeV, the $\Upsilon(4S)$ resonance. The signal of $250.9^{+23.2}_{-21.8}$ events is extracted and the corresponding branching fraction is found to be $(4.83^{+0.45+0.48}_{-0.42-0.40}) \times 10^{-5}$, where the first error is statistical and the second is systematic.

The preliminary result presented here is about one standard deviation lower than the SM–based next to leading order calculations (see Table 1.1). In order to be able to make conclusions about differences between the SM and this measurement, the theoretical precision will need to improve considerably, e.g. by going to the next to next leading order calculation.

The measured branching fraction for the decay $B^{\pm} \to K^{*\pm}\gamma$ presented in this document is higher than the on 85.0×10^{6} $B\bar{B}$ pairs based corresponding *Belle* measurement of $(4.40 \pm 0.33 \pm 0.24) \times 10^{-5}$ (see Table 1.2). The difference is not significant since both results differ by less than one standard deviation.

The statistical error of this *Belle* measurement stated in Table 1.2 is smaller due to the inclusion of the decay mode $K^{*\pm} \to K^{0}_{S}\pi^{\pm}$. This measurement is also performed by the BaBar collaboration and its result will be included into the overall measurement of the branching fraction for the decay $B^{\pm} \to K^{*\pm}\gamma$. Since the statistical precision for this mode in the BaBar analysis is about the same as for the one discussed in this document, the total statistical error on the combined branching fraction will drop by approximately a factor of $1/\sqrt{2}$. This will lead to a slightly better statistical error for the BaBar measurement in comparison with the result from the *Belle* collaboration.

The systematic error for this analysis is dominated by the error on the neutral candidates (high–energy photon and especially π^0). An improvement of this systematic uncertainty is expected to be made soon. Once this improvement is done, the total systematic error for the BaBar result for the combined decay $B^{\pm} \to K^{*\pm}\gamma$ should be of the same order as the systematic error from the *Belle* collaboration.

	$B^{\pm} \to K^{*\pm}\gamma$, $K^{*\pm} \to K^{\pm}\pi^0$ decay mode only	
	Signal Yield	$\mathcal{B}(B^{\pm} \to K^{*\pm}\gamma)$
BaBar	$250.9^{+23.2}_{-21.8}$	$(4.83^{+0.45+0.48}_{-0.42-0.40}) \times 10^{-5}$
Belle	$86.4 \pm 11.1 \pm 2.4$	$(4.52 \pm 0.58 \pm 0.27) \times 10^{-5}$

Table 10.1. Comparison between the BaBar and *Belle* measurement. The decay modes $B^{\pm} \to K^{*\pm}\gamma$, $K^{*\pm} \to K^{\pm}\pi^0$ are shown. Signal yield is given in the middle column and the calculated branching fraction is given in the right column. The first error is statistical and the second is systematic.

Thanks to the superb charged particle ID system of the BaBar detector, the decay mode discussed in this document is statistical much cleaner than the same decay mode measured with the *Belle* detector. The signal yield for this analysis is 250.9 ± 22.6 which corresponds to a 9.0% statistical error. The corresponding signal yield measured with the *Belle* detector is $86.4 \pm 11.1 \pm 2.4$ which corresponds to a 12.8% statistical error for the decay $B^{\pm} \to K^{*\pm}\gamma$, $K^{*\pm} \to K^{\pm}\pi^0$. With this signal yield, the *Belle* collaboration also calculated the branching fraction for the decay $B^{\pm} \to K^{*\pm}\gamma$, $K^{*\pm} \to K^{\pm}\pi^0$ and their result is $(4.52 \pm 0.58 \pm 0.27) \times 10^{-5}$ [13]. This result is in excellent agreement with the one presented in this document (see Table 10.1).

Overall, this analysis can compete very well with the *Belle* measurement. Both measurements are based on a similar amount of data. In fact the statistical precision of the measurement discussed in this document is considerably better than the corresponding statistical error achieved by the *Belle* collaboration.

The measurement of the branching fraction for the decay $B^{\pm} \rightarrow K^{*\pm}\gamma$, $K^{*\pm} \rightarrow K^{\pm}\pi^{0}$ presented in this document is statistically the most precise measurement performed so far!

APPENDIX

USED FUNCTIONS

The Gaussian Function

A simple symmetric Gaussian function is defined as

$$\mathcal{F}_{Gauss}(x) = C_{Gauss} \cdot e^{-\frac{(x-\langle x\rangle)^2}{2\sigma^2}} \quad , \tag{A.1}$$

where $\langle x\rangle$ is the mean of the distribution, σ is its width and C_{Gauss} is the normalization constant.

The Novosibirsk Function

The Novosibirsk function is a function describing an asymmetric peak

$$\mathcal{F}_{Novo}(x) = C_{Novo} \cdot e^{-\frac{1}{2}\left(\frac{\ln^2\left(1+\tau\cdot(x-\langle x\rangle)\cdot\frac{\sinh\left(\tau\sqrt{\ln 4}\right)}{\sigma\tau\sqrt{\ln 4}}\right)}{\tau}+\tau^2\right)} \quad . \tag{A.2}$$

As usual, $\langle x\rangle$ refers to the mean of the distribution and σ refers to the width. The asymmetry (w.r.t. a gaussian function) is described by the additional parameter τ, referred to as the "tail" parameter.

The Crystal Ball Function

The Crystal Ball function is a simple Gaussian at the peak center. It deviates from a Gaussian in that it has a tail attached at one side of the peak, depending on the parameter α. The tail is attached in such a way as to have continuous function and first derivative. The function is

$$\mathcal{F}_{CB}(x) = C_{CB} \cdot \begin{cases} e^{-\frac{(x-\langle x\rangle)^2}{2\sigma^2}} & \text{for} \quad x > \langle x\rangle - \alpha\sigma \\ \frac{\left(\frac{n}{\alpha}\right)^n \cdot e^{-\frac{\alpha^2}{2}}}{\left(\frac{\langle x\rangle - x}{\sigma} + \frac{n}{\alpha} - \alpha\right)^n} & \text{for} \quad x \leq \langle x\rangle - \alpha\sigma \end{cases} , \tag{A.3}$$

where $\langle x\rangle$ is the mean of the function and σ is the width. These two parameters are the same as in a usual Gaussian function. We refer to the two new parameters α and n as the "attachment point" and the "power of the tail", respectively.

The Argus Function

The Argus function was first used to describe the continuum background in m_{ES} by the ARGUS collaboration [28]

$$\mathcal{F}_{Argus}(x) = C_{Argus} \cdot \frac{x}{E_{BEAM}} \cdot \sqrt{1 - \frac{x^2}{E_{BEAM}^2}} \cdot e^{-\xi\left(1 - \frac{x^2}{E_{BEAM}^2}\right)} , \tag{A.4}$$

where ξ is the "Argus parameter" and E_{BEAM} is the "Argus endpoint". In our case, E_{BEAM} is simply half of the center-of-momentum energy ($= \frac{\sqrt{s}}{2}$).

The Relativistic Breit–Wigner Function

An orbital angular momentum dependent relativistic Breit–Wigner function is used to describe the $K^{*\pm}$ mass peak in data and Monte Carlo:

$$f_{BW}(m) = C_{BW} \cdot \frac{m \cdot \Gamma_{rel}}{\left(m^2 - m_0^2\right)^2 + \left(m_0 \cdot \Gamma_{rel}\right)^2} , \tag{A.5}$$

with

$$\Gamma_{rel} = \Gamma \left(\frac{p}{p_0}\right)^{2l+1} \left(\frac{m_0}{m}\right) \cdot B^l(p, p_0) , \tag{A.6}$$

where:

- m is the reconstructed mass,
- $m_0 = 891.66\,\mathrm{MeV}/c^2$ is the position of the $K^{*\pm}$ resonance peak [10],
- $\Gamma = 50.8\,\mathrm{MeV}/c^2$ is the resonance width [10],
- p is the 3–momentum of the outgoing particle (either one due to momentum conservation) measured in the rest frame of the $K^{*\pm}$ meson and depending on its reconstructed mass,
- p_0 is the 3–momentum of the outgoing particle (either one due to momentum conservation) measured in the rest frame of the $K^{*\pm}$ meson evaluated at $\langle m \rangle$,
- l is the orbital angular momentum of the daughter particles ($l = 1$ in this case since the $K^{*\pm}$ is a vector meson (spin 1) and both daughter particles are scalar mesons (spin 0)),
- $B^l(p, p_0)$ is the ratio of two Blatt–Weisskopf barrier functions (see Equation A.10).

The Blatt–Weisskopf barrier functions are due to the limited range of the strong force ($\approx 1fm$). Thus, the maximum angular momentum in a strong decay is limited by the momenta of the decay products:

$$\vec{L} = \vec{r} \times \vec{p}\ , \tag{A.7}$$

$$\left|\vec{L}\right| = (1fm) \cdot |\vec{p}|\ \ . \tag{A.8}$$

If the decay particles have low momentum and the impact parameter, due to the strong force, is of the order of $1fm$, the decay products cannot generate sufficient angular momentum to conserve the spin of the decaying particle. Blatt and Weisskopf calculated functions in order to account for this effect [29]. The Blatt-Weisskopf function for angular momentum $l = 1$ is:

$$F_1(p) = \sqrt{\frac{(pr)^2}{(pr)^2 + 1}} \; , \tag{A.9}$$

where $r = 5\,\mathrm{GeV}^{-1}c$ is the range of the interaction. The above mentioned ratio is then:

$$B^l(p, p_0) = \frac{F_1(p)}{F_1(p_0)} \; . \tag{A.10}$$

BIBLIOGRAPHY

[1] L. Wolfenstein, Phys. Rev. Lett. **13**, 562 (1964).

[2] L. Wolfenstein, Phys. Rev. Lett. **51**, 1945 (1983).

[3] *BaBar*, B. Aubert *et al.*, Phys. Rev. Lett. **87**, 091801 (2001), hep-ex/0107013.

[4] *Belle*, K. Abe *et al.*, Phys. Rev. Lett. **87**, 091802 (2001), hep-ex/0107061.

[5] J. R. Ellis, M. K. Gaillard, D. V. Nanopoulos, and S. Rudaz, Nucl. Phys. **B131**, 285 (1977).

[6] A. Ali and A. Y. Parkhomenko, Eur. Phys. J. **C23**, 89 (2002), hep-ph/0105302.

[7] M. Beneke, T. Feldmann, and D. Seidel, Nucl. Phys. **B612**, 25 (2001), hep-ph/0106067.

[8] S. W. Bosch and G. Buchalla, Nucl. Phys. **B621**, 459 (2002), hep-ph/0106081.

[9] M. Battaglia *et al.*, (2003), hep-ph/0304132.

[10] K. Hagiwara *et al.*, Physical Review D **66**, 010001+ (2002).

[11] CLEO, T. E. Coan *et al.*, Phys. Rev. Lett. **84**, 5283 (2000), hep-ex/9912057.

[12] *BaBar*, B. Aubert *et al.*, Phys. Rev. Lett. **88**, 101805 (2002), hep-ex/0110065.

[13] *Belle*, K. Abe *et al.*, Measurement of the $B \rightarrow K^{*}\gamma$ branching fractions, in *Flavor Physics and CP Violation*, Paris, 2003, BELLE-CONF-0239.

[14] *BaBar*, B. Aubert *et al.*, (2002), hep-ex/0207076.

[15] *BaBar*, e. Harrison, P. F. and e. Quinn, Helen R., Papers from Workshop on Physics at an Asymmetric B Factory (BaBar Collaboration Meeting), Rome, Italy, 11-14 Nov 1996, Princeton, NJ, 17-20 Mar 1997, Orsay, France, 16-19 Jun 1997 and Pasadena, CA, 22-24 Sep 1997.

[16] *BaBar*, B. Aubert *et al.*, Nucl. Instrum. Meth. **A479**, 1 (2002), hep-ex/0105044.

[17] R. Santonico and R. Cardarelli, Nucl. Instrum. Meth. **187**, 377 (1981).

[18] *BaBar*, B. Aubert *et al.*, (2003), hep-ex/0306038.

[19] G. C. Fox and S. Wolfram, Phys. Rev. Lett. **41**, 1581 (1978).

[20] T. Brandt, *Electron Identifcation and Measurement of the Inclusive Semileptonic Branching Fraction of B Mesons at the BaBar Experiment*, PhD thesis, Technische Universität Dresden, 2001.

[21] *BaBar*, B. Aubert *et al.*, 2002 comparison of kaon ID selectors for data & MC, World Wide Web, `http://www.slac.stanford.edu/~sokoloff/Babar/PID/pidplots030120/`.

[22] G. Mancinelli and S. M. Spanier, Kaon selection at the *BaBar* experiment (PidKaonSMMSSelector, PidKaonMicroSelector), *BaBar* Analysis Document (BAD) 116, version 1.

[23] A. Hoecker *et al.*, The DIRC timing, *BaBar* Analysis Document (BAD) 73, version 1.

[24] B. H. Denby, Invited tutorial to be publ. in Proc. of 2nd Int. Workshop on Software Engineering, Artificial Intelligence and Expert Systems for High Energy and Nuclear Physics, La Londe-les- Maures, France, Jan 13-18, 1992.

[25] University of Stuttgart and University of Tübingen, Stuttgart neural network simulator, World Wide Web, `http://www-ra.informatik.uni-tuebingen.de/SNNS/`.

[26] *BaBar*, B. Aubert *et al.*, Neutral reconstruction analysis working group, World Wide Web, `http://www.slac.stanford.edu/BFROOT/www/Physics/Analysis/AWG/Neutrals/`.

[27] *BaBar*, B. Aubert *et al.*, (2002), hep-ex/0207074.

[28] ARGUS, H. Albrecht *et al.*, Z. Phys. **C48**, 543 (1990).

[29] F. Von Hippel and C. Quigg, Phys. Rev. **D5**, 624 (1972).